TÉCNICO LISBOA

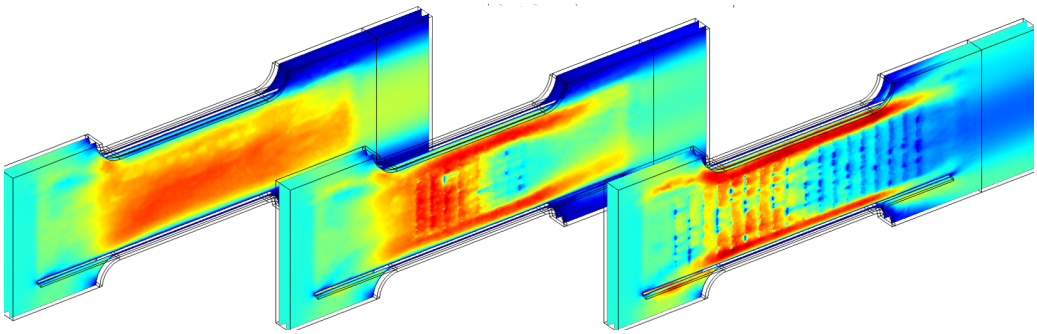

Development of a Custom Made Condenser for a Two-Phase Thermosyphon CPU Cooling System

João Miguel Martins Lameiras

Thesis to obtain the Master of Science Degree in

Mechanical Engineering

Supervisors: Prof. António Luís Nobre Moreira
Dr. Ana Sofia Oliveira Henriques Moita

Examination Committee

Chairperson: Prof. Edgar Caetano Fernandes
Supervisor: Dr. Ana Sofia Oliveira Henriques Moita
Member of the Committee: Prof. José Maria Campos de Silva André

November 2018

Acknowledgments

First I would like to thank my supervisor Doctor Ana Moita for the scientific guidance and supervision through the course of this dissertation. I'd also like to thank my professor and supervisor Professor Doctor António Luis Nobre Moreira for having me in his laboratory team.

My thanks to Construtora de Radiadores for the manufacture of the custom made condenser used in this work, specially to Mr. José Eduardo who was always attentive and helpful. A huge thanks to Eng. Pedro Pontes for answering to all my questions giving me all the support and motivation along the elaboration of this master dissertation. A big acknowledgment goes also to Doctor Artem Nikulin who helped me a lot, advising me at different topics related with my thesis. Also i can't forget, all my laboratory mates, especially to Filipe Andrade and Ricardo Cautela, who helped me in countless occasions and kept me motivated. Also, for all the support through the machining of several parts for the experimental facility, I need to thank Mechanical II building workshop's staff. Acknowledgements are also due to Fundação para a Ciência e Tecnologia (FCT) for partially financing the research under the framework of the project JICAM/0003/2017, in the context of Projecto 3599 - Promover a Produção Científica, o Desenvolvimento Tecnológico e a Inovação.

I'd like to give a special thank you to all my good friends that support me and make this challenge less difficult. And last but not least I'd like to give a sincere thanks to my family, specially parents and sister mostly for all the love and support, but also for all the support through this academic journey essential for my graduation and for my future professional life.

Abstract

The present work aims at the development and characterization a custom air-cooled condenser to be implemented on a thermosyphon cooling system based on pool boiling and condensation of a dielectric fluid - HFE-7000. This gravity-assisted cooler is designed to be applied on a commercially available desktop CPU, to be capable of dissipating heat loads up to 250W. A numerical simulation was performed to define the design of the condenser and also to perform a parametric sensible study. The air-side heat transfer performance was evaluated based on the Colburn factor (j) and the Fanning friction factor (f) was determined to analyze the pressure drops. An experimental study was also performed on a benchmark test facility, examining the condenser effectiveness and its effect on the overall cooling system thermal resistance.

A multi-louvered fin heat exchanger with core's size of 110x120x22mm, which was the outcome of the numerical study, was manufactured and tested in the experimental study. The condenser was characterized both in reflux and circulation, under steady-state and transient regimes. In this experimental characterization of the condenser, other parameters such as the tilt angle, effect of micro-structuring the surface on the evaporator and the effect of surface orientation were also addressed to evaluate their impact in the overall performance of the cooling system, incorporating the designed new condenser.

Based on this analysis, the final thermosyphon system devised here with condenser in circulation achieved better results, $R = 0.275\mathrm{K/W}$ with $q = 200\mathrm{W}$ for horizontal surface orientation.

Keywords

Louvered fins, Condensation, Thermosyphon cooling, Closed loop thermosyphon.

Resumo

Este trabalho tem como objetivo desenvolver e caracterizar um condensador personalizado arrefecido a ar para ser implementado num sistema de arrefecimento em termossifão baseado na ebulição e condensação de um fluido dielétrico - HFE-7000. Este *cooler* é projetado para ser aplicado num CPU de secretária capaz de dissipar até 250W. Foi realizada uma simulação numérica para definir as dimensões do condensador e também para efetuar um estudo paramétrico na geometria da alheta. O calor transferido para o ar foi analisado com base no factor de Colburn (j) e o factor de Fanning (f) foi utilizado para analizar as perdas de carga. Um estudo experimental foi realizado numa instalação de ensaio para analisar a aplicabilidade, avaliando a efectividade do condensador e o seu efeito na resistência térmica do sistema de arrefecimento.

Um permutador de calor com multi-alhetas em grelha e com miolo de dimensão 110x120x22mm, que foi o resultado da simulação numérica, foi fabricado e testado experimentalmente. O condensador foi caracterizado em refluxo e circulação, em regime estacionário e transiente. Nesta actividade experimental outros parametros como a inclinação do condensador, o efeito de microestrururação da superficie do evaporador e o efeito da orientação da superfície também foram estudados de modo a avaliar o seu impacto no desempenho do sistema de arrefecimento, incorporando o novo condensador projetado.

Baseado nesta análise, o sistema final em termossifão com o condensador em circulação apresenta melhores resultados, $R = 0.275\mathrm{K/W}$ para $q = 200\mathrm{W}$ com a superfície na horizontal.

Palavras Chave

Alhetas em grelha, Condensação, Arrefecimento de termossifão, Circuito fechado em termossifão.

Contents

List of Figures

List of Tables

Acronyms

CFD	Computational Fluid Dynamics
CHF	Critical Heat Flux
CLTPT	Closed Loop Two-Phase Thermosyphon
CPU	Central Processing Unit
CTPT	Closed Two-Phase Thermosyphon
CWC	Controlled Working Conditions
FEM	Finite Element Method
GWP	Global Warming Potential
HTC	Heat Transfer Coefficient
IC	Internal Circuit
IR	Infrared
MUMPS	Multifrontal Massively Parallel Sparse Direct Solver
ONB	Onset of Nucleate Boiling
PARDISO	Parallel Sparse Direct Linear Solver
PFHE	Plate Fin Heat Exchanger
RPM	Revolutions Per Minute
RWC	Real Working Conditions
TDP	Thermal Design Power

Nomenclature

Latin letters

A_c	Minimum flow cross section area	mm^2
A_o	Total air-side surface area	mm^2
A_f	Frontal area of the heat exchanger	mm^2
Bo	Bond number	-
C	Capacity rate	$\mathrm{J/s.K}$
C^*	Heat capacity rate	-
c_p	Specific heat	$\mathrm{J/kg.K}$
D	Diameter	mm
f	Fanning friction factor	-
F_d	Fin depth	mm
F_l	Fin length	mm
G	Fluid mass velocity	$\mathrm{kg/m^2.s}$
h	Heat transfer coefficient	$\mathrm{W/m^2.K}$
h_{fg}	Latent heat of vaporization	$\mathrm{J/kg}$
j	Colburn factor	-
J^*	Modified Froude number	-
k	Fluid thermal conductivity	$\mathrm{W/m.K}$
L_p	Louver pitch	mm
L_α	Louver angle	$\mathrm{degrees}$
$\dot{m}$	Fluid mass flow rate	$\mathrm{kg/s}$
Nu	Nusselt number	-
p	Pressure	mbar
Pr	Prandtl number	-
q	Heat rate	W
q''	Heat flux	$\mathrm{W/cm^2}$
R	Absolute thermal resistance	$\mathrm{K/W}$
Re	Reynolds number	-
S	Distance between cavities	$\mu\mathrm{m}$
T	Temperature	$^\circ\mathrm{C}$
T_m	Fluid bulk temperature	$^\circ\mathrm{C}$
T_∞	Ambient fluid temperature/ Free stream temperature	$^\circ\mathrm{C}$
u	Fluid velocity	$\mathrm{m/s}$
U	Overall heat transfer coefficient	$\mathrm{W/m^2.K}$
u_m	Fluid mean axial velocity	$\mathrm{m/s}$
x	Vapor quality	-
X_{tt}	Martinellii parameter	-

Greek symbols

θ	tilt angle	$\mathrm{degrees}$
ν	Fluid dynamic viscosity	$\mathrm{Pa.s}$
ρ	Fluid density	$\mathrm{kg/m^3}$
α	Aspect ratio/void fraction	-
μ	Fluid kinematic viscosity	$\mathrm{m^2/s}$
δ_f	Fin thickness	mm
η_f	Fin efficiency	-
η_0	Extended surface efficiency	-
ε	Effectiveness	-
σ	Surface tension	$\mathrm{N/m}$

Subscripts

a	air-side
c	cold/critical
cond	condenser
e	excess
evap	evaporator
f	fluid/fouling
h	hydraulic/hot
g	gas/vapor
i	inside/inlet
j	junction
l	liquid
o	outlet/overall
sat	saturation
sys	system
w	wall

1. Introduction

1.1 Context and Motivation

Gordon Moore foresaw that the number of transistors in an Internal Circuit (IC) would approximately double every two years - Moores' Law [1]. Half-century later, Moore's prediction held true with exceptional accuracy, in such way that became one of the driving principles of semiconductors industry. Along the years, the increasing number of transistors per chip has been followed by a significant size reduction in the chips and encapsulations, looking for higher processor's performance. Dennard [2] observed that voltage and current should be proportional to the linear dimensions of a transistor. Thus, as the size of the transistors shrunk, the voltage was reduced, circuits could operate at higher frequencies at the same power - Dennard scaling [2]. This was truth until the breakdown around 2006, when thermal and material limitations had been found, due to the small size of the transistors (lower than 65nm), causing a considerable increasing of thermal power dissipation.

The continued scaling of IC technology together with the resultant ever-increasing power density and operating temperature poses significant challenges to engineers worldwide. The junction temperature has significant impacts on microelectronic performance and should be maintained within an acceptable range, typically lower than 80°C. This is vital since transistors speed is slower at higher temperatures, due to the degradation of carrier mobility. Furthermore, elevated operating temperatures greatly increase the leakage power as IC designs move into the deep submicron regime [3]. The interconnect metal resistivity is also dependent on temperature (e.g., the resistivity of copper increases by 39% from 20°C to 120°C). Higher resistivity causes longer interconnect delay and consequent performance degradation. Last, but not least, reliability of the die and the package is strongly related to temperature: the temperature exponentially decreases the mean time to failure, hence the life time is also decreased in the same proportion. So, high operating temperatures have significant negative impacts on the performance, power consumption and reliability of the microprocessors [4].

In summary, the junction temperature has become a major concern for high performance microprocessors as more devices are integrated on a chip. In order to solve the Thermal Power Management issue and keep with the improvement of microprocessors' performance, effective cooling technique should be developed to dissipate a large amount of heat from small areas. The present, widely used cooling techniques are not efficient enough. Therefore, adequate cooling is a key to maintaining the CPU working properly and, hence, achieving high performance reliability.

In this context, for higher dissipation heat fluxes, cooling with nucleate boiling is promising, as it removes dissipated heat within a wide range of fluxes and at relatively small surface temperature super-

heat. This technology benefits from the phase change latent heat of vaporization, being addressed as two-phase cooling technology. The thermosyphon is a simple and sustainable system that does not require pumping power. As shown in the literature review, that is presented in the next chapter, a relatively large number of studies have focused on the design of alternative electronics cooling techniques, many of them addressing pool boiling heat transfer. However, most of them has focused on the evaporator and on several strategies to enhance pool boiling heat transfer. However, little work has been performed yet on the condensation, despite its crucial role in the performance of the whole cooling system [5]. In this context, the main core of the present work is to improve the condenser design and performance, as this is the component of the cooling system with highest thermal resistance of unit area R''.

1.2 Objective and Contribution

In line with the context, the present work aims at developing and testing an air-cooled custom made condenser to be implemented in a closed two-phase thermosyphon. This cooler is devised to work on a commercially available desktop CPU and should be able to dissipate heats loads up to $250\mathrm{W}$.

The devised condenser must cope with the geometrical restrictions to fit in the limited size of a desktop. Manufacturing costs should also be considered.

To cope with this objective, the condenser was firstly designed and a numerical study was performed to establish the main dimensions and geometry of the condenser and evaluate the range of the most relevant parameters that should be used to assure the best cooling performance for a condenser as compact as possible.

The designed condenser was manufactured and evaluated based on an experimental work which addressed the performance of the condenser in terms of the dissipated heat and heat transfer coefficients, as well as of the flow characteristics (e.g. pressure drop). The overall cooling performance of the entire system was also evaluated, mostly based on the dissipated heat flux and on the resulting heat transfer coefficients, to address the effective impact of the devised condenser.

1.3 Organization

This document is organized in seven main chapters, including the present Introduction, which provides the context, motivation and objective of the work. Chapter 2 revises the relevant work, reported in the literature, on alternative CPU technologies and more specifically on the strategies used to enhance the performance of thermosyphon cooling systems applied to electronics cooling. Chapter 3 introduces the theoretical background required to understand the work performed in dimensioning, designing and testing the condensers for the thermosyphon cooling system. Chapter 4 describes the analysis per-

formed to design the condenser, optimizing the relevant influencing parameters. The designed condenser was manufactured and then experimentally tested in a thermosyphon cooling system. Hence, chapter 5 describes the experimental facility and procedures used to test the devised condenser, including the acquisition systems, instrumentation and respective uncertainties. The experimental results focusing on evaluating the performance of the devised condenser and of the overall thermosyphon cooling system are presented in discussed in chapter 6. Finally, main conclusions are addressed in chapter 7, which also proposes future work topics.

2. Sate of Art

2.1 CPU Cooling Technologies

Conventionally, air cooling-heat sink was employed widely for thermal management of electronic due to its simplicity, high reliability and low cost of the required equipment [6]. However, the current high heat densities demanded nowadays surpassed already the maximum heat loads which can be dissipated by forced convection air-cooled heat sinks. Under this scenario, the attention of industry and academia has shifted to alternative cooling technologies, namely liquid cooling and two-phase cooling. Note that the main advantage of the two-phase cooling technology is the ability to benefit from the latent heat of vaporization, thus absorbing large quantities of heat during the phase change.

Liquid based cooling of electronics is an obvious choice due to their superior thermophysical properties compared with air. Microchannel in single phase is an extremely efficient in removing heat from a compact space. However, this technique generally requires a high pumping power to sustain the pressure drops associated with driving the single-phase flow.

Several two-phase new technologies have been proposed, such as microchannel cooling [7, 8], jet impingement [9] and spray cooling [10]. These techniques are able to absorb large heat fluxes and consequently are pointed out as extremely promising and efficient, but complexity and cost of implementation could be prohibitive for an application such as CPU cooling. Mudawar [11] discussed the ability, advantages and disadvantages of different electronic cooling technologies. The disadvantage of the jet impingement technique is the large temperature gradients within the cooled devices due to the concentration of heat removal within the impingement zone. Furthermore during vigorous boiling there is a risk of separation of the liquid layer from the impingement zone.

The disadvantages of spray cooling are the complicated flow feature with spray nozzles, the possibility of clogging of the nozzles and the lot of power that is consumed in pressurizing the fluid. The need for careful periodic testing of nozzles and higher temperature difference compared to nucleate boiling are other disadvantages of spray cooling. Thus, this cooling scheme has strong implementation limitations in terms of size, weight, and power and requires pumping auxiliaries, not being suitable to embed in the near junction [12].

Under this scenario, pool boiling is not in fact considered as the mechanism delivering the highest heat transfer coefficients, but due to its feasibility and ease of implementation, it has been considered one of the most potential solutions in the field of electronics cooling [13].

Heat pipes, which work based on the phase change of a working fluid inside the pipes, are very

promising means of cooling electronic devices due to their extremely high effective thermal conductivity and very low effective thermal resistance. At present, this is one of the most viable means of cooling high heat fluxes. There are many commercial cooling applications of heat pipes and their ability to remove high heat loads has attracted tremendous interest from the electronic industries, namely in Central Processing Units (CPUs). Very recently, Chen et al. [14] reported a comprehensive review on design, fabrication and performance analysis of small heat pipes for electronics cooling. They also showed the potential of such small heat pipes in cooling small electronic devices and systems. The most fascinating feature of heat pipes is that they don't have any moving parts and thus they are highly reliable with minimum maintenance. Heat pipes also include no external energy or power consumption, are a noise free cooling technique, present increased longevity hence low operation and overall cost, very good application flexibility (due to simple and robust design and construction), small size and weight (suitable for modern electronic devices), work in any orientation, and sealed enclosure cooling thus no adverse effect to environment or the electronic devices.

Two-phase thermosyphon technology also rely on evaporation and condensation processes. The difference between the heat pipe and this cooling technique is that the liquid is returned from the condenser to the evaporator by gravity forces and not by a wick structure exerting a capillary action on the liquid phase. With no wick, a thermosyphon can be designed with less thermal resistances at reduced manufacturing cost and time, taking the form of Closed Two-Phase Thermosyphon (CTPT) or Closed Loop Two-Phase Thermosyphon (CLTPT). Two-phase thermosyphon solutions are an easy and safe choice, even when compared to heat pipes, due to its simplicity in terms of hardware and of the working principles, with reduced worries regarding pressure drops and pipes clogging, under the complex flow situations associated with convective heat transfer of two-phase flows.

In summary, the technologies already implemented in the market are mainly forced air convection (fin fan cooling), heat pipes and forced liquid convection (liquid cooling). All the others are still been studied and enhanced in research works. Spray cooling, micro-channels and jet are extremely promising and efficient in terms of heat removal, but complexity and cost of implementation could be prohibitive for an application such as CPU cooling. Despite of various challenges, the two-phase closed thermosyphon seem in this context to be the next candidate to effectively being employed as a CPU cooling solution.

2.2 Closed Two-Phase Termoshyphon Research

The two-phase closed thermosyphon cooling is a gravity-assisted system composed by an evaporator, a condenser and connecting pipes. In the evaporator the microprocessor heat is absorbed into the system due to the nucleate boiling mechanism, while at the condenser the heat is dissipated to the ambient due to the condensation of the working fluid. A fan promotes the air force heat transfer convec-

tion in the condenser. The high heat loads which can be dissipated at low superheat temperatures, may lead to high heat transfer rates of condensation and boiling. The vapour generated at the evaporator during pool rises due to buoyancy heading to the condenser. The condensate, in turn, returns into the evaporator due to a favorable gravitational head.

Though this technology has been widely studied in the past for several high power dissipation applications, only recently attention was given to the application of this technique to microelectronics cooling. Hence, in the context of CPU cooling, fewer studies were conducted [15, 16] although its applicability has been proven effective and reliable. Beyond that, the existent two-phase thermosyphons studies are only focused on the evaporator and boiling heat transfer as well as on the overall system efficiency, having no work done evaluating the condensation and the condenser impact.

The heat transfer mechanisms occurring in a thermosyphon are significantly affected by the geometry, the inclination angle, the vapour temperature, operating pressure, the filling ratio and the thermophysical properties of the working fluid [17]. Among those, the filling ratio which is defined as the volume ratio of the charged liquid to the whole thermosyphon has an important effect on the thermal performance of the device. In most of the cases, the input working fluid is overfilled so that the liquid pool remains during the thermosyphon operation. However, excessive liquid charge is not appropriate. On the opposite, when there is not sufficient amount of working fluid to assure a stable operation of the device for a given heat input - underfilled case may lead to burnout [18]. The most significant criterion to evaluate thermosyphon performance is the thermal resistance [19].

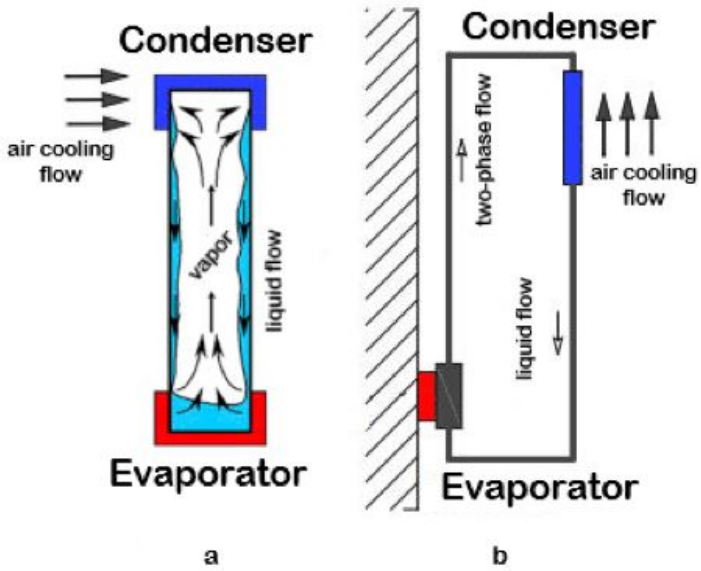

Figure 2.1: Schematic representation of (a) traditional thermosyphon (CTPT) and (b) loop thermosyphon (CLTPT).

As aforementioned, a two-phase thermosyphon may be designed as a single pipe CTPT or as a loop CLTPT, as shown in figure 2.1. In the first case, the liquid and vapour flow in opposite directions, also

known as reflux. Under high heat fluxes, the interaction between these counter-current liquid and vapour flow and the viscous shear forces occurring at the liquid/vapour interface may inhibit the return of liquid to the evaporator (entrainment effect [20]). This results in a decrease in the amount of liquid returning to the evaporator and its eventual, while the liquid droplets are held in the condenser which becomes flooded [21, 22]. If the evaporator section is not wet by returning fluid, the wall temperature significantly increases and the thermosyphon and/or the CPU may be permanently damaged. Furthermore, this two-phase flow in reflux mode introduces significant pressure fluctuations [23, 24] which vary the saturation temperature and trigger temperature fluctuations. These instabilities may cause problems in maintaining steady and safe operating conditions at phase-change heat transfer devices.

These operating limits are overcome in a closed CLTPT, where the liquid and vapour flows are separated and the flow is unidirectional. So, a conventional CLTPT is composed of an evaporator, a condenser and two connecting tubes - a rising (two-phase mixture from evaporator to the condenser) and a falling tube (condensed liquid back into de evaporator). The performance of a CLTPT with unidirectional coolant circulation by separating vapour and liquid flows, which is more geometrically flexible for transferring heat over a long distance, is generally improved from a CTPT. In a CLTPT, the phase change processes take place at different temperatures in the evaporator and condenser. The saturation pressure in the evaporator is generally higher than that in the condenser counterpart. This differential saturation pressure assists to drive the coolant circulation in a CLTPT. To ensure the required circulation rate to fulfill the cooling duty at the prescribed source-to-sink temperature difference for a CLTPT, the net driving pressure head is required to counteract the friction and form drags as well as the pressure drops attributed from flow acceleration/deceleration, bends, contractions and enlargements through the flow pathway. Note that the saturation temperature varies with pressure, which in turn affects the temperature potential for heat transfer. The heat transfer performance of the system is interdependent with its pressure drop.

Since the counter-current flow limitation seems to be a performance limitation at high heat fluxes, the use of thermosyphon loops with extended condenser surfaces has been suggested. In this study two arrangements are considered, namely the CLTPT with a single-pass condenser in circulation mode, where the flow direction is unidirectional and the CTPT with counter-current flow, using the condenser in reflux mode.

2.3 Thermosyphon Enhancement

In order to improve the system efficiency and reduce the size, it has become important to develop methods to enhance the heat transfer processes occurring at the thermosyphon. The following paragraphs swiftly review some passive methods reported in the literature to enhance the heat transfer

processes in the evaporator and in the condenser.

Strategies to Enhance Pool Boiling Heat Transfer - Evaporator

The strategies to enhance the pool boiling heat transfer can mainly be categorized in two major groups: (1) modifying the fluid properties and/or operating conditions (e.g. saturation pressure and subcooling) and (2) modifying the heating surface. The geometry and arrangement of the setup have also been scarcely studied, although most of the studies focus mainly on the effect of surface orientation (horizontal vs vertical and tilted surfaces), which naturally affects the positioning of the thermosyphon.

Modification of the fluid properties (e.g. using nanoparticles) is a complex an extensive approach, which is out of the scope of the current work. Concerning the modification of the working conditions, a few studies focused on water as working fluid and usually a sub-atmospheric boiling pressure is attained, to keep the heat surface temperature as low as possible. It's known that the boiling heat transfer processes are lessened as the governing pressure decreases, because at low pressure values both the bubble departure time and radius increase substantially [25], deteriorating the heat transfer coefficient.

Surface modification consists in altering the surface wettability by changing its topography and/or chemistry to enhance pool boiling heat transfer. Numerous studies have been performed in this context, using a wide diversity of patterns and techniques to alter the surface wettability. Extensive reviews on these studies can be found, for instance in Kim et al. [26] or more recently in Malavasi et al. [27]. In line with previous work, which evidenced good results in enhancing pool boiling heat transfer in a systematic way, using regular patterns of surfaces with microcavities (e.g. [28–30]), the present work addresses the use of surfaces microstructured with cavities. Decreasing the cavities distance, increases the fluid/surface contact area and also increases the number of cavities, which are more likely to act as nucleation sites, thus promoting the heterogeneous nucleation process. However, it would be extremely simplistic to consider that these two parameters linearly affect the heat transfer coefficients. In fact, Moita et al. [31] and Teodori et al. [32] observed that changing the spacing between cavities influences the interaction mechanisms, which in turn affects boiling heat transfer. Despite this is not the main goal within this work, several microstructured surfaces were tested, featuring inter-cavity distances ranging from 100 to 600 μm to check on the consistency of the previous findings reported by [28] and by [33].

Several authors investigated the effect of surface orientation in pool boiling heat transfer (Heat Transfer Coefficient (HTC) and Critical Heat Flux (CHF)) establishing correlations for different fluids and working conditions. The definition of increase orientation angle in the pool boiling means that the surface is being moved from facing upwards to facing downwards, where 0° is the horizontal upward and 90° vertical surface (tested orientations in this study). Nishikawa et al [34] studied experimentally water pool boiling on a copper plate and concluded that the HTC increases with the increase of orientation angle

in relatively low heat flux regions ($q'' < 7{\times}10^4\mathrm{W}$), while there is no marked effect in the high heat flux region ($q'' > 17{\times}10^4\mathrm{W}$). Nishikawa et al [34] attributed this trend to the decreased population density of nucleation sites on the heating surface and increased bubble diameters.

More recently, the effect of surface orientation on nucleate boiling was investigated with dielectric liquids, similar to the one used in this project. El-Genk and Bostanci [35], Priarone [36] and El-Genk and Parker [37] showed that the HTC increased markedly with the orientation angle (defined as in the previous paragraph), in accordance to the trends observed by Nishikawa et al. [34] in saturated water. When analysing the saturated pool boiling of HFE-7100 on a smooth copper surface, El-Genk and Bostanci [35] found that increasing the angle until $\theta \leq 90°$, HTC decreases for $\Delta T_e > 20\mathrm{K}$, while it increases for $\Delta T_e < 20\mathrm{K}$. Nucleate boiling heat flux decreased with increased θ, due to the increase in vapour accumulation near the surface, but increased with increased θ at low surface superheats ($\Delta T_e < 20\mathrm{K}$) due to the increase in mixing by rising bubbles in the boundary layer, whose residence time increases with increased inclination. The surface superheat at CHF also decreased with increasing θ. These results are consistent with those obtained by Rini et al [38] with dielectric and non-dielectric liquids.

Strategies to Enhance Condensation - Condenser

Heat transfer enhancement produced using a surface modification enhancement is one of the most effective passive enhancement techniques which can be utilized to improve the condensation processes occurring in a heat exchanger. Within this scope, extended surfaces or fins are employed in heat exchangers for effectively improving the overall heat transfer performance. In the case of in tube condensation there are two possibilities to enhance a heat exchanger: (1) enhancing the external surface and (2) enhancing the internal surface.

The external enhancement is especially imperative for air-cooled heat exchangers, since the dominant thermal resistance is usually on the air-side. In this context, Kays and London [39] reported the first reliable study on louvered fins and concluded that these arrays are very cost-effective. Louvers interrupt the airflow and create a series of thin boundary layers which have lower thermal resistance. Furthermore, the louvered structures promotes the air circulation between different fins promoting the heat transfer. The most important design parameters affecting the heat transfer and pressure drop in multi-louvered fins are the louver angle, the louver pitch, the fin pitch, the flow depth and the louver height. The most important drawback of louvered fins is associated to high pressure losses, when compared to the plain fin. However this pressure losses can be decreased by flattened tubes, with long axis parallel to the external fluid flow direction. In this work, a numerical simulation was performed taking into account the air-side external enhancement, so more information in this context is presented in chapter 4.

Due to the external air-side enhancements, significant additional advantages can be obtained by increasing the condensing-side, heat transfer coefficient. In some cases, the tubes are internally finned. Such procedure enhances heat transfer by providing a wider contact surface, while it also strengthens the tube to withstand internal pressure. Such arrangement also increases the vapour-side pressure drop for a given flow rate. This internal micro-fin enhancement is accomplished by disturbing the boundary layer, producing secondary flow, and increasing fluid turbulence [40].

Jung et al. [41] performed experiments condensing different refrigeration fluids (R22, R134a, R407C and R410A) inside plain and micro-fin tubes (0.2mm fin height) and found that the heat transfer coefficients of a micro-fin tube were 2-3 times higher than those of plain tubes.

Li et al. [42] carried out an experimental work to compare the condensation heat transfer characteristics of R22 and R410A in smooth and micro-fin tubes (0.15-0.17mm fin height). Their results indicated that the heat transfer coefficients of the micro-fin tube are approximately 1.65–2.55 times the HTC found in smooth tubes, while the pressure drop is more than 30$\%$ higher than that in smooth tubes.

Guo et al. [43] performed an experimental investigation to evaluate convective condensation and evaporation (R22, R32 and R410A) inside a smooth tube, a herringbone tube and the newly developed enhanced surface tube (dimple structure) at low mass fluxes. For condensation, unlike that observed in evaporation, the herringbone tube have the best performance with the heat transfer coefficient 2.0–3.0 times larger than the smooth tube.

Inclination Effect in Co-Current Flow

It is important to note that, along this work independently of the condenser's flow, the definition of increase orientation angle in condensation means that the condenser is being moved from an downward to upward flow, where 0° corresponds to the horizontal. So, a negative angle value corresponds to downward flow and a positive angle to upward flow.

Few studies are available for two-phase flows inside inclined tubes. A review of tilting effects on the flow patterns, heat transfer and pressure drop during condensation inside smooth tubes has been presented by Lips and Meyer [44–46]. Lips and Meyer [44–46] report an experimental study of convective condensation of R134a in an 8.38mm inner diameter smooth smooth tube at inclined orientations. These authors presented flow patterns and heat transfer coefficients during condensation for different mass fluxes and vapour qualities for the whole range of inclination angles (from vertical downwards to vertical upwards). Lips and Meyer [44–46] also report that for low mass fluxes and/or low vapour qualities, the flow pattern was strongly dependent on the inclination angle, whereas it remained annular for high mass fluxes and high vapour qualities regardless of the tube inclination. They also concluded that the condensation heat transfer enhancement also depends on saturation temperature, being the incli-

nation effect more pronounced at higher saturation temperature values. Their experimental results also showed that -30° is the optimum inclination angle that leads to the highest heat transfer coefficient for downward flow. More recently, these same conclusions were verified by Meyer and Ewim [47] and Abadi et al. [48].

In the work of Del Col et al. [49], the authors investigated the effect of inclination during condensation of R134a and R32 in a minichannel with 1.23mm inner hydraulic diameter and square cross section. Considering the heat transfer coefficient measured in horizontal channel as the reference case, they concluded that the channel inclination has negligible effect on condensation in downflow configurations at high mass velocity while in upflow configuration such effect is minor for the whole range of mass velocities. On the other hand, whatever the fluid, they found that the effect of the channel inclination on the condensation heat transfer coefficient becomes noteworthy in downflow, at low vapour qualities and mass velocities lower than a critical value, which was $G = 150\mathrm{kg/m^2.s}$ for R134a and $G = 200\mathrm{kg/m^2.s}$ for R32. In these working conditions, the inclination generally penalizes the condensation process and may cause a strong decrease of the heat transfer coefficient, up to 48$\%$ compared to that obtained in horizontal.

Inclination Effect in Counter-Current Flow

The effects of the inclination angle on reflux condensation heat transfer and flooding of R134a were investigated by Fiedler and Auracher [50]. These authors used a plain test tube with an inner diameter of 7mm and a length of 500mm as an idealized single sub-channel of a compact heat exchanger. They found that the inclination of the channel has a significant enhancing effect on heat transfer, an outcome related to the increase in the thin film regions around the perimeter. The optimum inclination angle for maximum heat transfer was found to be approximately 40° from the horizontal. At this inclination angle, the heat transfer was increased by a factor of almost 2 in comparison to reflux condensation in the vertical configuration.

Klahm et al. [51] investigated the heat transfer during reflux condensation of R134a inside a rectangular channel with a hydraulic diameter of 7 mm. Their experimental results were compared with the results previously reported by Fiedler and Auracher [50] for a circular test section with an inner diameter of 7mm. The rectangular channel used by Klahm et al. [51] reached a maximum heat transfer occurred at inclination angles between 30° and 60° to the horizontal. The heat transfer rate was almost 30$\%$ better than in the vertical case. They also found that heat transfer in a rectangular channel is about 50$\%$ better than in a circular tube with the same hydraulic diameter and inclination angle.

3. Theoretical Background

This chapter is aimed at providing theoretical insight into the concepts which were required for the design, development and discussion of the cooling system performance. This section is organized in two main topics. The first, addressed in revised in sub-chapter 3.1 revises the pool boiling heat transfer phenomena, occurring in the evaporator. The following sub-chapters address the theoretical background required to understand the heat transfer at the compact heat exchanger used as condenser. Thus, the theoretical background on condensation inside tubes, basic heat transfer and heat exchanger design are essential topics to be addressed here, as introduced in sub-chapters 3.2, 3.3 and 3.4 respectively.

3.1 Fundamentals of Pool Boiling Heat Transfer

Boiling occurs when the temperature of the surface, T_w exceeds the saturation temperature T_{sat} corresponding to the liquid pressure. The heat transferred from the solid surface to the liquid is expressed by the equation 3.1, well known as Newton's law of cooling.

$$q'' = h(T_w - T_{sat}) \tag{3.1}$$

The boiling process is characterized by the formation of vapour bubbles, which grow and subsequently detach from the surface. Vapour bubble growth and dynamics depend, in a complicated manner of different parameters, such as the excess temperature and thermophysical properties of the fluid. Besides that, the nature of the surface (i.e. surface topography and chemistry), the surface configuration and orientation (the main effects taken into account in this study) also affect the dynamics of vapour bubble formation and therefore strongly influence the HTC.

3.1.1 Boiling Curve

The boiling curves are a graphical representation of the variation of heat flux with respect to surface superheat, ΔT_e, defined by the difference between the surface temperature and the saturation temperature of the working fluid. Various boiling regimes can be identified within this curve, corresponding to different boiling characteristics, which in turn lead to a different heat flux evolution with ΔT_e. Nukiyama [52] was the first to identify different regimes of pool boiling, namely the single-phase natural convection, nucleate pool boiling, transition boiling and film boiling as illustrated in figure 3.1.

Single-phase natural convection heat transfer occurs when low heat flux is applied and is charac-

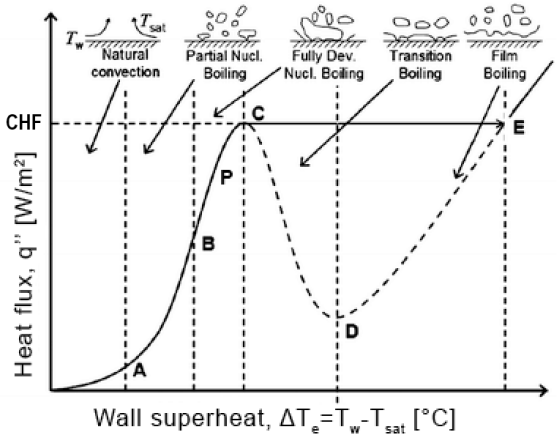

Figure 3.1: Typical boiling curve for water at 1 atm adapted from [53].

terized by low HTC variation. As the excess temperature is increased, bubble inception will eventually occur, but below the Onset of Nucleate Boiling (ONB), for $\Delta T_e < \Delta T_{e,A}$, the fluid motion is determined principally by free convection effects.

As wall superheat increases, the flow will then evolve to a fully developed nucleate boiling regime. In this range, two different flow regimes may be distinguished as displayed in boiling curve by A-B and B-C regions. In region A–B, isolated bubbles form at nucleation sites and separate from the surface. This separation induces considerable fluid mixing near the surface, substantially increasing HTC and heat flux, q''. In this regime most of the heat exchange occurs through direct transfer from the surface to liquid in motion on the surface and not through the vapour bubbles rising from the surface. As ΔT_e is increased, more nucleation sites become active and increased bubble formation causes bubble interference and coalescence. In the region B–C, the vapour escapes as jets or columns, which subsequently merge into slugs of the vapour. This trend inhibits the motion of liquid near the surface causing a decrease of the HTC. For this reason there is an inflection turn, point P represented in figure 3.1, which corresponds to the maximum HTC achieved. At this point HTC begins to decrease with increasing ΔT_e, although the product of h and ΔT_e continues to increase. At point C the maximum heat flux is achieved since considerable vapour is being formed, precluding the liquid to continuously wet the surface. This point is called CHF, being in the context of this cooling system a critical design point that establishes the limiting working conditions. In this work, the evaporator is projected to operate in the nucleate boiling regime.

Continuously increasing ΔT_e, the transition boiling occurs, being characterized by beginning of vapour blanket's formation above the surface. This effect causes a HTC major reduction due to lower vapour's thermal conductivity and consequently a wall superheat steep increase. At point D of the boiling curve, referred to as the Leidenfrost point, the heat flux is minimum and the surface is completely covered by a vapour blanket. Lastly, film boiling is initiated with the establishment of a vapour insulating layer over the surface, so that evaporation occurs at the liquid-vapour interface.

3.2 Condensation Inside Tubes

A condenser heat exchanger incorporates the thermosyphon cooling where vapour formed within the boiling process arises and undergoes a phase change returning to the liquid phase, closing the thermodynamic loop. This section broaches the theoretical background required to predict the convective condensation heat transfer coefficient, which in turn is needed to properly address the design of the condenser. In this work, flat tubes (rectangular shape with round corners), classified as minichannels, are used in the condensation with very low mass velocities (G <10$\mathrm{kg/m^2.s}$). The main topics covered in this sub-section are flow channel classification, flow patterns and heat transfer during convective condensation.

3.2.1 Flow Channel Classification

Hydraulic and heat transfer processes are affected differently depending on the relative importance of the governing forces, depending on the scale that is being considered. Hence, classification schemes that identify a channel as macro, mini, or micro should be considered merely as guidelines. Quite a few classifications of channels' dimension have been proposed. A widely used one and recommended for boiling and condensing flows it was defined by Kandlikar and Grande [54] according to the minimum channel dimension, as presented next:

Conventional Channels: $D > 3\mathrm{mm}$

Minichannels: $3\mathrm{mm} \geq D > 0.2\mathrm{mm}$

Microchannels: $0.2\mathrm{mm} \geq D > 0.01\mathrm{mm}$

According to Mehendail et al. [55], heat exchangers with hydraulic diameters greater than $6\mathrm{mm}$ are conventional or macro, $1\mathrm{mm} \leq D_h \leq 6\mathrm{mm}$ are compact, $0.1\mathrm{mm} \leq D_h \leq 1\mathrm{mm}$ are meso, and $6\mu\mathrm{m} \leq D_h \leq 1\mathrm{mm}$ are micro type. This classification has been widely accepted by the scientific community. For example, Kim and Mudawar [56] included tubes up to 6 mm diameter when validating their correlation for mini-channels. Cheng and Wu [57] adopted a different criteria, based on dimensionless Bond number, that includes the gravity and surface tension effects: Microchannel, if $Bo < 0.5$ (negligible effect of gravity), Minichannel, if $0.5 < Bo < 3.0$ (both gravity and surface tension have significant effect), Macrochannel, if $Bo > 3.0$ (surface tension has negligible effect).

In this study, the condensation occurs in a compact heat exchanger with several flat tubes of $D = 3\mathrm{mm}$, $D_h \approx 5\mathrm{mm}$ and $Bo \approx 2.45$. Accordingly to previous classifications schemes, it was possible to classify this case study as using parallel minichannels.

3.2.2 Flow Regimes in Condensation

Studies of heat transfer condensation inside minichannels have received in the recent years an increasing attention and an increased number of research laboratories have focusing on this research topic within the last years. However, very few studies were performed at similar operating conditions, mainly due to the difficulty in performing accurate measurements under such low flow speed conditions.

Round Tubes

Fundamentally, the two factors controlling the two-phase flow in round tubes are gravity and vapour shear. At low velocities gravity dominates and the condensate forms primarily on the top portion of the tube and flows downward into a liquid pool which is driven out axially partially by the vapour flow and partly by a gravitational head. In terms of void fraction, the flow regimes can be divided into high void and low void fractions. The first category includes five flow regimes: stratified flow, wavy flow, wavy-annular flow, annular flow and annular-mist flow. The second category includes slug, plug and bubbly flow. The five flow regimes in the first category are arranged such that each successive flow regime corresponds to an increasing in the vapour velocity. The three flow regimes in the second category are arranged

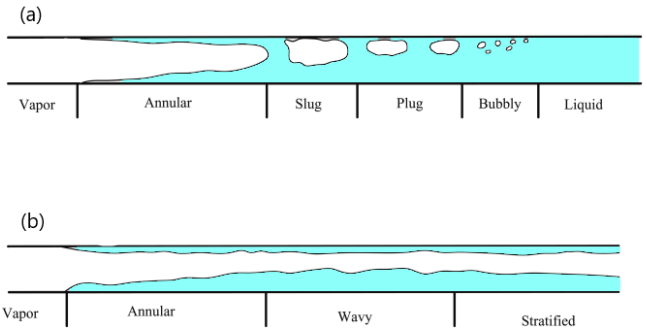

Figure 3.2: Two-phase flow patterns in horizontal tubes: (a) condensation with high liquid loading, (b) condensation with low liquid loading.

such that the transition from one flow regime to the next corresponds to a decrease in void fraction. At very low vapour velocities, the gravity controlled stratified flow regime is observed and the liquid-vapour interface remains smooth [58]. An illustration of these two-phase flow patterns in horizontal tubes is shown in figure 3.2.

Analogous to predicting the transition from laminar to turbulent flow in single-phase flow, numerous flow pattern maps have been developed for predicting two-phase flow regime transitions. Thome and El Hajal [59], El Hajal et al. [60] and Suliman et al. [61] developed flow pattern maps for condensation in horizontal tubes, following the original pattern map built by Kattan et al. [62] for flow boiling evaporation inside horizontal tube.

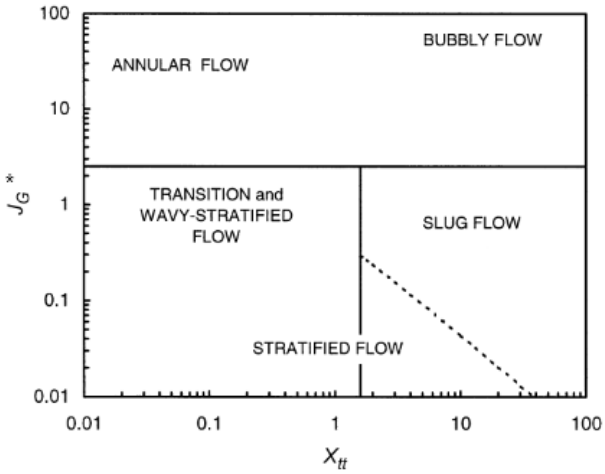

Figure 3.3: Cavallini two-phase flow regime maps adapted from [63].

Cavallini et al. [63] proposed a model for halogenated refrigerants inside smooth tubes, dependent of Martinelli parameter X_{tt} and dimensionless gas velocity, the so-called modified Froude number J_g^*. These parameters are defined in equation 3.2.

$$J_g^* = \frac{Gx}{\sqrt{\rho_g(\rho_f - \rho_g)gD_h}} \quad \text{and} \quad X_{tt} = (\frac{1-x}{x})^{0.9}(\frac{\rho_g}{\rho_l})^{0.5}(\frac{\mu_l}{\mu_g})^{0.1} \tag{3.2}$$

Figure 3.3 illustrates the various regimes and their transitions, like to $X_{tt} < 1.6$ the two-phase flows is annular for $J_g^* > 2.5$ and turns wavy stratified for $J_g^* < 2.5$.

Coleman and Garimella [64] investigated the effect of tube diameter and shape on flow patterns and flow regime transitions for air-water mixture flow in tubes with small hydraulic diameters from 1.3 to 5.5mm. They showed that while pipe diameter and surface tension may have a negligible effect on flow regime transitions in tubes with diameters larger than 10mm, for smaller tubes these factors play an important role. Therefore, flow regime maps such as those mentioned previously based upon data from larger tubes may not be applicable for a smaller tube diameter range. They showed that as the tube diameter decreases, the transition to a dispersed flow regime occurs at a higher value of the superficial liquid velocity. Also, the transition to annular flow occurs at a nearly constant value of the superficial gas velocity, which approaches a limiting value as the tube diameter decreases. Another effect of surface tension and tube diameter is to suppress the stratified regime in small diameter tubes and to increase the size of the intermittent regime. Thus, this study showed that the flow patterns and the respective transitions change significantly with tube diameter, as shown in figure 3.4.

In the present study, applying equations 3.2, the Martinelli parameter is $X_{tt} = 0.085$ and the maximum predicted gas velocity is $J_g^* = 0.1$, so the regime appears to be between stratified flow - wavy stratified flow. The same regime is obtained by applying the Coleman and Garimella [64] flow map,

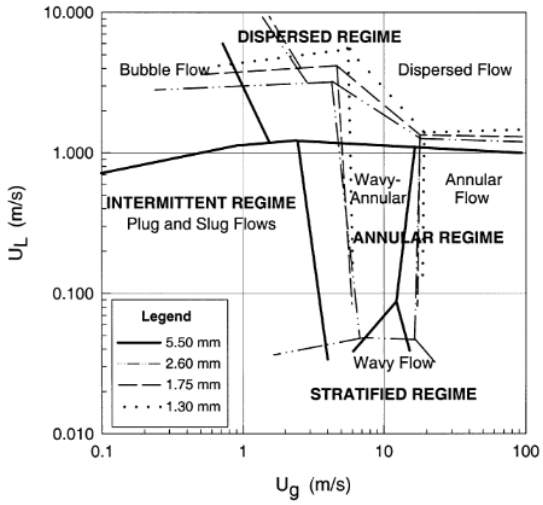

Figure 3.4: Coleman and Garimella flow regime map for round tubes adapted from [64].

since the vapour and liquid velocity are very low.

Non Circular Tubes

Little research has performed on regime maps for small hydraulic diameter rectangular tubes. For these tube geometries additional complexity arises due to the effect of aspect ratio on the specific flow regimes and transitions between them. In rectangular tubes, the effects of surface tension are expected to be more important as the liquid is more readily pulled up into the corners of the tube and held against gravity, leading to a thinner liquid film at flat sides and, therefore, to a lower thermal resistance.

Coleman and Garimella [64] also investigated the effects of surface tension in small diameter tubes. A rectangular tube of hydraulic diameter 5.36mm with an aspect ratio of 0.725 was chosen and the results were compared with those previously reported [64] for the 5.50mm round tube. The main difference between the rectangular and round tube flow patterns is in the transition to the dispersed flow regime, which occurs at a higher value of u_l for the rectangular tubes. It can also be seen that in the rectangular tube, the transition to the annular regime (wavy-annular and annular flow) occurs at a nearly constant value of u_g. Both the round and rectangular geometries show stratified flows. However, the stratified flow regime occurs at a lower gas velocity in the rectangular tube as illustrated in figure 3.5.

As the hydraulic diameter decreases, the effects of surface tension increasingly counteract the effects of gravity, promoting and extending the size of the annular film flow pattern region instead of the more stratified wavy flow regime. Thus, as D_h decreases, the wavy flow regime is increasingly replaced by the annular flow regime, and is non-existent in the $D_h = 1\mathrm{mm}$ tube.

Bortolin et al. [65] studied the condensation of R134a in a single horizontal minichannel with circular and square cross section. In fact, at high mass flux, the interfacial shear stress effects are more important than those of surface tension and gravity, so the HTC in circular and square minichannels are shown

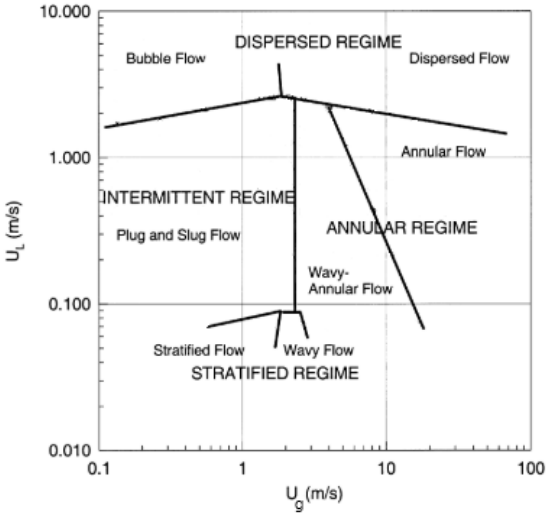

Figure 3.5: Coleman and Garimella flow regime map for rectangular tube (D_h =5.36mm and α =0.725) [64].

to be approximately the same. On the other hand, at low mass flux, the interfacial shear stress effect is less important and the liquid flow is expected to be laminar. In this case, the surface tension and the gravity forces play an important role to drive the liquid film and to control the heat transfer condensation inside the minichanel. The gravity is responsible for the liquid film thickness increase at the bottom of the circular minichannel, while in the square, the surface tension forces can be more important than gravity pulling the liquid toward the corners

Toninelli et al. [66] stressed the importance of the three forces affecting the liquid film distribution: shear, gravity and surface tension. Toninelli et al. [66] concluded that at low value of mass flux ($G \leq 200\mathrm{kg/m^2.s}$), surface tension can play an important role as microscale effects are observed. In particular, for vapour quality $x > 0.5$, both numerical simulations and experimental results show a clear enhancement of the heat transfer coefficient in the square channel with respect to the circular one. Such enhancement is due to the surface tension force that, in the square channel, pulls the liquid towards the corners leading to a low film thickness on the flat sides of the channel. Del Col et al. [67] studied the presence of smooth corners in a square cross section (minichannel). They concluded that for mass flux equal or lower than $200\mathrm{kg/m^2.s}$ it increases the HTC, but does not have a significant effect at higher mass flux.

3.2.3 Condensation Heat Transfer Coefficient

Chato [58, 68] developed a detailed analytical model of the heat transfer for gravity-driven condensation. [58, 68] neglected heat transfer in the liquid pool at the bottom of the tube and hypothesized that the bulk of the heat transfer was occurring in the film on the upper portion of the tube wall. Following

this, Chato [58, 68] proposed the modified Nusselt falling film condensation model:

$$\bar{h}_f = 0.728 K_c [\frac{\rho_l(\rho_l - \rho_g) g h'_{fg} k_l^3}{D\mu_l(T_{sat} - T_w)}]^{1/4} \tag{3.3}$$

$$h'_{fg} = h_{fg} + 0.69 c_{p,l}(T_{sat} - T_w) \tag{3.4}$$

Equation 3.3 is identical to the relation obtained from the classic Nusselt condensation model for the evaluation of the mean heat transfer coefficient for laminar condensation on the surface of a horizontal tube of diameter D, except that the multiplying prefactor has been changed. [58, 68] assumed for K_c in 3.3 the value of 0.76 (K_c constant depends of refrigerant), where ρ_l and ρ_g are the liquid and vapour densities, g the gravity acceleration, k_l the thermal conductivity of the fluid, μ_l is the fluid dynamic viscosity, T_{sat} and T_w are the saturation and wall temperatures. Following Chato's formulation, the modified latent heat h'_{fg} is calculated by equation 3.4, where h_{fg} is the latent heat of vaporization and $c_{p,l}$ the liquid heat capacity.

Dalkilic et al. [69] showed that, at low mass fluxes the equation presented by Carey [53] leads to the best results. This is very similar to that of Chato's with:

$$K_c = \alpha \tag{3.5}$$

$$\alpha = \frac{1}{1 + (\frac{1-x}{x})(\frac{\rho_g}{\rho_f})^{2/3}} \tag{3.6}$$

where α is the void fraction term for determining the depth of the liquid pool and x is the vapour quality. Carey [53] proposed using Zivi's [70] void fraction correlation 3.6. The above mentioned correlation evaluate the average heat transfer coefficient during gravity driven, neglecting heat transfer in the liquid pool.

The following correlations of Singh et al. [71] and Dobson and Chato [72] take into account the circumferential variation of the heat transfer coefficient. Singh et al. [71] proposed a correlation for stratified wavy flow pattern:

$$h_{cond} = \theta h_{bottom} + (2\pi - \theta) h_{top} \tag{3.7}$$

where θ was the angle in radian, subtended from top of the tube to the liquid level and was approximated by:

$$\theta = 2cos^{-1}(2\alpha - 1) \tag{3.8}$$

The heat transfer coefficient of the bottom film was evaluated as:

$$h_{bottom} = h_1(1 + \frac{0.2332}{X_{tt}^{1.402}}) \tag{3.9}$$

where h_1 was the heat transfer coefficient for the liquid portion of the flow evaluated with Gnielinski's [73] equation for $Re_l > 2300$ and evaluated with a modified Dittus-Boelter equation 3.10 for $Re_l < 2300$.

$$Nu_{convection} = 0.2339 Re_l^{0.5} Pr_l^{0.33} \tag{3.10}$$

The heat transfer coefficient in the top of the tube was evaluated with Chato's correlation with a K_c value of 0.0925.

Dobson and Chato [72] improved Chato's correlation, equation 3.3, by including a stratified-wavy model. The heat transfer coefficient was given in the form:

$$h_{cond} = h_{top} + (1 - \frac{\theta}{\pi}) h_{botttom} \tag{3.11}$$

where θ was geometrically related to the void fraction by the following formula if the area occupied by the condensate film was neglected:

$$\alpha = \frac{\theta}{\pi} - \frac{\sin(2\theta)}{2\pi} \tag{3.12}$$

The heat transfer coefficient for the top, h_{top}, was evaluated from Chato's correlation, replacing the K_c value by:

$$K_c = \frac{0.23 Re_{vo}^{0.12}}{0.728(1 + 1.1 X_{tt}^{0.58})} \tag{3.13}$$

weher Re_{vo} is the vapour only Reynolds number. The heat transfer coefficient for the bottom was expressed as:

$$h_{bottom} = 0.0195 \frac{k_1}{D} Re_l^{0.8} Pr_l^{0.4} \phi_l \text{ , with } \phi_l = \sqrt{1.376 + \frac{C_1}{X_{tt}^{C_2}}} \tag{3.14}$$

$$\begin{cases} C_1 = 4.172 + 5.48 Fr_l - 1.564 Fr_l^2 \text{ and } C_2 = 1.773 - 0.169 Fr_l & \text{if } 0 \leq Fr_l \ll 0.17 \\ C_1 = 7.242 \text{ and } C_2 = 1.655 & \text{if } Fr_l > 0.17 \end{cases} \tag{3.15}$$

Several stratified and annular flow condensation correlations were established, which are suitable for different flow regimes or based on flow patterns [74–76]. Most of them have relatively complex forms, wide range application and good prediction accuracy. Some of the correlations discussed before and other relevant are detailed in tables 3.1 and 3.2, for gravity driven flows and stratified/annular flows (both gravity and surface tension are relevant) respectively.

Table 3.1: Heat transfer coefficient correlations for gravity driven flow inside horizontal round tubes.

Author	D_h[mm]	Fluid(s)	Range
Chato [58]	14.53-27.94	Air-Water, R-113	$Re_g < 35000$
Carey [53]	12.5	Steam	$12.6 < G < 145 \text{kg/m}^2.\text{s}$
Singh et al. [71]	11	R134a	$20 < G < 500 \text{kg/m}^2.\text{s}$
Dobson and Chato [72]	3.14-7.04	R-12, R-22, R-134a, R32/R125	$25 < G < 800 \text{kg/m}^2.\text{s}$

Table 3.2: Heat transfer coefficient correlations for stratified and annular flows inside horizontal tubes. C: circular; R: rectangular.

References	Geometry	$D_h[\mathrm{mm}]$	Fluid(s)	range
Wang et al. [74]	R	1.46	R-134a	$75 < G < 750\mathrm{kg/m^2.s}$
Thome et al. [75]	C	3.1–21.4	15 refrigerants	$24 < G < 1022\mathrm{kg/m^2.s}$
Cavallini et al. [76]	C	> 3	HCFCs, HFCs, HCs, CO2, NH4, H20	$50 < G < 800\mathrm{kg/m^2.s}$

3.3 Basic Heat Transfer Concepts

Some of the basic concepts required to understand heat transfer characteristics of heat exchanger surfaces are described in the following sub-section.

3.3.1 Basic Definitions

The fluid mean axial velocity is defined as the integrated average axial velocity with respect to the free-flow area A_o, where u is the local velocity distribution across the flow cross section:

$$u_m = \frac{1}{A_o} \int u dA \tag{3.16}$$

The peripheral mean wall temperature, and the fluid bulk temperature at an arbitrary duct cross section are defined as:

$$T_{w,m} = \frac{1}{P} \int T_w ds \tag{3.17}$$

$$T_m = \frac{1}{A_o u_m} \int u T dA \tag{3.18}$$

Where P is the duct perimeter and s is the spatial coordinate at a point on the duct wall along the inside perimeter. For a duct with uniform curvature, such as a circular tube, $T_w = T_{w,m}$. However, for a noncircular tube, T_w may not be uniform, but instead it will be dependent on the boundary condition. The fluid bulk temperature T_m in equation 3.18 is an enthalpy average over the flow cross section for constant ρc_p . However, if one idealizes uniform flow in a cross section with $u = u_m$, the T_m in equation 3.18 is the integrated average value over the cross section. The fluid bulk temperature is also referred to as the mixed mean fluid temperature or flow average temperature.

The convection heat flux can be simplified by introducing a concept of the heat transfer coefficient as a proportionality factor in Newton's law of cooling:

$$q'' = \begin{cases} h(T_w - T_m) & \text{(3.19a)} \\ h(T_w - T_\infty) & \text{(3.19b)} \end{cases}$$

Where the first relation is used for internal flow or heat exchangers, while the second equation 3.19b for

external flow. In the convection heat transfer process using 3.19a, only the wall temperature and fluid bulk temperature are involved for the determination of convective heat flux.

The case of study in the present work, plate fin heat exchanger with multi-louvered fin, addresses a confined flow where the boundary layers could interact depending on several variables such as the air-flow Reynolds number and other louver fin geometric parameters. For this reason, along this work, the air-flow was considered an internal flow. Combining Fourier's law and 3.19a, the heat transfer rate per unit surface area can be represented either as conduction or convection heat flux as follows:

$$q'' = -k\frac{\partial T}{\partial y}_{y=0} = h(T_w - T_m) \tag{3.20}$$

Consequently, the heat transfer coefficient is given by:

$$h = \frac{-k\frac{\partial T}{\partial y}_{y=0}}{T_w - T_m} \tag{3.21}$$

Where the heat transfer coefficient is, indeed, dependent on the temperature gradient at the wall. This equation 3.21 was used to calculate the heat transfer coefficient on the air-side of the heat exchanger.

Basic Concepts on Heat Transfer and Flow Friction

Usually the dimensionless heat transfer and pressure drop characteristics of a compact heat exchanger are obtained and presented in terms of Colburn j factor and Fanning f factor in function of Reynolds number, Re.

In this work, a numerical simulation of the heat transfer and pressure drop of compact heat exchangers with louvered fins and flat tubes was conducted. The value of Reynolds number based on louver pitch is calculated from:

$$Re_{L_p} = \frac{\rho u_c L_p}{\mu} \tag{3.22}$$

where L_p is louver pitch, u_c critical air velocity at the minimum free flow area A_c, ρ is the air density and μ the air dynamic viscosity. The air-side heat transfer characteristics is presented in terms of Colburn j factor and can be calculated as follows:

$$j = \frac{Nu}{Re_{L_p} Pr^{1/3}} = St.Pr^{2/3} \tag{3.23}$$

This factor is a modified Stanton number taking into account the moderate variations in the Prandtl number. The Santon number is the ratio of convected heat transfer to the enthalpy rate change of the fluid reaching the wall temperature.

The pressure drop equation by Kays and London [39] is used to calculate the heat exchanger core

Fanning friction factor as follows:

$$f = \frac{2\Delta p}{\rho u_c^2}\frac{A_c}{A_f} \tag{3.24}$$

Where Δp is the pressure drop and A_f, A_c are frontal air-side surface area and minimum free flow cross area respectively. The numerical simulation considered the absence of friction losses, so the core entrance and exit losses were neglected in the fanning friction factor calculation, simplifying the original expression defined by Kays and London [39].

The results were also evaluated using the volume goodness factor $j/f^{1/3}$ [77], adopted to evaluate the overall thermal-hydraulic performance and the enhanced heat transfer effect of the louver region fins.

3.4 Thermal Design Theory for Recuperators

3.4.1 Thermal Circuit

In heat exchanger analysis, the analog electric is very useful to calculate the thermal resistances defined as the ratio of a driving potential to the corresponding heat transfer rate $R = \Delta T/q$.

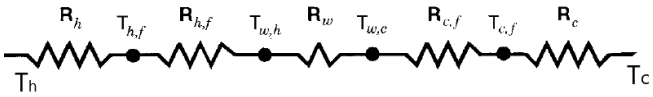

Figure 3.6: Thermal circuit for a heat exchanger.

The overall thermal resistance of the heat exchanger is considered as having three components in series: (1) cold side thermal resistance R_c, including the extended surface efficiency; (2) wall thermal resistance R_w; and (3) hot thermal resistance R_h, including the extended surface efficiency. No fouling or scale resistance is considered on either side, so the corresponding resistance is not included in the calculations in spite of be represented in figure 3.6. The wall thermal resistance is constant and the condensation heat transfer coefficients should be known a priori in order to calculate the overall thermal resistance.

$$dR_{tot} = dR_h + \cancelto{0}{dR_{h,f}} + dR_w + \cancelto{0}{dR_{c,f}} + dR_c \tag{3.25}$$

$$\frac{1}{UdA} = \frac{1}{(\eta_o h dA)_h} + dR_w + \frac{A_a}{(\eta_o h dA)_c} \tag{3.26}$$

$$\frac{1}{U_o} = \frac{A_a}{A_i h_i} + \frac{A_a \delta_w}{A_w k_w} + \frac{1}{\eta_{o,a} h_a} \tag{3.27}$$

Here the subscripts a and i denote the tube air-side and inside respectively. The term $\eta_{o,a}$ in equation 3.27 is extended surface efficiency of the air-side surface and is related to the fin efficiency of the

extended surface as follows:

$$\eta_{o,a} = 1 - \frac{A_f}{A_o}(1 - \eta_f), \quad \text{with} \quad \eta_f = \frac{tanh(ml)}{ml} \quad \text{and} \quad l = \frac{F_d}{2} - \delta_f \tag{3.28}$$

For many plate-fin surfaces, the relation for the straight fin with constant conduction cross section may be used to a good approximation. In that case, where $m = [\frac{2h}{k_f \delta_f}/(1 + \frac{\delta}{F_d})]^{\frac{1}{2}}$ and l is the fin length from the root to the center of the fin.

3.4.2 Effectiveness-Number of Transfer Units Method

In the ε-NTU method, the heat transfer rate from the hot fluid to the cold fluid in the exchanger is expressed as

$$q = \varepsilon C_{min}(T_{h,i} - T_{c,i}) = \varepsilon C_{min} \Delta T_{max} \tag{3.29}$$

where ε is the heat exchanger effectiveness, sometimes referred to in the literature as the thermal efficiency, C_{min} is the minimum of C_h and C_c; $\Delta T_{max} = T_{h,i} - T_{c,i}$ is the fluid inlet temperature difference. The heat exchanger effectiveness is nondimensional and it can be shown that in general it is dependent on the number of transfer units NTU, the heat capacity rate ratio C^*, and the flow arrangement for any heat exchanger:

$$\varepsilon = \phi(NTU, C^*, flow\ arrangement) \tag{3.30}$$

The three dimensionless groups, ε, C^*, and NTU are defined below.

Effectiveness ε

Effectiveness ε is a measure of thermal performance of a heat exchanger. It is defined for a given heat exchanger of any flow arrangement as a ratio of the actual heat transfer rate from the hot fluid to the cold fluid to the maximum possible heat transfer rate q_{max} thermodynamically permitted:

$$\varepsilon = \frac{q}{q_{max}} \tag{3.31}$$

An overall energy balance for the two fluid streams give the next equation 3.32, where h is the fluid specific enthalpy.

$$q = \dot{m}_h dh_h = \dot{m}_c dh_c \tag{3.32}$$

If occurs phase change, enthalpy differences should be replaced by enthalpies of phase change. However, c_p can be assumed as infinity for condensing or evaporating single-component fluid streams. Hence, the phase changing stream can be treated as a "single-phase" fluid having $\dot{m}c_p = \infty$ or $\Delta T = 0$ for isothermal evaporating or condensing (as this case of study). The q_{max} could be determined by the

next equation 3.33, independently of the flow arrangement, considering a heat exchanger with infinite surface area.

$$q_{max} = C_{min}(T_{h,i} - T_{c,i}) = C_{min}\Delta T_{max} \tag{3.33}$$

Using the actual heat transfer rate q from energy conservation equation and q_{max} from equations 3.32 and 3.33, the exchanger effectiveness ε of equation 3.31 valid for all flow arrangements is given by:

$$\varepsilon = \frac{C_h(T_{h,i} - T_{h,o})}{C_{min}(T_{h,i} - T_{c,i})} = \frac{C_c(T_{c,o} - T_{c,i})}{C_{min}(T_{h,i} - T_{c,i})} \tag{3.34}$$

Thus, ε can be determined directly from the operating temperatures and heat capacity rates. It should be emphasized here that $T_{h,o}$ and $T_{c,o}$ are the bulk outlet temperatures defined by equation 3.18.

Heat Capacity Rate C^*

Heat capacity rate ratio, C^* is simply a ratio of the smaller to larger heat capacity rate for the two fluid streams so that $C^* \leq 1$.

$$C^* = \frac{C_{min}}{C_{max}} = \frac{(\dot{m}c_p)_{min}}{(\dot{m}c_p)_{max}} \tag{3.35}$$

C^* is a heat exchanger operating parameter since it is dependent on mass flow rates and/or temperatures of the fluids in the exchanger. Let point out that for a condensing fluid at ideally constant temperature, the ΔT range is zero, and hence the heat capacity rate C approaches infinity for a finite heat rate. Then, in this case, the heat capacity rate ratio is $C^* = 0$ with C_{min} as finite and C_{max} approaching infinity in the sense just discussed. The $C^* = 0$ case with $C_{min} = (\dot{m}c_p) = 0$ is not of practical importance, since to have $\dot{m} = 0$ there is no flow on the C_{min} side of the exchanger.

Number of Transfer Units NTU

The number of transfer units is defined as a ratio of the overall thermal conductance to the smaller heat capacity rate:

$$NTU = \frac{1}{C_{min}} \int_A U dA \tag{3.36}$$

NTU designates the nondimensional heat transfer size or thermal size of the heat exchanger, and therefore it is a design parameter. With equation 3.36 it is possible to get the overall heat transfer coefficient (U_oA_o) for the heat exchanger as $U_oA_o = NTUC_{min}$.

For the special case of an evaporator or a condenser, as in this specific case of study, $C^* = 0$ and the exchanger effectiveness expression 3.30 reduces to 3.37 valid for all flow arrangements.

$$\varepsilon = 1 - exp(-NTU) \tag{3.37}$$

4. Condenser Design and Evaluation of the Most Relevant Design and Geometric Parameters to Develop the Thermosyphon

4.1 Working Fluid

The working fluid selection has an important role on the thermosyphon system performance, as the thermophysical properties of the chosen fluid influence the condensation, the nucleate boiling heat transfer as well as the critical heat flux. Several additional issues must be taken into account when selecting the working fluid, such as the material compatibility, the global environment impact, not be hazardous nor corrosive, stability of the working fluid under the operating conditions, cost and availability.

The working fluid selected in the present work was the hydrofluorether Novec^{TM} HFE-7000 manufactured by 3M^{TM}. This is an inert and dielectric fluid, which is recommended in order to meet the requirements of safety and reliability, considering the present context of electronic cooling applications. However, compared to other common fluids such as water, under similar working conditions, the thermal properties of a dielectric fluids such as the thermal conductivity, the heat capacity or the latent heat of vaporization have significantly lower values. This means that the devised system must be designed to overcome this disadvantage, being one of the main reasons of the great effort put in improving the performance of the evaporator and of the condenser.

HFE-7000 is a relatively new hydrofluoroether dielectric that has recently been proposed to replace FC-72, as it has similar thermophysical properties and better environmental characteristics (lower Global Warming Potential (GWP)). Furthermore, as its latent heat of vaporisation is greater, it allows achieving higher heat transfer coefficients at larger critical heat fluxes (CHF). While several studies have dealt with the boiling of the fluorinert FC-72, few have investigated HFE-7000.

Table 4.1: 3M^{TM} Novec^{TM} HFE-7000 thermophysical properties at 25°C, 1 atm.

$T_{sat}[^{\circ}\mathrm{C}]$	$\rho_l[\mathrm{kg/m^3}]$	$\rho_g[\mathrm{kg/m^3}]$	$\mu_l[\mathrm{N.s/m}]$	$c_{p,l}[\mathrm{J/kg.K}]$	$k_l[\mathrm{W/m.K}]$	$h_{fg}[\mathrm{J/kg}]$	$\sigma[\mathrm{N/m}]$
34	1386.2	8.22	4.31×10^{-4}	1327.93	0.075	132.16×10^{3}	12.4×10^{-3}

An important feature is the solubility of air in the HFE-7000 (approximately 35% volume of air in fluid), which affects the boiling heat transfer. The onset of boiling, the nucleate boiling and also the condensation may be affected due to the presence of non-condensable gases in the system. Furthermore, the dissolved air causes higher saturation pressures which consequently deteriorate the system thermal resistance. Therefore, a degassing procedure is a vital step, which was executed at the beginning of each test.

The thermophysical properties of the HFE-7000 presented in table 4.1 are temperature dependents, being some of the dependency relations provided by 3M™. For instance, the pressure-temperature relation along the saturation curve, equation 4.1, being used throughout in this work is given by the manufacturer:

$$ln(p.10^6[MPa]) = -\frac{3548.6}{T[K]} + 22.978, \quad 243 < T[K] < T_{critic} \quad \text{and} \quad T_{critic} = 437.7K \pm 1 \tag{4.1}$$

HFE-7000 working fluid has some material incompatibilities issues that must be taken into account in the selection materials before the assembly. Following the research on this topic realized by Moura [28], it was concluded that elastomers with excess of plasticizers and additives are incompatible materials, which can cause the polymer to harden, crack or shrink. Samples of the used polymeric materials were submerged into an one week HFE-7000 bath in order to prove the material compatibility. Teflon anaerobic adhesive and Viton O-rings showed positive results and therefore were used for sealing purposes. Note that the working fluid is also compatible with metals (copper and brass used in the condenser).

4.2 Evaporator Design

A cylindrical design tube was chosen for the evaporator since the hot surfaces to test are circular. Taking into account previous work developed by [28, 33], a clear acrylic tube with internal diameter of 32mm and height of 40mm was used for the main body of the evaporator. The outer diameter of the cylinder is 40mm, which allows for the wall thickness to be large enough (4mm) to resist the considerate compression load applied to properly seal the assembly and to resist to the radial strength due to pressure variations. Manufacturer Acrilfer was chosen as the supplier for the acrylic components. Several machining works for the manufacturing of the evaporator for horizontal and vertical setups with the pretended size, threaded holes and O-ring grooves were performed during this work in the university department's shop floor. A technical draw of the evaporator designed to be used either horizontally or vertically is illustrated in figure 4.1.

The diameter of the threaded holes (evaporator inlet and outlet) were selected according to the maximum allowed pressure losses calculated with the Darcy–Weisbach equation [78], assuming that

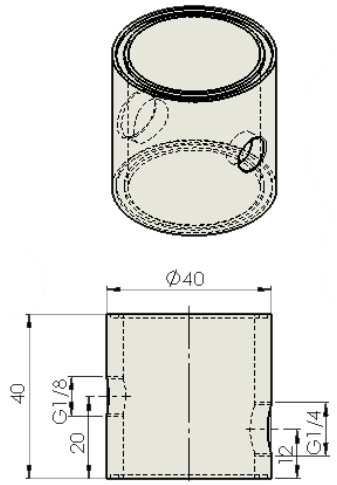

Figure 4.1: 32$\emptyset_i$x40mm evaporator (units in mm).

the friction losses occurring in liquid line must be lower than the positive pressure head of liquid column. The positive pressure head, calculated by the height difference between the condenser and the entrance of the evaporator, should be able to drive 1.36$\mathrm{ml/s}$ across the tube length. This results in a minimum tube inner diameter of 1.8mm. Thus, a 3mm inner diameter PVC tube was used for the liquid line and a 9mm inner diameter PVC tube was used for vapour line due to material and feasibility constrains.

The bottom open end of the tube is closed by the hot surface, using a Viton™ O-ring and the Teflon™ adhesive for sealing under pressure. Due to its very small surface tension, HFE-7000 can effectively drain through very tiny leaks. Hence a Loxeal® anaerobic adhesive, which gains consistency under pressure, was used for extra sealing. The top open end of the cylinder was sealed by another acrylic part, a square block with a groove for an additional O-ring and two threaded holes to connect pipe couplings leading to the condenser, placed above the evaporator. The anaerobic adhesive is here again used for extra sealing guarantee.

4.3 Condenser Design

Plate Fin Heat Exchangers (PFHEs) are recognized as one of the most efficient, standard, and compact type of heat transfer devices. These heat exchangers have unique features and considerable advantages when compared with the remaining on the market. High efficiency, small size, light weight and low cost are the desirable and relevant criteria in the fabrication of these types of compact heat exchangers. Heat transfer and hydrodynamic processes of the PFHEs are strongly influenced by the configuration and geometrical parameters of extended surfaces. Plate fins are categorized as (1) plain, such as plain triangular and rectangular fins, (2) plain but wavy fins, and (3) interrupted fins, such as offset strip, louver, perforated, and pin fins. An example of some of these geometries is shown in figure

4.2.

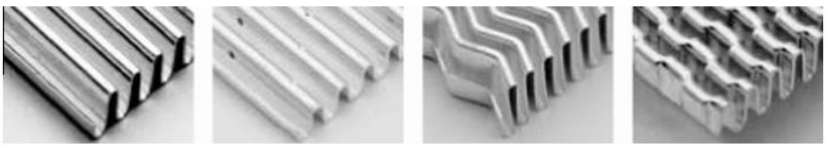

Figure 4.2: Plate fin heat exchangers geometries: plain, perforated, wavy and offset strip (from left to right).

The fins are used depending of the application. In this work louvered fins were considered on the external side that form the individual air-flow passages. This louvered fin PFHE used as condenser is a cross-flow heat exchanger with flat tubes, where the flat tubes separate the two fluid streams (air and coolant) and the fins are only used on the air-side.

4.3.1 Louvered Fins

The compact heat exchanger selected in the present work - a corrugated multi-louver fin and flat tube heat exchanger is widely used in automotive, air-conditioning and refrigeration systems, where high efficiency, low cost, small volume and light weight are vital requirements to fulfill. This type of fin array has several advantages. Hence, the main concept of the louvers is interrupt the airflow and create a series of thin boundary layers that have lower thermal resistance. Besides that, the finned structure increases the surface contact area due to high level of compactness, resulting in heat transfer improvements. This configuration with flat tubes also provides lower drop pressures, when compared with conventional round tubes, due to smaller projected frontal area causing less profile drag. These type of fins is schematically represented on figure 4.3(a), being the geometric parameters detailed in figure 4.3(b).

Over the years, several studies were performed to determine the air-side heat transfer coefficient and pressure drop, mainly evaluated in terms of the Colburn j factor and fanning friction factor f. A large number of experiments were performed by Chang and Wang [80], Kim and Bullard [81] and Chang et al. [82] to calculate the air-side heat transfer and pressure drop data. Cowell et al. [83] showed that the flow pattern can be characterized in terms of duct-directed and louvered-directed flows, which is a function of the Reynolds number based on louver pitch. At high velocities, the boundary layers are thinner and the flow follows the direction of the louvers (louver directed), increasing heat transfer. Conversely, at low velocities, the boundary layers are thick, which block the gap between adjacent louvers and make the flow duct-directed, characterized by a very poor heat transfer performance. The most important drawback of louvered fins is associated to high pressure loss if compared to the plain fin. To understand if this type of finned plate heat exchanger would be efficiently applied as condenser into this two-phase system, and if the fan's Revolutions Per Minute (RPM) speed was enough to effectively improve the heat transfer, a numerical Computational Fluid Dynamics (CFD) simulation was performed.

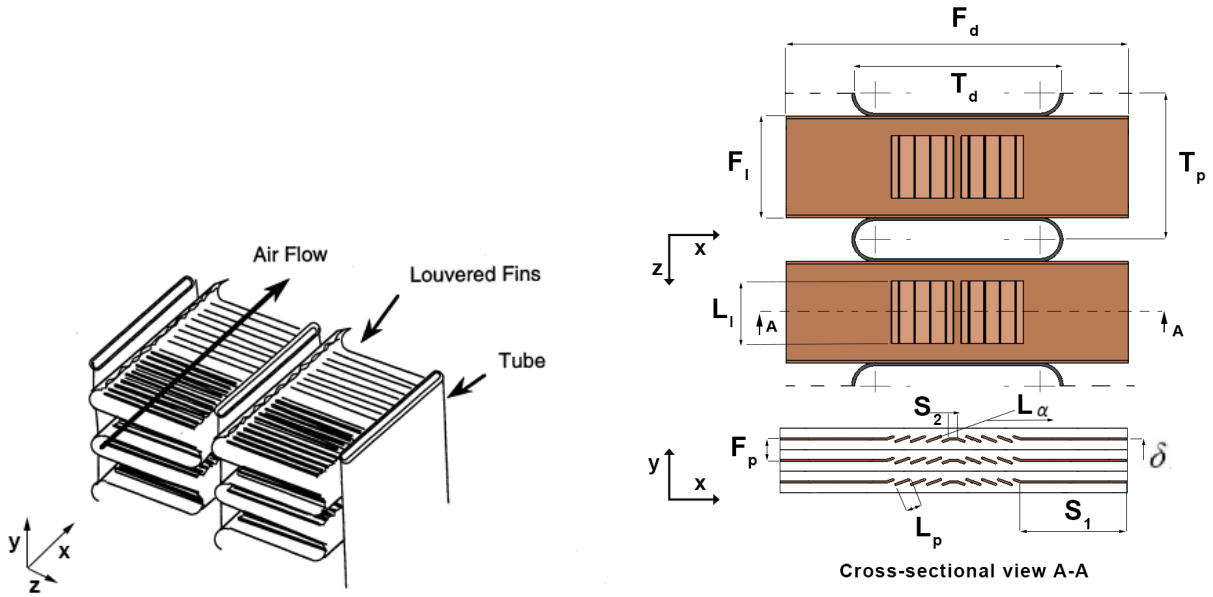

(a) (b)

Figure 4.3: Detailed heat exchanger with corrugated multi-louvered fins and flat tubes. **a)** 3D draw adapted from [79]; **b)** Plane and side view and definitions of geometric parameters.

4.3.2 Numerical Simulation: Sensitivity Analysis of the Relevant Parameters in the Design of the Condenser

Very few studies are reported in the literature for the specific geometric parameters and flow conditions which are required for the present study. Therefore, a numerical CFD simulation was performed on the air-side of the multi-louvered fin and flat tube in order to infer on the heat transfer performance and on the design compactness. This numerical analysis has been conducted for different geometric configurations, in the laminar range of Reynolds number based on the louver pitch between 20–250.

Computational Domain

On the schematic diagram displayed in figure 4.3(a), it is visible the flattened rectangular tubes and the corrugated multi-louvered fins where the refrigerant (dielectric fluid HFE-7000) and air passes through respectively. The louvered plate is periodically folded and then bonded to the surface of the flattened tube, forming the confined flow channels through which air passes over the louvers. Inspecting the schematic representation, one can clearly identify a geometric periodicity and symmetry which can be used to simplify the problem to only one fin and half of each flat tube. Therefore, it was not necessary to solve the problem for the global heat exchanger.

The model was divided into three main domains: the air-flow domain, the flat tube domain and the

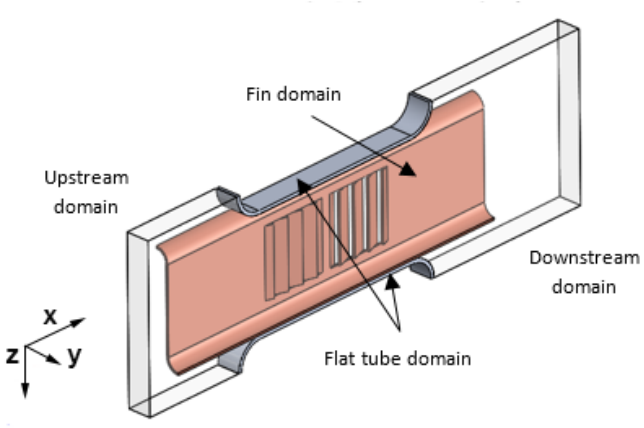

Figure 4.4: 3D computational domain.

fin domain. To fulfill the boundary conditions, which will be discussed in the next section, the fluid domain was extended at the inlet (upstream), to allow a uniform air-flow and especially at the outlet (downstream), in order to have a developed flow in the streamwise direction. Figure 4.4 identifies the different domains: the louvered fin is represented in copper color, the flat tube is in gray, while the shaded volume represents the air domain.

The initial geometry depicted in figure 4.5 was chosen taking into account the standard condenser geometries and also the fin dimensions addressed in the correlations reported in the literature. This detailed geometry was initially considered only for validation purposes.

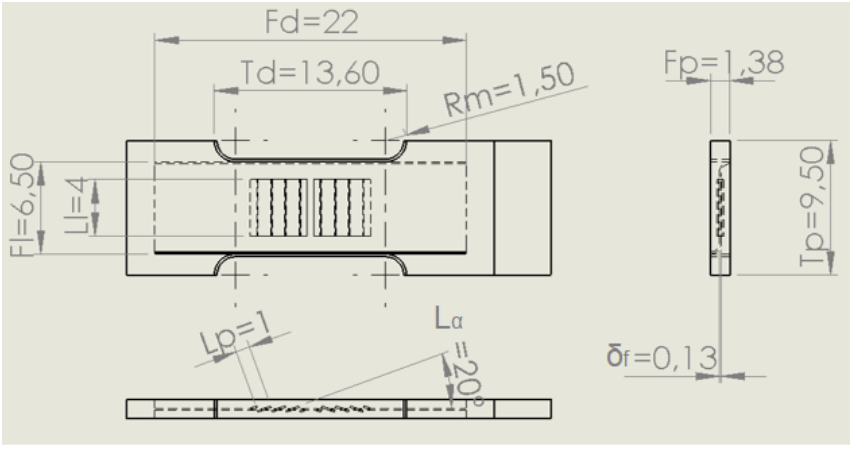

Figure 4.5: Initial detailed geometry in millimetres.

Different heat exchanger configurations were also tested, in the numerical simulation, to infer on those which can potentially provide improved heat transfer rates. Within this scope several geometric parameters were varied, namely the louver angle (L_α), the louver length (L_l), the louver pitch (L_p), louver number (N_l), redirection length (S_2) and fin pitch (F_p), while some fin dimensions, as fin thickness (δ_f), fin depth (F_d) and fin length (F_l) were kept constant at 0.13mm , 22mm and 6.5mm respectively.

The range considered to vary these parameters was establish to respect the CPU dimensions and the manufacturing limitations.

Governing Equations

This is a 3D dimensional convective heat transfer problem, where the fluid motion is governed by the Navier-Stokes and continuity equations coupled with the energy conservation equation. In non-conservative form, these equations can be written as:

$$\frac{D\rho}{Dt} + \rho\nabla.\vec{u} = 0 \tag{4.2}$$

$$\rho\frac{D\vec{u}}{Dt} = -\nabla p + \nabla\bar{\tau} + \rho\vec{f} \tag{4.3}$$

$$\rho\frac{De}{Dt} = -p\nabla.\vec{u} + \nabla.(k\nabla T) + \phi + Q \quad , with \quad \phi = (\bar{\tau}.\nabla)\vec{u} \tag{4.4}$$

Where ρ is the fluid density, $\vec{u}$ the velocity vector, $\vec{\tau}$ the viscous stress tensor, $\vec{f}$ the body force per unite of mass acting on the fluid, p pressure, e the specific internal energy, k thermal conductivity and Q is the heat generation rate per unit volume. The first equation results from mass conservation and is known as the continuity equation. The second is a set of equations (one for each dimension) that describes the linear momentum conservation. Finally, the third equation represents the energy balance and is applied for the flow and solid domain.

To simplify the previous governing equations, several assumptions were taken in consideration. The fluid was assumed as isotropic and Newtonian and the stress tensor only depends of the velocity gradient. The flow is considered to be incompressible, since the air velocity is much lower than the speed of sound. This assumption is evaluated based on the fact that the Mach number, which represents the local flow velocity divided by the speed of sound in the medium. The assumption of incompressibility is valid since $Ma =$ 0.02, which fulfills the condition of $Ma <$ 0.3, meaning that density variation along the space can be neglected. Due to the very low Mach number, the viscous dissipation effect, as well as the work done by pressure changes were neglected.

The transition from laminar to turbulent flow is dependent on the entrance configuration, flow passage geometry, whether or not the surface is interrupted, surface roughness, natural convection effects, flow pulsation and even the change of viscosity when large heating rates occur. So, for a plate finned heat exchanger, not being a smooth circular tube, the transition flow is even more uncertain. Therefore, classifying the flow on a corrugated multi-louvered fin as laminar or turbulent, is a difficult task. In fact, there may be regions of laminar, laminar unsteady, transitional, and turbulent flows all coexisting in a heat exchanger complex flow passage. In the numerical simulation, the air-flow was assumed as laminar, which is a reasonable consideration for the range of Reynolds numbers addressed here $Re_{Lp} <$

1200, according to Antoniou et al. [84].

Tafti et al. [85, 86] performed several studies where they estimated that the flow instability starts to appear outside of the louver bank for $Re_{Lp} = 400$. Tafti et al. [85,86] also concluded that only at $Re_{Lp} = 1300$ the air-flow at all louvers exhibits unsteadiness. Therefore, a steady-state analysis is valid for the applied range Re_{Lp} conditions. Note that a steady-state analysis means constant flow rates and fluid temperatures (at the inlet and within the exchanger) independent of time.

Since $\rho = cst.$, applying the incompressible substance model $c_v = c_p$ and consequently the internal energy is defined as $de = c_p dT$. The heat transfer by radiation was also neglected in the energy balance due to the low temperatures observed in the current problem (25°C - 34°C).

With all these assumptions, it was possible to derive and get the following simplified expressions:

$$\nabla . \vec{u} = 0 \tag{4.5}$$

$$\vec{u} . \nabla \vec{u} = -\frac{\nabla p}{\rho} + \nu \nabla^2 \vec{u} \tag{4.6}$$

$$\rho c_p \vec{u} . \nabla T = \nabla . (k \nabla T) + Q \tag{4.7}$$

Where ν is kinematic viscosity, p the gauge pressure and c_p the heat capacity. The gravity effect was also disregarded from the momentum since atmospheric relative pressure (gauge pressure) was used. The solid, such as the tube walls and fin, is assumed as an isotropic body with temperature-dependent heat transfer, according with the Fourier's law. Despite the flow incompressibility, all the fluid properties (density, thermal conductivity, heat capacity, viscosity) in the numerical simulation, are temperature-dependent due to the non-isothermal characteristic of the problem. Applying the previous governing equations, a numerical simulation was computed in COMSOL Multiphysics® v5.2.

Boundary Conditions

Rectangular Cartesian coordinates system (x,y,z) were used, with x representing streamwise direction, y wall normal direction and z spanwise direction.

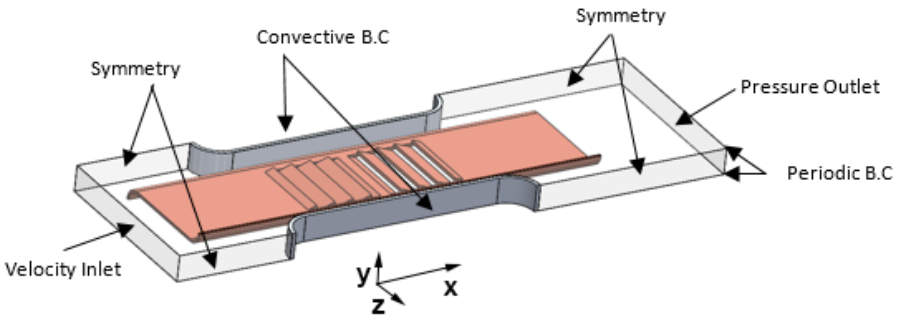

Figure 4.6: Boundary conditions of the computational domain.

A symmetric boundary condition was applied to the lateral faces, parallel to x-y plan, of upstream and downstream air domain, assuming a zero flux of all quantities across these surfaces. This condition was applied because the flow and the thermal solution have a symmetry pattern which is useful to reduce the extent of the computational model. A periodic boundary condition was used for longitudinal faces of air domain, top and bottom parallel to x-z, in order to implement standard periodicity.

Navier-Stokes boundary conditions

At the inlet surface a normal inflow velocity u_{in} ($u_y = u_z = 0$) was imposed according to the specified air mass flow rate. It is worth mentioning that air velocity depends on the rpm's fan and could reach the critical speed of $3\mathrm{m/s}$, corresponding to $Re_{Lp} \approx 250$ (based on the louver pitch). On the opposite face, at the outlet, a zero gauge pressure was imposed. However, this condition can lead to an unstable solution for the low Reynolds numbers used here, so the flow at the outlet was assumed to have only a normal velocity component (null tangential velocity). No slip boundary condition was imposed at solid walls, $\vec{u} = 0$, including all the fin surfaces and the exterior walls of the flat tubes.

Energy conservation boundary conditions

A constant temperature T_∞ was applied at the inlet of the fluid domain, imposed by the inflow air temperature. At the outlet, an outflow condition was imposed, assuming a convection dominant thermal problem, which results in a null temperature gradient in the normal direction ($(k\nabla T).\vec{n} = 0 \Rightarrow \frac{\partial T}{\partial x} = 0$). At the internal faces of the flat tubes, a convective boundary condition was imposed, $q'' = h_i(T_{sat} - T_w)$, simulating the latent heat released by the phase change of the refrigerant, with both, the fluid saturation temperature, T_{sat} and convective heat transfer coefficient, h_i, constant and known. A continuous flux was imposed at fluid-solid interface ($k_{sl}\frac{\partial T_{sl}}{\partial n} = k_{fl}\frac{\partial T_{fl}}{\partial n}$) and temperature ($T_{sl} = T_{fl}$).

Numerical Solver

COMSOL Multiphysics® uses the Finite Element Method (FEM) to approximate solutions to boundary value problems. A conjugated heat transfer problem was solved in COMSOL, coupling the heat transfer in solids and fluids in order to assure a continuous flux and temperature across the interface solid-fluid. In the solid, the thermal energy is transported by conduction (in the brass flat tubes and copper fins), while in the air-flow the heat is mainly transported by convection and conduction. The air-flow is non-isothermal, so the software solves the governing equations (4.5, 4.6 and 4.7) considering the properties to be temperature-dependent.

The problem was solved with a segregated model, as this requires less memory and has a faster

convergence. However, the convergence is not always guaranteed, because segregated solvers are not unconditionally stable. The idea of segregated solvers is to solve each governing equation separately.

In this study, segregated parametric solvers were used in two steps, for the fluid flow (u, v, w and p) and heat transfer (T) module. An iterative GMRE solver was implemented in the first module, since the convective term of the Navier Stokes equations is non-linear. The pre-conditioner solver was a Geometric Multigrid with SCGS like pre and post smoother and Parallel Sparse Direct Linear Solver (PARDISO) as coarse solver. To reach a faster convergence, in the second segregated step, the heat transfer equation was solved with Multifrontal Massively Parallel Sparse Direct Solver (MUMPS). Moreover, streamline and crosswind diffusion techniques of stabilization were used for both fluid flow and heat transfer modules.

Mesh Settings

Due to the model's complex geometry, the mesh was generated automatically, with the physics-controlled mesh mode of COMSOL. An unstructured grid was generated with free triangular mesh (tetrahedral elements, pyramids and prisms are the most used) within the flow stream away from the walls, while boundary layers were added close to the walls. Since the velocity changes very rapidly in the direction normal to the wall, close to the boundary and very little in the tangential direction of the wall, the mesh at the boundary layers was refined and made to consist of quadrilateral elements tightly packed in the direction normal to the wall and more sparsely in the tangential direction. The mesh was more refined at the corners and at the edges in order to obtain a better accuracy.

A mesh analysis was performed, where the number of finite elements was increased as summarized in table 4.2, in order to avoid any mesh dependence results. The quantity of interest, that evaluates the air-side thermal performance was the Colburn j factor.

Table 4.2: Mesh properties.

Mesh	Total No. of elements	Maximum element size (mm)	Near wall element size (mm)	Computation time (min)
Extra Coarse	107111	1.28	5.06E-1	6
Coarser	229985	7.79E-1	1.17E-1	15
Coarse	650677	5.06E-1	7.79E-2	50
Normal	1488934	3.89E-1	3.89E-2	140
Fine	4658487	2-61E-1	1.56E-2	2100

Steady-state simulations were conducted for all structured meshes at frontal air velocity of $2\mathrm{m/s}$. Colburn j factor and the computational cost parameters were documented and compared for all the meshes. Colburn j factor against the grid size of free triangular mesh is shown in figure 4.7. Computational results show that the variation in the j factor tends to converge when the mesh is refined. However, more resources would be needed to compute the model with a greater number of elements and obtain a better convergence.

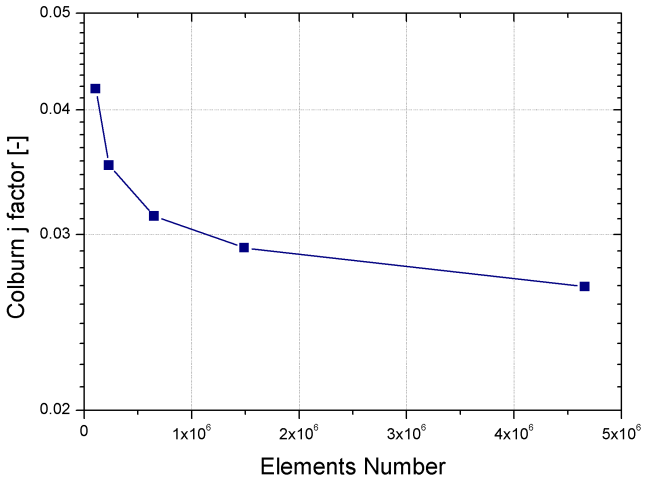

Figure 4.7: Variation of Colburn j factor for different grid sizes.

The computational cost, that includes the computation time and allocated memory is several times higher for normal and fine mesh. Therefore, due to the aforementioned reasons, a coarse mesh was selected for all the simulations in the present study, to improve the simulation speed.

4.3.3 Results

The air-side mean heat transfer coefficient was reported as the Colburn j factor and the mean drop pressure was evaluated using the Fanning friction factor. These parameters were chosen to allow a comparative analysis with previous studies reported in the literature, which is useful for validation purposes. The expressions used to calculate these quantities are given in Eqs. 3.23 and 3.24. In the data processing, all the fluid properties were assumed as constant, $\bar{\mu}, \bar{k}, \bar{C_p}, \bar{\rho}$, to facilitate the calculations and results presentation. The CFD variables ($T, \vec{u}, p$ – unknowns of the problem) were successively exported and processed separately, in a Matlab code, to predict the variables of interest. All the results depicted and discussed in this section were obtained with the input parameters presented in Table 4.3.

Table 4.3: Input variables

variable	unit	value
u_{in}	$\mathrm{m/s}$	$0-3$
T_{sat}	$^{\circ}\mathrm{C}$	34
T_{∞}	$^{\circ}\mathrm{C}$	25
h_i	$\mathrm{W/m^2.K}$	2000

The heat transfer coefficient values were predicted considering an internal flow, equation 3.19a, where the heat flux is directly determined by the commercial software. The outlet bulk temperature and

the wall temperature were calculated according to the definitions provided in equations 3.18 and 3.17 respectively.

Considering the flow as a steady-problem, the heat transfer, more precisely latent heat term, dissipated from the flat tubes equals the sensible heat absorbed by the air-side. Hence, the heat transfer rate value can be calculated by a simple energy balance at the air-flow channel, between the outlet and inlet surfaces ($q = \int \rho c_p u T ds_{out} - \int \rho c_p u T ds_{in}$).

Validation

A validation exercise was performed to check on the validity of the results for the imposed conditions on the model and on its boundaries. This analysis showed that mass, momentum and energy were successful conserved. Afterwards, still for validation purposes, a numerical simulation was performed, where the initial geometry was kept constant, as presented in figure 4.5, being the numerical results compared with those obtained from the effectiveness-NTU method.

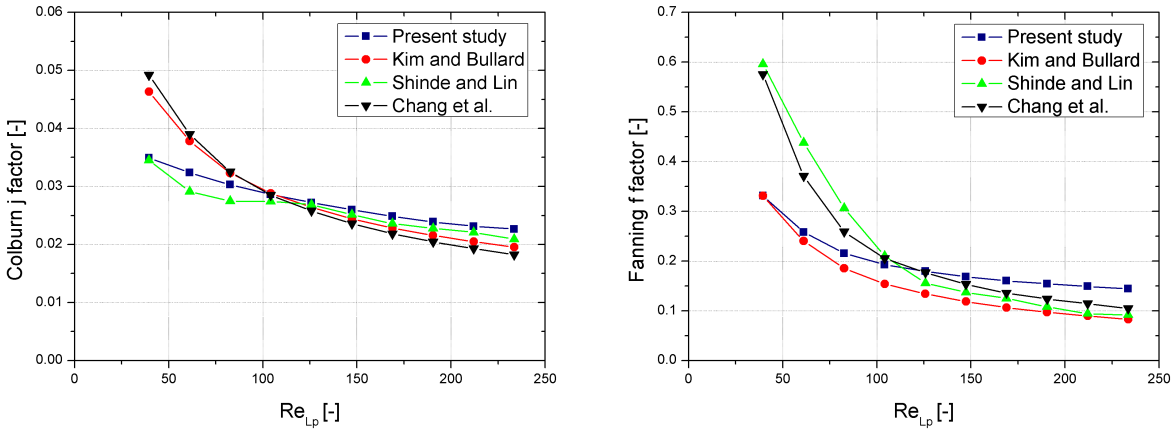

Figure 4.8: Comparation between CFD results and existent correlations. **a)** Colburn factor. **b)** Fanning factor.

Chang et al. [82], Chang and Wang [80], Kim and Bullard [81] and Shinde and Linde [87] report some of the few existing empirical correlations, valid for this corrugated multi-louver geometry and for this specific range of working conditions (Reynolds number). Therefore, these correlations were used to validate the numerical results, as depicted figure 4.8, where the the Colburn j factor and the Fanning friction factor are represented as a function of the louver pitch Reynolds number. These results show that both, j and f factors, exhibit a decreasing trend with increasing Reynolds numbers, which is generally in agreement with the trends reported in the literature [80–82, 87].

Furthermore, figure 4.8(a) shows that, for the Colburn j factor, the numerical data obtained here is in very good agreement with the Shinde and Lin correlation [87], presenting a maximum relative error of 10%. However, for the Fanning friction factor, shown in figure 4.8(b), there is a considerable deviation

between the numerical data and the Shinde and Lin correlation [87], particularly for low Reynolds number ($Re_{L_p} < 100$) getting an error of 80%. This deviation observed for the friction factor may be due to fouling, local flow contraction and expansion losses, which are neglected in the numerical model and have a considerable effect under experimental conditions, mainly at low flow speeds. Thus, it affects the empirical correlations, which are known to be very sensitive to the particular working conditions for which the experimental data was obtained. Surface roughness, which was not taken into account in the model, may also effect the Fanning factor, as reported by Shah [88] for compact flows passages.

Shinde and Lin [87] reported that 85% of the experimental test data were used to develop the j and f factor correlations, within an maximum root mean square error of $\pm$22.12% and $\pm$13.53% respectively as plotted in figure 4.9. Despite the friction factor nonconformity, this correlation was chosen to proceed with the validation process.

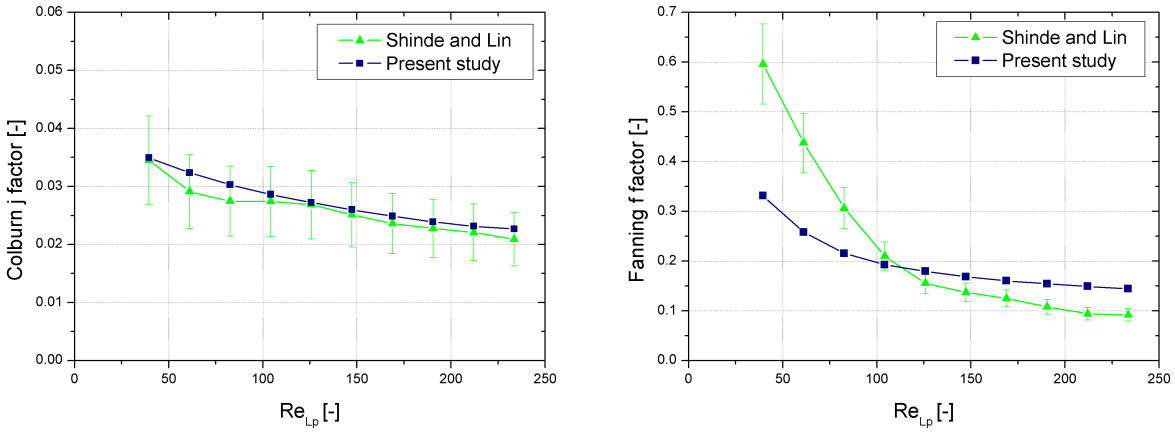

Figure 4.9: Numerical results validation with Shinde and Lin correlation [87]. **a)** Colburn factor. **b)** Fanning factor.

Knowing Colburn j factor values allows predicting, for a given core size, the mean outlet temperature and consequently the heat transfer rate. Applying an iterative ε-NTU procedure, as proposed by Shah [88] and known as rating problem, the variables of interest were calculated. This procedure consists in solving, iteratively, the effectiveness-NTU method and the analogue electric expressions for a plate-fin heat exchanger with $C^* = 0$ (phase change). The iterative process starts with a guessed initially outlet temperature until convergence is achieved, within the set value degree of accuracy.

It is worth mentioning that all the geometric properties have to be known to determine the Reynolds number and, consequently, determine Colburn and Fanning factors. To compute the total conductance U_o, the total thermal resistance from the air to the coolant was formulated as shown in equation 3.27, with the fin efficiency and extended surface efficiency calculated as assumed in equation 3.28. NTU was determined by the definition of number of transfer units, expression 3.36 and the effectiveness was evaluated using equation 3.37. Finally, the temperature is recalculated by an energy balance, taking into

account equation 3.34 of the effectiveness method.

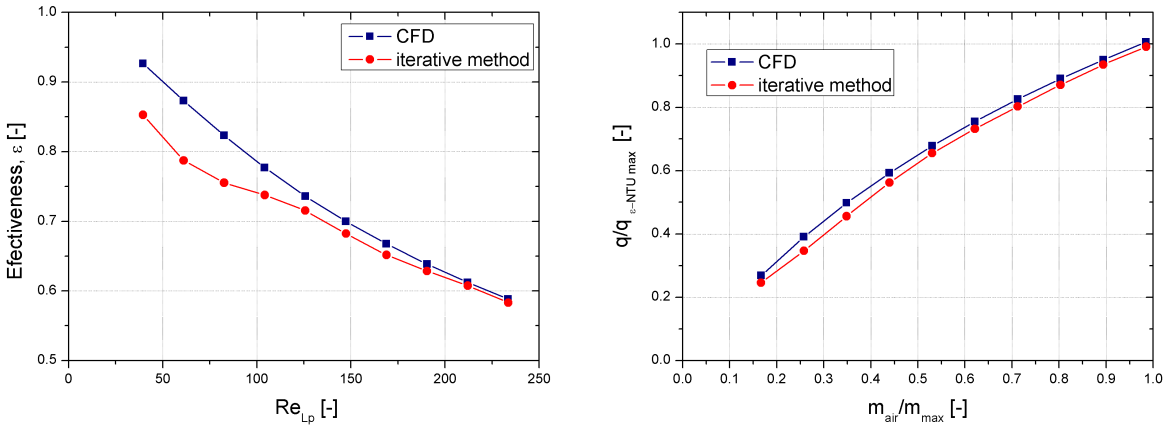

Figure 4.10: CFD results validation with an iterative ε-NTU procedure [88]. **a)** Effectiveness results. **b)** Heat transfer rate results.

The numerical outlet temperature and heat transfer rate values were compared with the results obtained with the ε-NTU iterative method for the applied Reynolds number. As shown in figure 4.10, a reasonable agreement is attained where the relative deviation tends to be reduced, as the air-flow speed increases, with a relative error of 1.1$\%$ at maximum flow speed. This is an acceptable value, taking into account that the heat transfer rate is the main quantity of interest for this study. So, the results discussed here allow validating the CFD model and extrapolate the simulation to other core dimensions, as well as different finned parameters.

Parametric Optimization Process

A sensitivity analysis including fin pitch F_p, louver pitch L_p, louver angle L_α, louver length L_l, redirection length S_2 and louver number N_l was extensively performed. Within this scope, these geometric parameters were varied once at a time to obtain the best heat transfer performance possible, which was evaluated based on the Colburn and Fanning factors (equations 3.23 and 3.24), as well as on the goodness factor which infers a valuable thermal-hydraulic performance quantification. This is still a basic analysis, only valid for the range of Reynolds number of 20–250.

Effect of fin pitch variation F_p

The variation of the Colburn factor with respect to the Reynolds number based on the louver pitch is illustrated in figure 4.11(a). The figure shows a proportional decrease in the j factor, with the increase of the air-flow speed, for a given fin pitch. For a certain fixed Reynolds number, the value of the convective heat transfer coefficient tends to decrease as the fin pitch decreases, due to the mixing of the thermal

boundary layer between surfaces. On the other hand, an increase in the Colburn factor of 7.2% is observed when the fin pitch is varied from 1mm to 1.38mm, at maximum Reynolds number (air speed of 3m/s).

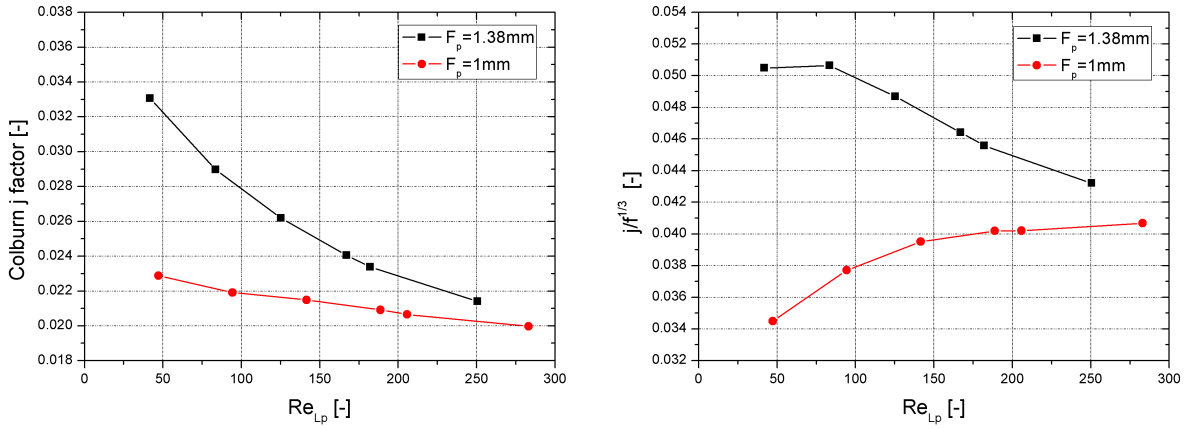

Figure 4.11: Thermal-hydraulic behavior corresponding to fin pitch variation at different Reynolds number. **a)** Colburn j factor **b)** Goodness factor.

In fact [89] reported that, for low Reynolds numbers ($Re_{L_p} < 300$), the j factor decreases as the fin pitch decreases, while the reverse is observed at high Reynolds numbers ($Re_{L_p} > 300$), where the j increases as the F_p decreases. This transition Reynolds number depends also on other parameters such as the louver angle and louver length. The effect of fin pitch on the heat transfer described here is consistent with that reported in the literature [81].

On the other hand, the Fanning factor increases with the decrease in the fin pitch, for all flow conditions tested here. The fin pitch reduction leads to a corresponding increase in the surface area, for a given heat exchanger core volume, which in turn, provides higher air-flow speed and higher resistance. This explains why the friction losses are higher for $F_p = 1\text{mm}$ deteriorating the goodness factor as shown in 4.11(b).

For a given heat exchanger core volume, the surface area density will increase in proportion to the decrease in size of F_p. This increase provides a wider surface area to enhance the heat transfer rate. So, although the heat transfer coefficient tends to be reduced as F_p decreases, the heat rate is not deteriorated for a fixed Reynolds number.

Louver pitch L_p

Figure 4.12(a) depicts the Colburn factor as a function of the Reynolds number, for three different louver pitches (0.9, 1 and 1.1mm). The figure evidences that the heat transfer is strongly dependent on the Reynolds number, so the optimum louver pitch parameter was chosen taking into account the

maximum applied Reynolds number value.

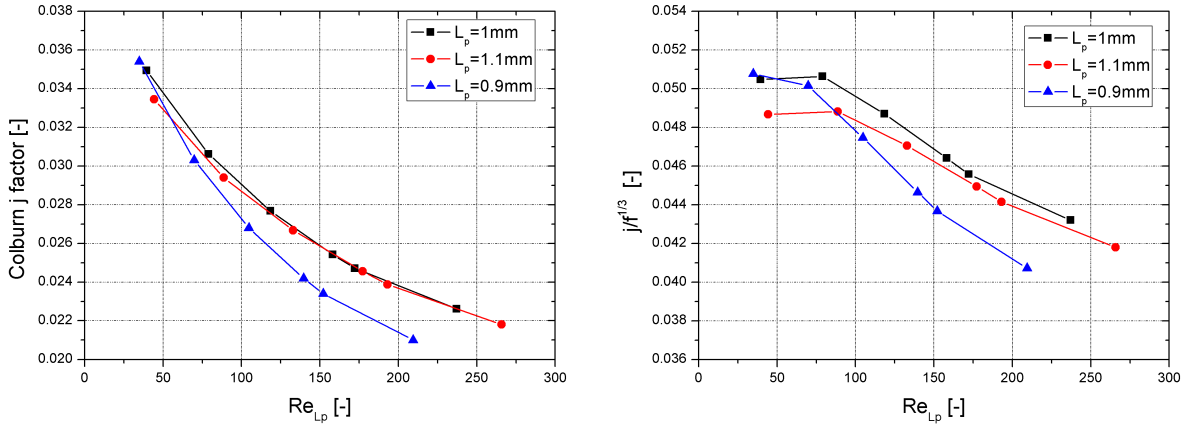

Figure 4.12: Thermal-hydraulic behavior corresponding to louver pitch variation at different Reynolds number. **a)** Colburn j factor **b)** Goodness factor.

On the other hand, the Fanning factor is observed to increase with the increase in the louver pitch, as expected. The increase in L_p leads to a corresponding increase in the surface area, for a given volume, which in turn, provides higher resistance (drag and friction) on the air-flow side.

In summary, increasing the louver pitch contributes to obtain higher heat transfer coefficients, but only until a certain louver pitch value. To have a clearer view of this trend, the goodness factor was plotted in figure 4.12(b) as function of the louver pitch reynolds number. At maximum air-flow speed, the highest values was obtained for $Lp = 1\text{mm}$. Further increasing the louver pitch has a negative effect on the pressure drop which consequently affects the heat transfer coefficient. Hence, beyond this value of the louver pitch of $Lp = 1\text{mm}$, the surface area becomes the sole variable which contributes to improve the heat transfer rate.

Louver angle L_α

Figure 4.13 shows, as expected, a trend of the Colburn factor to increase when the louver angle is increased, which is particularly evident at Reynolds numbers higher than 200 ($Re_{L_p} > 200$). Increasing 30% the louver inclination from 20 to 26 degrees, the Colburn j factor is augmented 3.4$\%$ at maximum air-flow speed, which results in a heat transfer coefficient improvement of 9.2$\%$.

The louver angle plays an essential role in the heat transfer and in the fluid flow mechanisms in the air-flow. Increasing the louver angle turns the flow more louver-directed, leading to higher heat transfer rates. The fluid travels larger distances through the fin, improving the mixing between cold and hot air. Moreover, the air-flow velocity passing among the louvers is increased, causing thinner boundary layers around them. However, large louver angles are more prone to develop large recirculation zones on

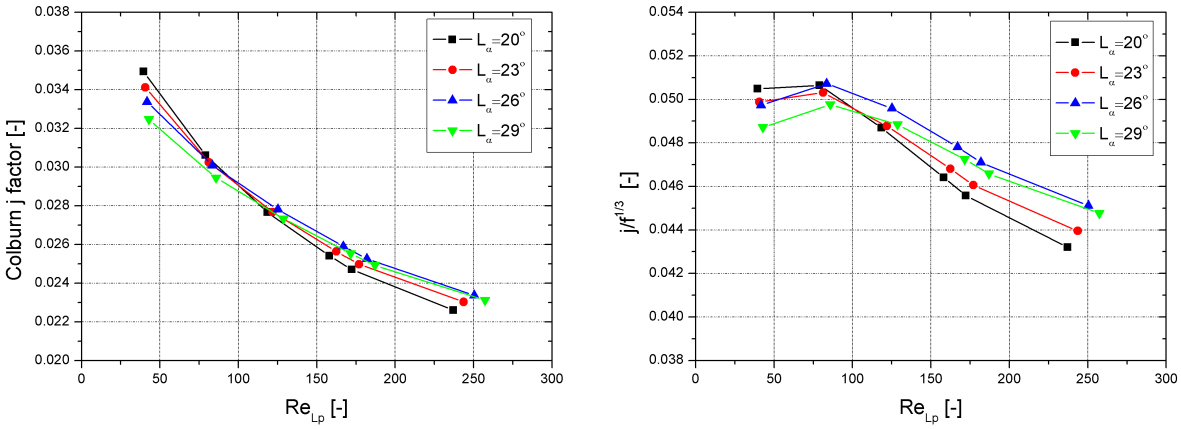

Figure 4.13: Thermal-hydraulic behavior corresponding to louver angle variation at different Reynolds number. **a)** Colburn j factor **b)** Goodness factor.

louvers at relatively low Reynolds numbers ($Re_{L_p} < 200$).

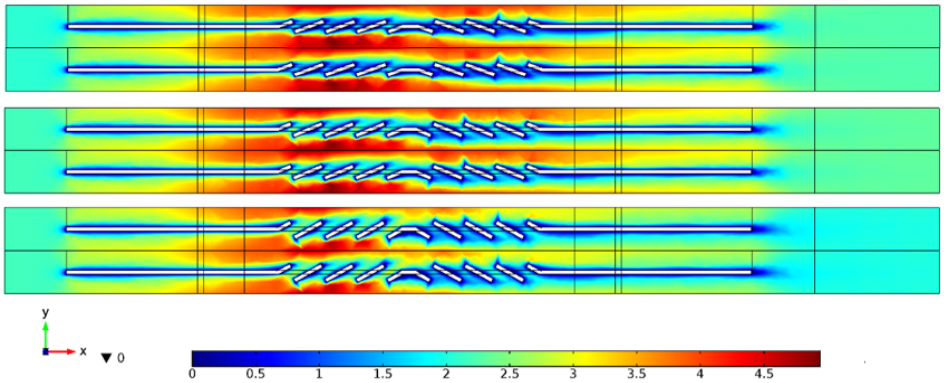

Figure 4.14: Velocity field $[\mathrm{m/s}]$ at plan z=0 for different louver angles $L_\alpha = 20, 26, 29\,\mathrm{deg}$.

The numerical results discussed here show that the air-side heat transfer coefficient is strongly dependent on the relative angle between adjacent fins. Figure 4.13 illustrates the Colburn j factor and the goodness factor in function of Reynolds number. The results shows that the heat transfer is enhanced by increasing the louver angle up to a certain value, $\alpha = 26°$, after which the Colburn factor starts to decrease. This trend can be explained by the louver alignment, which prohibits or delays the re-initialization of boundary layer, as shown in figure 4.14. Whenever the louvers are oriented in a manner that the upstream louvers reduce the effective surface area of downstream louvers available for heat transfer, the heat transfer coefficient is drastically reduced.

Louver length L_l

The larger is the L_l the better will be the heat transfer performance, not only due to the finned surface area increment, but also due to the increase of re-initialization's boundary layer along span direction. However, after a critical value of $L_l = 4.5\text{mm}$ the span direction distance between the boundary layer and the flat tube surface are reduced deteriorating the flow and heat transfer coefficients. The results also suggest that increasing this parameter results in a small penalty of pressure drop. An optimum Colburn j factor was reached with $L_l = 4.5\text{mm}$. Increasing the L_l just 0.5mm (from $L_l = 4\text{mm}$ to $L_l = 4.5\text{mm}$) corresponds to an improving of heat transfer coefficient and heat flux around 2.17% and 0.64% respectively.

Redirection length S_2 *and Louver number* N_l

So far, all the previous results were obtained for a constant louver number and redirection length, $N_l = 6$ and $S_2 = 0.5\text{mm}$. From here, these parameters will be varied to infer on their impact on the flow field and on the heat transfer processes. The redirection length and louver number's effects on Fanning friction and Colburn factors were studied.

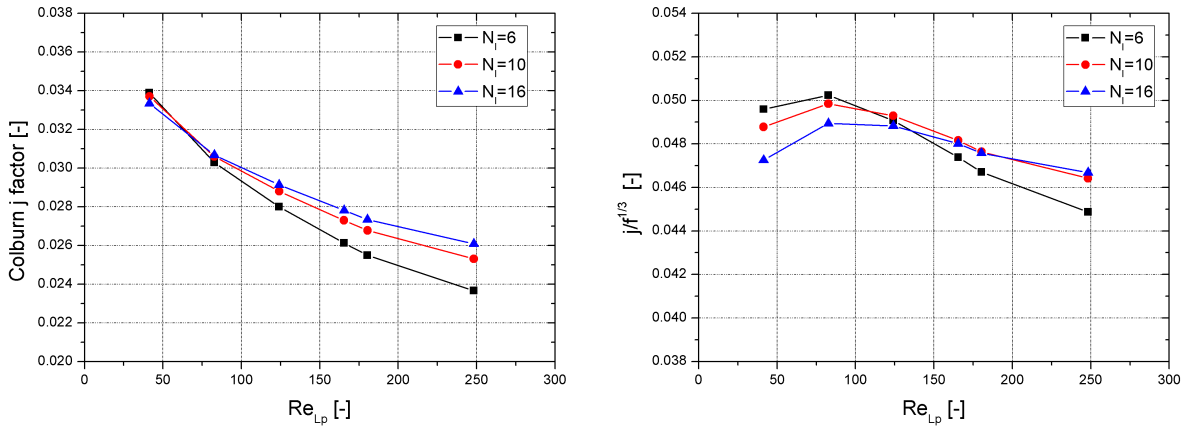

Figure 4.15: Thermal-hydraulic behavior corresponding to louver number variation at different Reynolds number. **a)** Colburn j factor **b)** Goodness factor.

According to these results, regarding the redirection length, one may observe that decreasing the S_2 dimension, up to 0.5mm, increases the Colburn j factor, regardless of the Reynolds number. The friction losses are mostly unaffected by this parameter. Following these results, $S_2 = 0.5\text{mm}$ was taken as optimum value for the final condenser design.

The effect of the louver number on the heat transfer is depicted in figure 4.15. The evaluation of the heat transfer for different louver numbers was performed for the maximum applied Reynolds number $Re_{L_p} = 250$. Increasing the louver number from 6 to 16, provides an enhancement in the Colburn j factor of 7%, while the friction factor is increased 17%. The optimum Colburn factor and goodness factor

was reached with 16 louvers which corresponds to a fully louvered fin (i.e., fin depth is completely filled with louver fins).

The hypothesis of including more redirection louvers in the louver array of the fin was also considered, following the recommendations of Kim et al. [89]. However the numerical results obtained for this scenario did not show any improvement on the heat transfer processes or in reducing the pressures losses, which can be related to the low Reynolds numbers used in this study.

Final Optimized Geometry

The current air-side study suggests that all the studied parameters have impact on the heat transfer and on the fluid flow mechanisms. For example increasing the angle between 20 to 26 degrees the h enhances 10$\%$ corresponding to an increase in the heat flux up to 4$\%$ with low pressure drop penalization. However, if all these corrections are taken into account, a good heat transfer improvement is achieved. The ”optimized” parameters that are recommended to design the final condenser, following the work reported in this chapter, are summarized in table 4.4.

Table 4.4: Optimized fin parameters and illustration.

Parameters		
variable	unit	value
F_d	mm	22
F_l	mm	6.5
F_p	mm	1.38
L_p	mm	1
L_l	mm	4.5
L_α	deg	26
N_l	-	16
S_2	mm	0.5

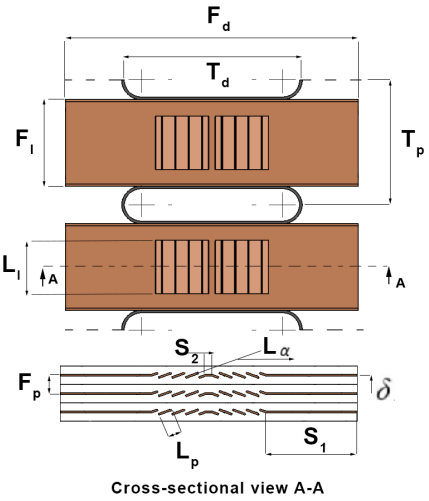

All the quantitative results, summarized in table 4.5 and discussed next, are relative to a corrugated plain fin heat exchanger for the same core's size and evaluated at $3\mathrm{m/s}$ air-flow speed. Numerical results have shown that the final optimized geometry enhances the air-side heat transfer coefficient around 55.0%, which results in approximately 14.8% of heat flux enhancement (although there is an obvious penalty of pressure drop). This results, in turn in a heat rate enhancement factor of 23.4$\%$ against the plain heat exchanger.

However, due to manufacture restrictions, these optimized proposed dimensions were not possible to

be applied in practice. Nevertheless, a local manufacturer - Construção de radiadores Lda, was able to manufacture and work on this type of louver fins after providing us their manufacturing limitations. So, an additional numerical simulation was performed to size and quantify the real gains of the condenser which could be actually manufactured and that was used in the following experimental activity, as detailed in the subsequent chapters. The final core's size of 110x120x22mm was obtained with a Thermal Design Power (TDP) of 250W (the maximum TDP value that is usually defined for modern CPU's). However, in a future work, providing that the current manufacture restrictions can be overcome, the "optimum" geometry values obtained here will allow a reduction in the heat exchanger's transversal area of nearly 12$\%$ for the same TDP of 250W.

Table 4.5: Final thermal-hydraulic enhancement results compared with plain heat exchanger.

	Enhancement at maximum air-flow rate					
Model	$h(\%)$	$\Delta T(\%)$	$q''(\%)$	Contact area$(\%)$	$q(\%)$	$j/f^{1/3}(\%)$
Manufacture	+22.8	-12.2	+7.8	+3.1	+11.1	+8.8
"Optimized"	+55.0	-26.0	+14.8	+7.5	+23.4	+18.9

5. Experimental Methodology

The cooling system must be developed and tested under well defined and controlled working conditions, which are representative of the real TDP and of the actual heat loads dissipated by a real CPU, both at steady-state and transient regimes. Hence, the condensers manufactured by Construção de radiadores Lda, following the analysis described in the previous chapter were used to re-assemble a closed loop thermosyphon facility, as early developed by Moura [28] and later improved by Abreu [33]. This chapter briefly describes the experimental facility that was assembled in this study to test and evaluate the performance of the devised condensers, including also the instrumentation and acquisition system. The experimental procedure and the measurement uncertainties are also described in this chapter.

5.1 Experimental Facility

The schematic diagram of the experimental facility is shown in figure 5.1. It consists of an evaporator and an air-cooled condenser, assembled in a thermosyphon system, aided by a 12V fan, a heater, two power supply modules, a graduated syringe for the working fluid filling, an exhaust valve with a recovery system to prevent fluid leakages and an acquisition system.

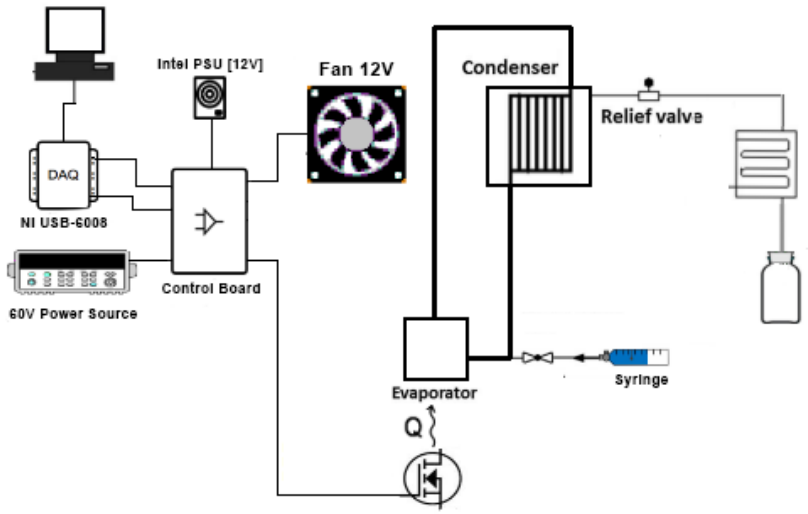

Figure 5.1: Schematic diagram of the experimental setup.

The evaporator is an acrylic tube with 32mm inner diameter, 40mm height and 4mm thick (details on the evaporator were previously described in chapter 4). The evaporator section is electrically heated by

a (IRFP450) transistor with a contact area of 300mm^2 which is connected to a 60V power source and controlled by the CPU and an electric board (described on the next sub-section). This heating element is insulated by a teflon base. The condenser is assembled above the evaporator and mounted on a pivot joint with locking clamping lever support that enables to set the desirable inclination angle θ. As already defined in sub-section 2.3, the condenser's inclination angles are measured from the horizontal plane, where 0° corresponds to the horizontal position, positive values to upward and negative angles to downward flow. This support is composed by two flat smooth surfaces made to settle on each of the condenser's face, which are fitted by two bolts tightened by nuts. Insulation paper is placed on these faces to minimize thermal conduction losses as well as to absorb excessive applied mechanical loads, avoiding damaging the condenser. Following the design and analysis detailed in the previous chapter, two condensers with multi-louver fin and flat tube were manufactured and experimentally tested. Hence, a standard 120x120mm multi-pass condenser was used in reflux mode and the custom made 110x120mm single-passe condenser was implemented in circulation (closed loop). Both cross-flow heat exchangers are constituted by copper on the fins and brass on the flat tubes.

Figure 5.2 show the facility mounted in the horizontal orientation in both circulation and reflux modes. In the reflux mode, figure 5.2(b), two 9mm pipes are used to connect the evaporator to the condenser, in an attempt of enhancing the reflux condensation rate. In the circulation mode, figure 5.2(a), the vapor and liquid phases flow separately, being needed only one pipe for the vapor line and other for the liquid line returning.

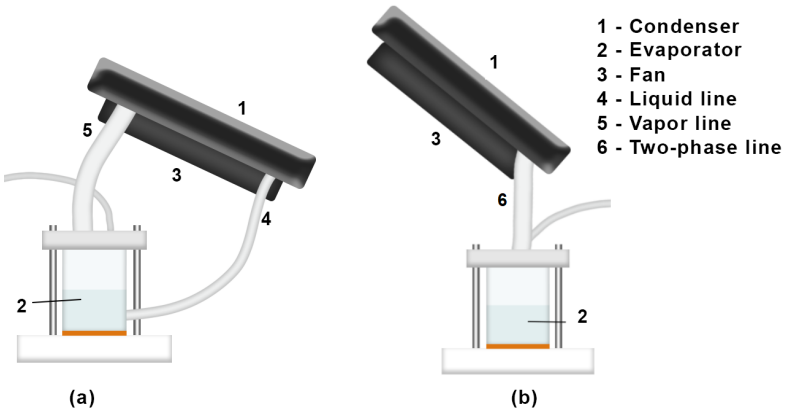

Figure 5.2: System configuration for different condenser [Horizontal]. **a)** Condenser in circulation mode (CLTPT) **b)** Condenser in reflux mode (CTPT).

The same facility, only with condenser in circulation mode, was placed at the vertical orientation, to characterize the behaviour of the CLTPT. However, some strictly necessary changes in the configuration were required. So, a RS pro pneumatic Y threaded-to-tube adapter G1/4 was mounted at the evaporator outlet to allow the vapour passage simultaneously with pressure measuring. This causes pressure losses that affects negatively the system performance, but which is mandatory to assemble the system in

a functional manner. Due to geometric constrains, the setup at the vertical position is more compact, so the difference in height between the evaporator and the condenser is smaller for the vertical orientation. This may affect the heat transfer and the flow mechanisms during boiling and condensation. However, these minor changes and their possible impact on the results were carefully analyzed and taken into account as much as possible when presenting and discussing the results (as detailed in chapter 6).

5.1.1 Instrumentation and Acquisition

Six K-type thermocouples manufactured by OMEGA were used to measure the following temperatures:

1. the junction temperature inside the transistor;
2. the saturation temperature of the liquid in the evaporator;
3. the liquid temperature of the condenser's outlet (only in circulation mode), two-phase temperature (reflux mode);
4. the ambient air temperature downstream to the condenser's fan forced convection air-flow;
5. the ambient air temperature upstream to the condenser's fan forced convection air-flow.

These sensors were placed as illustrated in figures 5.3(a) and 5.3(b) for the circulation and reflux modes respectively, where the numbers corresponds to the previously mentioned locations.

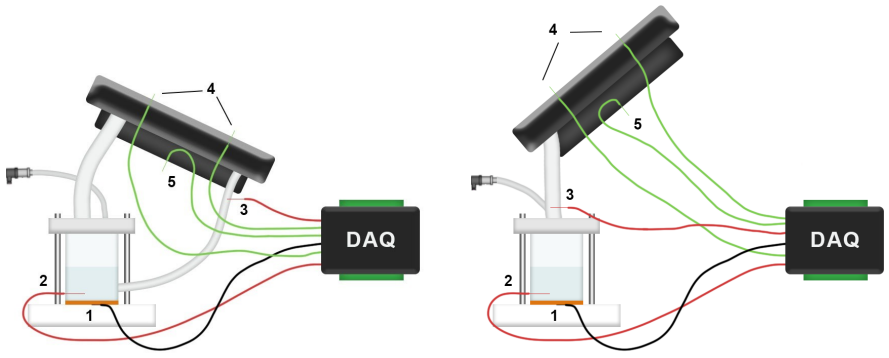

(a) Condenser in circulation mode. **(b)** Condenser in reflux mode.

Figure 5.3: Sensors location for different configurations [Horizontal]. red - coolant temperature; black - junction temperature; green - air-flow temperatures.

Two thermocouples were used to measure the ambient air temperature downstream to the condenser's fan forced convection air-flow, to obtain a more representative value of the average air-flow temperature at the outlet of the condenser. Insulated junction probes were used to measure the junction

temperature inside the transistor and the saturation temperature on the liquid in the evaporator, while the remaining temperature measurements were performed using exposed junction probes. The thermocouples have an accuracy of $\pm 1^{o}$C, being their signal acquired with a Data Translation DT9828E 12-bit ADC cold-junction compensated.

A Gefran -1 to 2 bar pressure transmitter with $\pm$ 0.5% FSO accuracy was assembled on the top of the evaporator and its signal was amplified with a power source regulated to 30V, as stated by the sensor's requirements. The pressure readings were converted to digital by a National Instruments DAQ board, connected to the computer through a USB cable.

5.1.2 Control Board

For a systematic conduction of the experiments and relevant data's collection, a control system was conceived (LabVIEW + NI DAQ + Control board - already shown in figure 5.1). The 12-bit National Instruments USB-6008 DAQ board with 1.0kHz converts the signals from analog to digital (or the opposite) which are needed to be controlled, in order to perform an automatic system's control. Only two quantities are being controlled: the electric power dissipation (heat load) and the inner evaporator pressure.

The electrical power input to the heater was controlled using an electric board monitored in a LabVIEW algorithm, by measuring the applied voltage and current. With the current and potential difference it is possible to calculate the real Joule power, which corresponds to the desired heat load rate to be imposed. The electric circuit receives the analog signal from the NI DAQ board and feeds the transistor MOSFET with 60V. The electronic circuit responsible for the heat load control, originally designed by Abreu [33], was improved in the present study with new Op-Amp, power film resistors and MOSFET, to allow reaching higher power dissipation and junction temperatures. The power control circuit scheme is provided in Annexes A.1. More detailed information on the signal processing can be found in Abreu [33].

On the other hand, the pressure in the evaporator can be controlled with the fan's RPM, according to the purpose of study (later discussed). The user can set the speed of the fan or make it vary, using a PID control to maintain the required pressure. A LabVIEW code backed by an electric circuit allows to control the output voltage and then the fan's RPM. The linear controller just amplifies the NI output [0-5V] to [0-12V]. The electric circuit used is shown in Annexes A.2.

It is worth mentioning that, for safety reasons, the transistor maximum operating temperature (150°C) is much higher than the normal working temperatures of a real microprocessor. However, throughout this work, when the junction temperature surpass forbidden temperature values for a real CPU, i.e. above from 80°C, the system is turned off.

5.2 Experimental Method

The experimental method described here includes the procedure followed in the closed system assembly, namely surface removing, surface cleaning and the new surface assembly. The degassing procedure is described next, being followed by the experimental procedure used to perform the experiments to characterize the performance of the condenser and of the entire cooling system both at steady and transient regimes.

5.2.1 System Assembly - Boiling Surface

Following previous work from Moura [28] and from Abreu [33], which clealry evidenced enhanced heat transfer coefficients and superior overall cooling performance of the thermosyphon system, using microstructured surfaces, the surfaces leading to the best results reported in [33] were also tested here, to infer on their impact with the custom made condenser. The surfaces were microstructured with a regular pattern of cavities with fixed diameter of 100μm and depth of 15μm . The distance between the microcavities S[μm] was varied, so that experiments were performed for $S = 100\mu$m, $S = 200\mu$m and $S = 600\mu$m. A smooth surface was also used as a reference. The surfaces, already used by [33] were fully characterized in terms of topography and wettability, quantified by the contact angles. The detailed characterization of the surface properties and measurement procedures is reported by [33]. HFE-7000 is a well wetting liquid, so that the contact angles measured with this liquid are always close to zero. The set of experiments using the microstructured surfaces was performed under steady-state conditions.

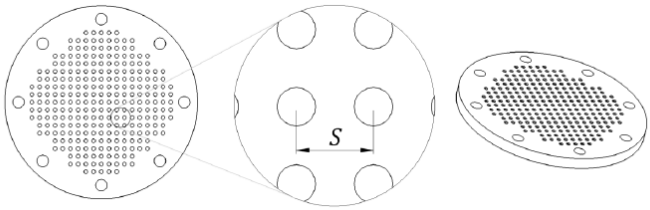

Figure 5.4: Microstructured copper surfaces and microcavities distance S.

Before being mounted in the evaporator the surfaces must be carefully cleaned with an acetone bath. A thermal compound was then applied on the transistor bottom's face, to reduce the thermal resistance between the transistor and the surface. Approximately the same amount of compound was used with each surface to assure repeatability of the results. The surface was manually placed at the center of the teflon base together with the acrylic evaporator with two O-rings on each extremity. The set acrylic evaporator and copper surface has to be visually centered in the assembly and then closed with the top acrylic cover which compresses and closes the evaporator by screwing the four studs. Afterwards, the transistor must be reassembled under the surface, through the teflon base's cavity. Four springs were

placed to assure a constant contact pressure along the junction surface. Finally, the system was be filled with an surplus amount of liquid, taking into account some losses that are inevitable in the degassing process that will be detailed next.

5.2.2 Degasification of the Working Fluid

At the beginning of each test, after filling the evaporator with HFE-7000, a degasification procedure is followed to remove as much as possible the dissolved air which affects the results, namely the onset of boiling. The first step of this procedure consists of simply moving around and shake the evaporator to help any enclosed air bubble or bag to move out of the evaporator, moving to upper zones, facilitating the degassing. After visualizing the liquid height without any air bubble the condenser exhaust valve was closed, closing the loop, and the controlling circuit is set to an initial power dissipation of $5\mathrm{W}$. The saturation temperature slightly increases as well as the inner pressure and the working liquid is on the natural convection regime. After the steady state is achieved, the heat load was increased to $20\mathrm{W}$. At this stage, active nucleation sites are already observed. Small heat load steps were then slowly applied until the evaporator pressure overtook $1200\mathrm{mbar}$ (corresponding nearly to an imposed heat load of $50\mathrm{W}$). At this stage, the exhaust valve was opened and closed repeatedly and very quickly, just 1 second each time, allowing the vapour and non-condensable gases to escape. This procedure leads the system pressure to rapidly decrease, so care should be taken to keep the pressure in the evaporator monitored and controlled. The exhaust valve was then closed when the pressure was close from the atmospheric. At this point, the liquid saturation temperature was checked and used to calculate the pressure, according to equation 4.1. The obtained value was compared with the pressure value measured at the evaporator. All the process is cyclically repeated until the pressure inside the evaporator is as close as possible to the pressure curve provided by the manufacturer of the working fluid. The degasing process was considered to be completed when the pressure value measured in the evaporator difered from that calculated by less than $50\mathrm{mbar}$. After degasification is completed, the liquid level should be re-checked and adjusted, if required.

5.2.3 Experimental Procedure Overview

With the degassing already performed, the facility is ready to be used, either in (1) steady or (2) transient regimes. The respective LabVIEW routine and QuickDAQ routines are started to monitor the temperatures and pressure at 20Hz, checking the operability of the sensors. Next the power supply should be turn on and the voltage must be set to 60V, because the analogic circuit together with LabVIEW code were projected to work at this voltage. Then depending of the state:

1. All the steady-state analysis (horizontal and vertical) were performed under controlled pressure

working conditions, via a PID controller implemented on LabVIEW. The evaporation pressure and consequently the boiling saturation temperature are controlled by the condenser fan rotational speed. So in the steady-state case, the user should set in the LabVIEW routine the reference pressure (1005mbar) to control the evaporator pressure. The operability of the control system must be ensured, by checking if the read heat rate corresponds to the input heat load.

5W steps were successively imposed until the onset of boiling was detected. Afterwards, the power steps were increased to 20W, until CHF was achieved or dry-out occured or the junction temperature exceeded the 80°C. Note that the critical heat flux depends on many parameters such as the surface orientation and topography. Relevant temperature and pressure values were collected only when steady-state was achieved and temperatures and pressure values were stabilized (this may take up to 10min). Each experiment performed for a different imposed heat load (steady-state regime) was repeated five times, for increasing and decreasing heat flux.The obtained data was then used to compute mean values and standard deviations for the each imposed heat load allowing to obtain a complete curve.

2. The transient-state analysis were performed under real working conditions (i.e. without controlling the pressure), with the fan set to run at constant speed. So the user should set in the LabVIEW routine the manual RPM control and aided by a manual anemometer with accuracy of $\pm 5\%$ read the air-flow speed in order to reach the air velocity of 3$\mathrm{m/s}$, to match the air-flow speed which was considered in the previous chapter, when the condenser was dimensioned and designed. A real scenario with transient power loads was implemented in LabVIEW, being the temporal evolution of a number of quantities monitored, following a custom made training benchmark adapted from Isci and Martonosi [90].

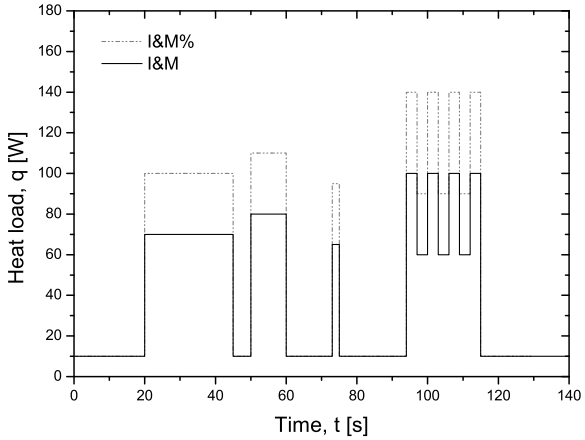

Figure 5.5: Power loads adapted from Isci and Martonosi benchmark. [90].

Hence, the applied cyclic heat load profiles shown in figure 5.5, named here as I&M power input and I&M% power input, respectively, being the later with heat loads approximately 40% higher were used to evaluate the reliability of the cooler system. Temperature and pressure values are monitored for 140 seconds, being each test repeated three times.

The experimental procedure detailed above is performed for both tested condensers, in reflux and circulation modes.

5.3 Measurement Uncertainties

The main quantities which are measured within a certain uncertainty in the present work are pressure, temperature and the heat load. The pressure and temperature measure uncertainties are given by the transducer uncertainty, which is added to the analog to digital signal converter uncertainty. In the heat load control, the uncertainty is due to the voltage readings from the power source to the DA converter and from the AD to the the power control circuit. The uncertainties are summarized in Table 5.1.

Table 5.1: Uncertainty data for featured instruments.

	Pressure		**Temperature**		**Heat load**	
	Transmitter	DAQ	Thermocouple	DAQ	AI*	AO*
U	0.5%	7.73mV	±1K	±0.1K	7.73mV	7mV

* AI - Analog input; AO - Analog output.

The uncertainty in the temperature measurements is assessed according to Abernethy et al. [91]. The heat load uncertainty is not represented in the plots for the sake of readability and ease of understanding. For instance, in the boiling curves, the wall superheat error is estimated according to:

$$Error_{\Delta T_e} = \sqrt{2U^2 + (2\sigma_{Tj})^2 + (2\sigma_{Tsat})^2} \tag{5.1}$$

6. Results and Discussion

The current chapter presents the results obtained through different experimental working conditions and equipment as well as a discussion on these data. First, in sub-chapter 6.1, the experimental working conditions were carefully detailed in steady-state. Next, in sections 6.2 and 6.3, after results validation, an extensive analysis is performed on horizontal, vertical surface orientation and also on the performance of the condenser. A comparison between the two devised facilities (horizontally and vertically oriented systems) were performed in booth studies (steady and transient).

Following this analysis, conclusions are drawn taking into account the cooler optimization and future implementation in real desktop CPU.

6.1 Working Conditions

This first sub-chapter intends to characterize the steady-state working conditions from the temperature distribution along the loop, governing pressure and also start-up behavior of the two-phase closed loop thermosyphon. For this purpose, the results presented and discussed in the next paragraphs were obtained using the following configuration:

- smooth non-structured copper surface;
- Evaporator with 32mm inner diameter and 40mm height;
- 30ml HFE-7000 fill charge;
- single-pass condenser in circulation mode with tilt angle of 30º (downward).

This configuration was carefully chosen, taking into account the setup and proof-of-concept prototype previously devised by Moura [28]. The condenser was positioned with a -30º tilt angle in order to enhance hydraulic drainage of the liquid film condensed, as suggested by Lip and Meyer [44, 45] (more information in 2.3). A Cooler Master JetFlo 120 fan was coupled to the condenser promoting the forced air-flow convection. Point out that the facility was designed and assembled as described in the previous chapter 5.

The initial governing pressure is set as the saturation pressure at ambient temperature, which was typically around 22$\pm$1ºC. The measured pressure could never match exactly the vapour pressure value predicted by equation 4.1, even after the degassing process. However measured values were at most 20mbar higher than the predicted one, resulting in a maximum increase of liquid saturation temperature

of $0.8^{\circ}\mathrm{C}$, which is considered acceptable, as it is within the uncertainty range of the measurements. With the increase of the heat load, the vaporization mass flow rate tends to increase, being unbalanced by the mass flow rate that is condensed. A way to improve condensation is therefore required to avoid this unbalancing, the system search for a way to improve the condensation. There are two alternatives, namely by spontaneously increasing the governing pressure within the closed loop - Real Working Conditions (RWC) - or forcing the raising of condensation rate by increasing fan RPMs - Controlled Working Conditions (CWC).

It is worth noting that along this work, the CWC was exclusively used for steady-state analysis. This condition was implemented for scientific purposes, in order to compare the experimental data obtained here with those reported in the literature, which are mostly obtained under controlled pressure conditions. The RWC was implemented only for transient-state analysis due to the implemented controller's insufficient response time to control the inner system pressure in a real CPU heat load demand. Thus, in transient analysis, the experiments were performed under RWC, simulating as much as possible what would occur if it were implemented in a real CPU.

6.1.1 Real Working Conditions - RWC

Under these conditions, the fan is set to run at constant speed, more precisely at $3\mathrm{m/s}$ air-flow speed independently of the heat rate. Increasing the heat load, the vaporization rate tends to be higher than the condensate rate, unbalancing the mass flow rate in the evaporator and consequently increasing the saturation temperature.

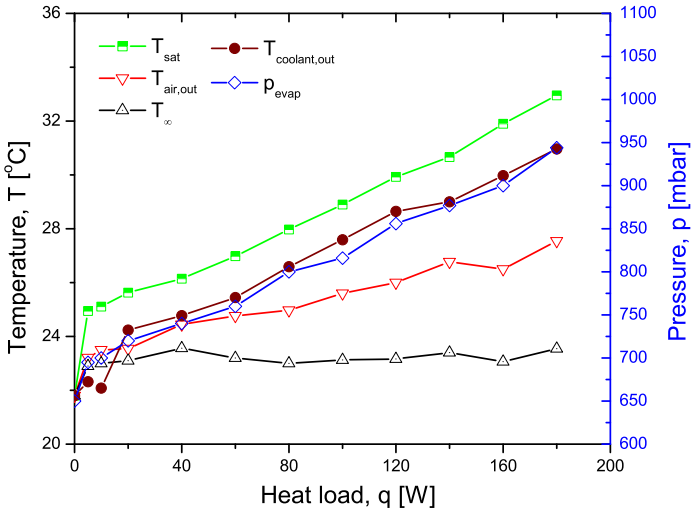

Figure 6.1: Steady-state temperature and pressure measurements along the loop at real working conditions.

It is important to note that, with higher working pressures, the condensation HTC tends to be slightly

enhanced. For this reason, a new equilibrium state with higher governing pressure within the closed loop is reached. Therefore, for the same ambient temperature and constant fan velocity, the liquid saturation temperature increases with increasing heat load, as well as all the temperatures measured along the loop. This trend is clearly observed in figure 6.1. One should stress the pressure-temperature direct relation that is evident between the saturation temperature and working pressure, as represented by the green and blue lines respectively, which confirms the saturation curve provided by the manufacturer, equation 4.1.

6.1.2 Controlled Working Conditions - CWC

At controlled pressure conditions, the fan speed depends on the input heat load. A PID controller was implemented in LabVIEW, to keep the evaporator inner pressure as constant as possible. Under these working conditions, the initial pressure set-point was carefully chosen taking into account several considerations. In fact, low pressure values lead to lower saturation temperature, which negatively affects the system for higher heat loads, causing an excessive presence of vapour phase in the evaporator and reducing the CHF value. The opposite effect occurs at higher pressure values. Hence, taking into account the demanding heat load range and in order to avoid the CHF, the pressure set-point was 1005mbar, very close to atmospheric pressure as proposed by Abreu [33]. Figure 6.2, shows the loop temperatures

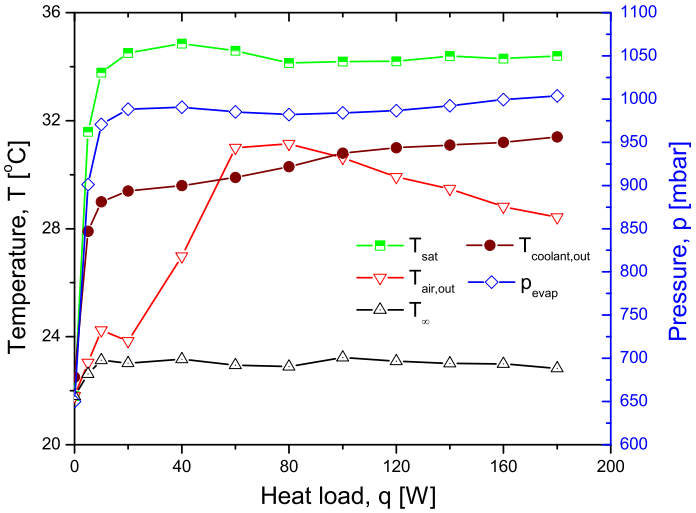

Figure 6.2: Steady-state temperature and pressure measurements along the loop at controlled conditions.

and governing pressure, as a function of heat load input for this specific working conditions. The plot shows that the pressure was reasonably maintained constant above 20W, as observed by the trend of the T_{sat} green line. Within this range, the inner pressure was maintained within a maximum deviation

of 15mbar from the set-point and the corresponding saturation temperature was kept at 34.2°C with a standard deviation of 0.3°C.

6.1.3 Thermodynamic Loop Characterization

It is important to understand the system's thermodynamic cycle along the closed loop, in order to improve its efficiency. However due to an insufficient number of sensors required to acquire pressure and temperature data along the loop, the thermodynamic cycle is mostly analyzed qualitatively. Therefore, the following images represent the p-h phase diagram of the working fluid HFE-7000 in order to understand better its behavior along the closed loop. Note that, the saturation temperature and the isentropic lines are additionally illustrated in figure 6.3.

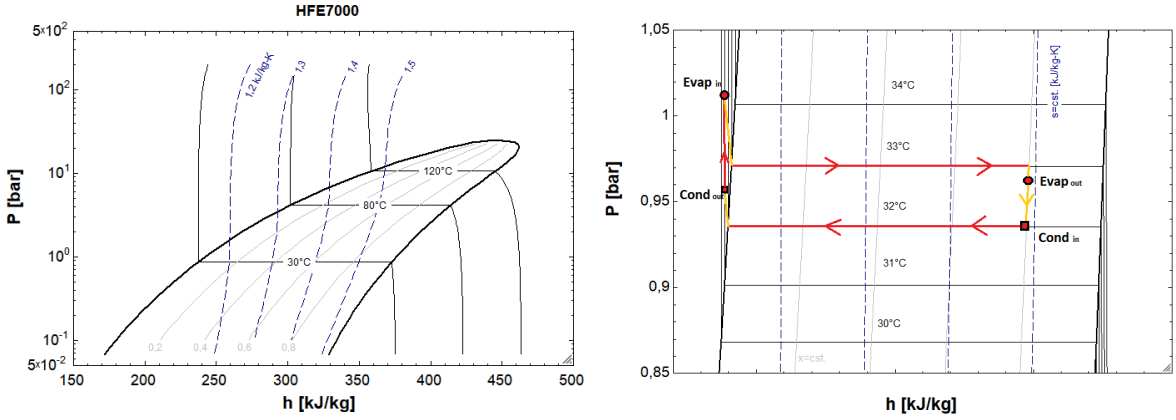

a) b)

Figure 6.3: Thermodynamic phase diagram (p-h) for HFE-7000. **a)** Overall p-h diagram. **b)** Refrigerant loop under real working conditions at 170W.

The diagram shown in figure 6.3, presents the predicted detailed evolution of the two-phase thermosyphon closed loop at the maximum imposed heat load (170W), using the smooth surface on the evaporator. Here, the circles correspond to data points at the evaporator and the squares are associated to the condenser. The top horizontal red line, represents the saturation temperature in the evaporator, while the under horizontal red line expresses the saturation temperature in the condenser. At the evaporator outlet, the vapour quality is assumed to be lower than 1 due to the visible presence of vapour-liquid mixture arising from the pool boiling evaporator. Furthermore, temperature and pressure values at the evaporator outlet are lightly lower than the saturated one, due to the sudden contraction, 7:2 area-ratio, from the evaporator to the exit channel. This contraction causes a pressure drop, generating an expansion process with a sensible temperature drop. Between the evaporator outlet and the condenser inlet, pressure and temperature drops are predicted to occur due to friction and thermal losses along the connection pipe, influenced by the pipe curvature. In the condenser, the fluid tends to be gradually condensed at constant pressure, until reaching the liquid saturated line. This is caused by the geometry

of the gravity assisted condenser, in which stratified flow with thin liquid film falling attached to the bottom wall of the tubes is drained due to the hydraulic gradient imposed. In the stratified regime, pressure losses are negligible owing to the quiescent vapour condition assumed inside the condenser. When the fluid reaches the sub-cooled region, the pressure tends to slightly increase due to the ascending fluid head along the tilted condenser. Note that the position of the condenser outlet point is influenced by the condenser's inclination since it influences the flow regime, the heat exchange and also the pressure head. In practice, it is also expected that the condenser outlet presents lower temperature than the values read at the inlet, which means that some sensible heat was removed from the system to the ambient by the heat exchanger. In summary, at the condenser outlet a sub-cooled state is presented with $T_{cond_{out}} < T_{cond_{in}}$, $p_{cond_{out}} > p_{cond_{in}}$. Downstream of the condenser, the gravitational-type pressure head impels the coolant into the evaporator inlet, reaching the maximum pressure at the evaporator inlet point. The presented results are in reasonable agreement with other studies reported by Chang et al. [92] and Zhang et al. [93].

To complete the general overview of the thermodynamic properties characterization along the loop and as function of heat load, the liquid level inside the evaporator is also worth to mention. The mass flow rate increases with increasing power. Friction losses consequently increase, which results in a corresponding liquid height decrease in the evaporator. This trend in the liquid level ratio with the heat loads is obvious and must be taken into account for an adequate design process, to avoid surface dry-out at high power loads. For example, at the same heat flux, under higher governing pressures, the boiling temperature increases, so the liquid level will reduce less.

6.2 Experimental Facility Under Controlled Working Conditions - Steady-State

The current section covers the outcomes of the steady-state study performed on the experimental facility (horizontal and vertical oriented) under CWC as described before in 6.1.2. The results discussed in this sub-section were obtained under controlled saturation temperature values. Under these conditions the results are independent from ambient temperature fluctuations and the comparative study performed at the condenser, evaporator and at the overall system efficiency are more conclusive. Limiting operational boundaries are defined according to their CHF and the thermal performance is characterized based on HTC, as well as on the absolute thermal resistance. In the final sub-chapter, a heat transfer analysis is performed on the condenser, focusing on the overall cooling system improvement, evaluated by the heat exchanger's effectiveness, ε. In order to perform an accurate and equitable experimental study, the evaporator pressure was kept constant throughout experiments, despite the challenges to overcome the control of pressure.

6.2.1 Horizontal Surface Orientation Setup

In the horizontal surface orientation setup, an experimental validation was firstly performed, keeping the same facility configuration as detailed in the previous chapter, in order to proof the functionality and repeatability of the devised thermosyphon system. Such analysis provided sufficient experimental results to validate the experimental setup and methodology based on the comparison with relevant results reported in the literature, obtained under comparable conditions. After this validation, a systematic characterization was performed to evaluate the cooling behaviour of the devised system, mostly related with the design and configuration of the condenser. This analysis includes changing the microstructured surface which is mounted on the evaporator, as it is known, from previous studies, to strongly affect the overall performance of the system. Hence, the performance of the designed condenser was analyzed including this major influence. Finally, the thermal resistance of the overall system is evaluated, to derive conclusions on the performance of the condenser, based on a quantity that is commonly used in studies addressing electronics cooling.

Validation of Pool Boiling Setup

The results obtained in the present study, with the initial configuration presented in section 6.1, were compared to those obtained by [28] and [33], under similar working conditions, for validation purposes. It is worth mentioning that all the plots named as pool boiling curves shouldn't be fully addressed with the real term of boiling curve because the superheat was taken using the junction temperature, which is more representative in this specific study than the surface temperature. Similar procedure was followed by [28] and [33]. Moreover, the pressure was not strictly constant as defined by Nukiyama [52].

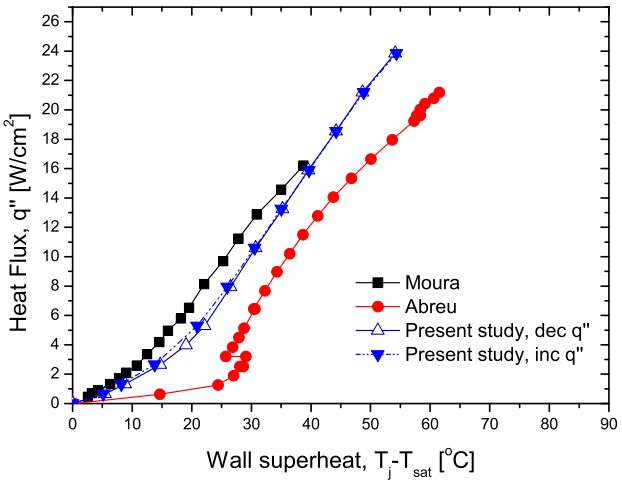

Figure 6.4: Proof of concept - experimental results validation for smooth surface [Horizontal].

The pool boiling curves represented by triangle blue lines in figure 6.4, were obtained increasing and decreasing the heat flux, to observe the possible occurrence of hysteresis. The plot shows a minimum discrepancy due to the hysteresis phenomenon, which is associated to the activation of the nucleation sites. All the subsequent boiling curves will be obtained solely by decreasing the heat flux. The results show that the heat flux curves follow the trend of a typical boiling curve. The aforementioned results are also in good agreement with those reported in [28] (square black line in figure 6.4) and in [33] (circles with red line), even though the working conditions could not be all exactly matched. Hence, different boiling regimes can be distinguished in the figure, namely natural convection followed by nucleate pool boiling. Around the 55°C superheat, 24 $\mathrm{W/cm^2}$ heat flux region, a CHF condition was attained and the system was shut down to avoid burnout.

Effect of Micro-structuring the Surface in the Evaporator

As aforementioned, the effect of micro-structuring the surface is addressed in the present study, being discussed in this sub-section. The results are always discussed with the scope of improving the cooler performance, namely focusing on the possible effect/relation of the various parameters with the performance of the condenser. The methodology adopted in this set of experiments consists on starting every experiment at maximum power, thus maximizing nucleation sites activation and decrease step by step the imposed heat power, until turning off the power source.

The boiling curves obtained on the horizontal setup, for different microstructured surfaces are depicted in figure 6.5. Each curve is averaged from 5 data sets, for each surface, being the uncertainty calculated as previously described, in chapter 5.3.

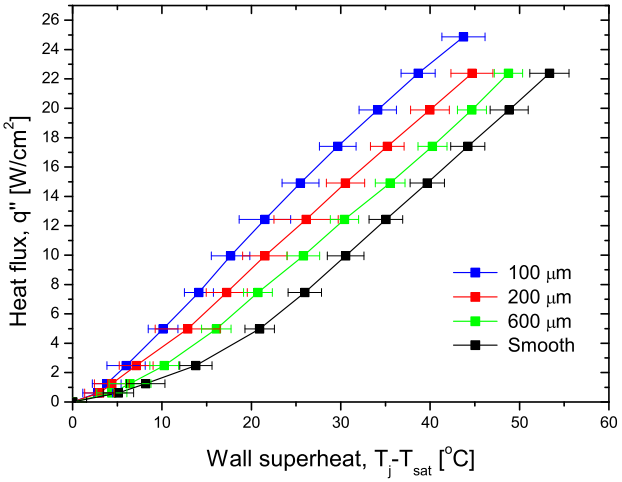

Figure 6.5: Boiling Curves under controlled conditions [Horizontal].

The boiling curves depicted in this figure show an obvious heat transfer improvement as the cavity

distance, S is reduced: the lowest cavity distance of 100μm leads to the lowest superheat temperature value, for the same imposed heat flux. Also, for this enhanced surface, it was possible to scope higher heat flux values without reaching the CHF.

The heat transfer coefficient ratio, in figure 6.6, shows the HTC relative to a smooth surface, for different microstructured surfaces. These values were plotted as a function of the imposed heat flux load, a common procedure followed in studies reported in the literature, e.g. [29]. Here, the error bars are the experimental standard deviation of consecutive measurements. From the figure one can infer a general trend depending on the boiling regime. Hence, as the imposed heat flux load is increased, within the regimes of natural convection and nucleate boiling with isolated bubbles regimes, the heat transfer coefficient ratio tends to increase. On the other hand, in the the nucleate boiling in the jets and columns regime, the HTC is reduced for increasing of heat fluxes, as interaction phenomena tend to promote the formation of vapour blankets and endorse the occurrence of the CHF.

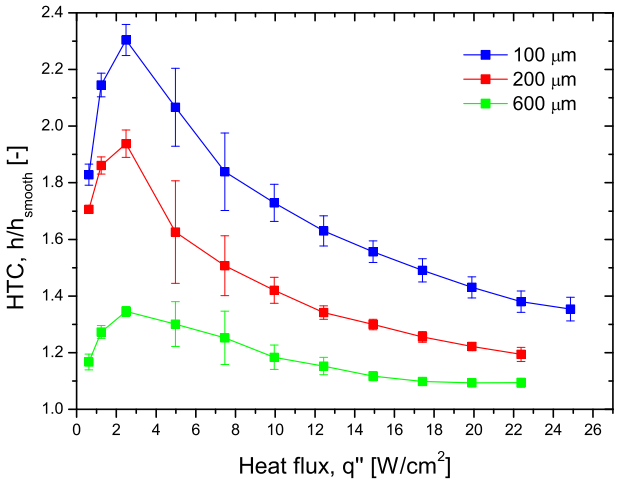

Figure 6.6: HTC ratio under controlled conditions [Horizontal]. Error bars indicate the average standard deviation.

Following this analysis, the experimental data acquired under controlled pressure was used to determine the average boiling heat transfer coefficient for the microstructured surfaces, h_{av}. The relative increment in the heat transfer coefficient compared to that obtained with the smooth surface, h_{smooth}, was plotted in figure 6.7. The HTC ratio values plotted as a function of the distance between cavities, S, were also compared with the data obtained by Moura [28] and by Moita et al. [29, 31], whose studies were performed for the same working fluid. However, between these studies, several experimental conditions were different, namely the surface material, the working pressure and also the depth, shape and size of cavities. Even so, a qualitative comparison concerning the effect of cavity distance in the relative enhancement of pool HTC versus cavity distance is illustrated in figure 6.7.

The present data set follows the same trend as those of Moura [28] and of Moita et al. [29, 31],

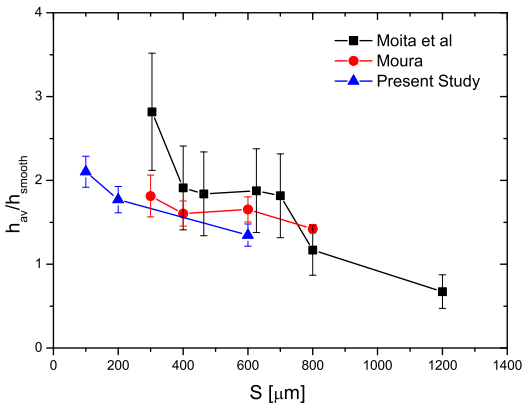

Figure 6.7: Average HTC ratio along cavity distance under controlled conditions. Error bars indicate the average standard deviation.

thus qualitatively confirming the role of the distance between cavities in the enhancement of boiling heat transfer. Disparities between the present study and the other results should be associated to the different experimental conditions, as aforementioned. Moreover, one should point out that the condenser is in circulation mode, in the present study, which also affects the boiling performance. The results show a clear HTC enhancement for lower cavity distances. However, care should be taken, as this trend is not monotonic. Moita et al. [31] and Valente et al. [94] studied this topic, proving that shortening the distance between nucleation doesn't imply an HTC enhancement, being even possible to reduce the HTC. Hence, the distance between cavities must be a counterbalance between the positive effect of promoting the activation of nucleation sites with the negative effect of excessive interaction between them (bubbles coalescence). Such effect however, is not present up to the smallest distance between cavities that could be tested in the present study.

Overall Thermal Resistance of the Thermosyphon

The loop thermosyphon's overall thermal resistance (junction-to-ambient), R_{sys}, is the sum of each component thermal resistance, more properly the solid heat conduction, the contact resistance and especially the boiling and condensation equivalent thermal resistances, R_{evap} and R_{cond} respectively. The following figure 6.8 displays the relevant thermal resistance variables in a logarithmic scale, characterizing the thermosyphon loop performance with a smooth surface and optimized microstructured surface (S =100μm), black and blue colours respectively on the graphic.

The overall thermal resistance, circle points on the graphic R_{sys}, decreases significantly with increasing heat power. The lowest R_{sys} values were reached at maximum heat loads, namely 0.361$\mathrm{K/W}$ for the smooth surface and 0.276$\mathrm{K/W}$ for the microstructured surface. As aforementioned, the microstructuring enhances the boiling heat transfer in the evaporator, reducing the evaporator thermal re-

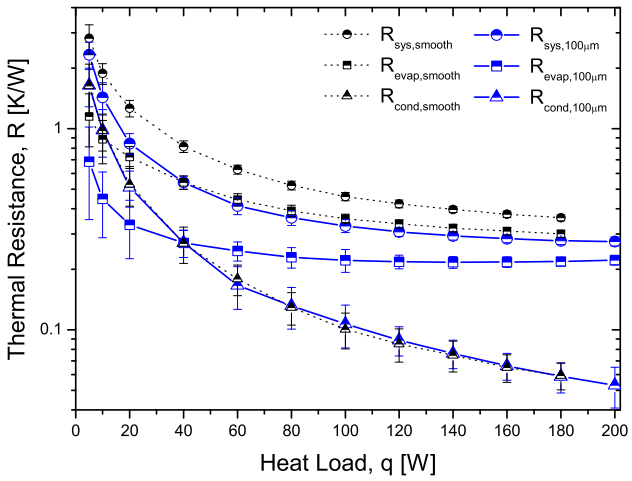

Figure 6.8: Thermosyphon loop's thermal resistances under controlled conditions with different surface topography [Horizontal].

sistance and consequently decreasing the overall resistance. Under maximum heat load demand, the junction temperature is nearly 15°C lower using the microstructured surface with S =100μm, when compared to that obtained using the smooth surface. This temperature difference results in approximately 23% lower overall thermal resistance for the microstructured surface, when compared to that obtained with the smooth surface. This percentage tends to increase for lower heat rates, because the HTC microstructured enhancement is greater for low heat fluxes, where there is no bubbles coalescence. On the other hand, as expected, the condenser thermal resistance (triangle points) was not affected by the micro-structuring effect.

6.2.2 Vertical Surface Orientation Setup

The systematic characterization of the system, performed on the horizontally oriented facility was repeated as the facility was set in the vertical orientation. The exhaustive description of such results is not provided here, so that only the results obtained for the smooth and microstructured surface with S = 100μm are presented here, for comparative purposes. These results were obtained under controlled pressure conditions.

Vertical vs Horizontal: Effect of Micro-structuring the Surfaces in the Evaporator

The adapted boiling curves under controlled conditions, obtained on the vertical setup (smooth and S = 100μm) are compared with those previously discussed, which were obtained for the horizontal orientation. The effect of surface orientation on boiling performance depends on the type of surface

as observed in figure 6.9. For the smooth surface, the data obtained here is in good agreement with

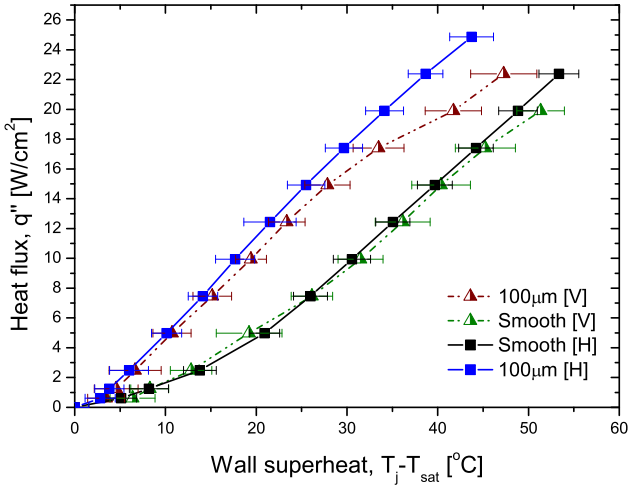

Figure 6.9: Boiling curve for different surface orientations under controlled conditions [Horizontal and Vertical].

the theory referenced in sub-chapter 2.3. Hence, for a certain value of wall superheat, more precisely ΔT lower than 25°C, the vertical setup (green triangles), presents higher heat fluxes when compared with the horizontally oriented setup (black squares data). For low wall superheat values, the vertical surface boiling heat flux is improved because the fluid mixing in the boundary layer, originated by the rising bubbles, promotes the increasing of the HTC. It is worth mentioning that, in this context, the microstructured surface does not lead to enhanced boiling performance when compared with the horizontal setup. This may be due to excessive vapor accumulation near the surface, which is promoted by the micro-structures, being lessened on the smooth surface. So, one can conclude that the impact of the inclination or orientation of the setup on the HTC depends on the characteristics of the surface that is mounted on the evaporator.

It is notorious for both curves that the CHF was reduced for the vertical oriented surface. Beyond that, with the vertical setup implementation, the upper part of the contact surface tends not to be completely covered by the liquid, as the heat flux increases, leading to the reduction of HTC. This phenomenon, in turn is associated to the liquid level ratio reduction which occurs as the heat load increases, as discussed in the previous sub-sections. Thus, a surface dry-out situation is easily reached when the cooling system is at the vertical orientation. This is important to address in the design and mounting of the final system, as most of the CPU's are nowadays mounted and prepared to work in the vertical position.

The overall thermal resistance and the evaporator resistance (represented by circle and square points respectively) depict the same trend whether the system is in the horizontal or in the vertical orientation (figures 6.10), although the overall thermal resistance is lower for lower heat loads and higher for large heat loads when the setup is at the vertical position, due to the vapour accumulation already dis-

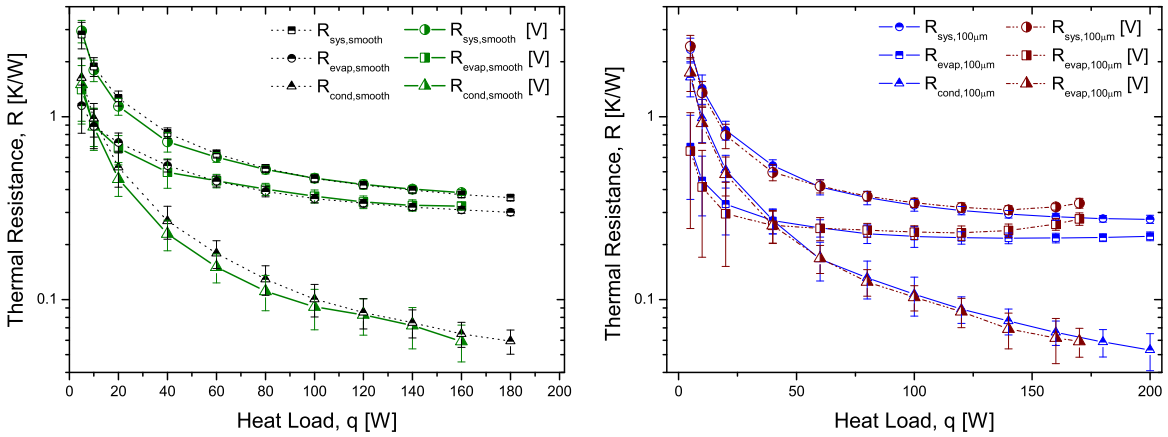

a) smooth surface. **b)** microstructured surface S =100μm.

Figure 6.10: Cooler performance for different surface orientations under controlled conditions [Horizontal and Vertical].

cussed in the previous paragraphs. Based on this analysis, the vertical thermosyphon system devised here with condenser in circulation achieved $R_{sys} = 0.337\mathrm{K/W}$ for the maximum heat load of $170\mathrm{W}$.

On the other hand, the thermal resistance related to the condenser is lower in the vertical orientation, when compared to that evaluated in the horizontal orientation. However, such differences should be attributed to different configuration elements which had to be included to position the cooling system at the different orientations. As mentioned in chapter 5 an Y-shaped adapter was mounted at the evaporator outlet causing pressure losses and consequently small temperature drop that could reduces the condenser absolute thermal resistance for the vertical setup.

6.2.3 Condenser

The condensation is detailed in this subsection where, the main focus is to evaluate the impact of the design condenser in the overall cooling system improvement. The effect of orientation (inclining the condenser at different angles) is firstly addressed, in both co-current and counter-current flow. This analysis is followed by a comparative study between the flow modes and their impact on the cooler system.

The HTC inside tubes, as already introduced in chapter 3, depends mainly on the mass flux and vapour quality. Since it was not possible to determine precisely the mass flux or the vapor quality in the system, the condenser was characterized taking into account the heat load input.

Effect of Condenser Orientation - Tilt Angle

Looking now into the loop condenser, more precisely to the condensation inside tubes, the experimental mean condensation heat transfer coefficient was deduced from the Newton's Law of cooling (equation 3.1). Where the heat flux is calculated from a thermal balance on the air side and divided by the total surface area of the heat exchanger, A_0. The excess of temperature, ΔT_e is referred to the temperature difference between the refrigerant saturation temperatures, T_{sat} and average wall inner temperatures, $\bar{T}_{w,i}$ of the test section determined by $\bar{T}_{w,i} = \bar{T}_{w,o} + |qR_w|$. The saturation temperatures were taken as the average between the measured inlet and outlet refrigerant temperature measurements in the condenser.

Several correlations, as shown in sub-chapter 3.2.3 were used to validate the experimental data. The experimental results are therefore confronted with the correlation in figure 6.11.

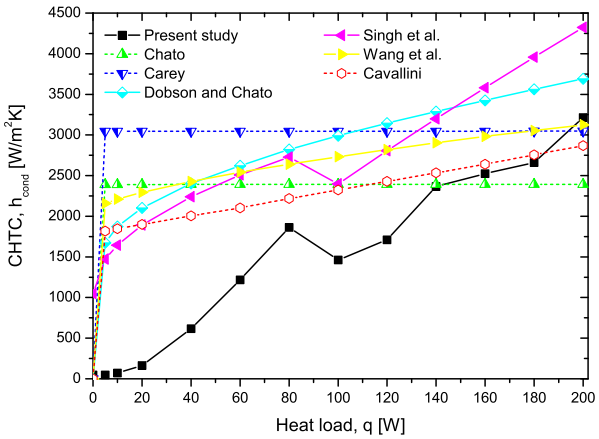

Figure 6.11: Condensation heat transfer coefficient validation.

The figure shows considerable differences between the values obtained from the experimental measurements and those predicted by different correlations. This discrepancy is expected since, as briefly detailed in tables 3.1 and 3.2, these correlations were proposed for geometries, fluids and a wide variety of other conditions, which do not exactly match those used in the present work. Moreover these correlations depend on the vapour quality x and on fluid mass velocity G along the condenser tubes that are roughly determined. The dot lines correspond to correlations devised for stratified flow while the continuous lines are related to correlations developed for wavy flow (booth in stratified regime). The heat transfer values predicted by Singh et al. [71] correlation produce a good resemblance with the experimental data set, presenting a similar trend with the increase of heat load, thus, qualitatively confirming the HTC inside the inclined flat tubes. These results suggest that the flow in the condenser studied in the present work is wavy and not stratified, as initially predicted.

Concerning specifically the effect of the tilt angle, Lips and Meyer [44–46], as detailed in 2.3, sum-

marily refer that the effect of inclination is more pronounced at low mass fluxes, low vapour qualities and high saturation temperature. Depending on these parameters, Lips and Meyer experimentally evidenced that there is an optimum inclination angle between -15° and -30° that leads to the highest heat transfer coefficient. In the present configuration the tilt angle affects many variables such as the positioning distance of the condenser relative to the evaporator (influencing the head pressure and also the pipe friction losses), liquid and vapour flow in the plenum chambers, pressure drop and liquid residence time. These parameters were never reported in the literature, as argued by Lips and Meyer [46].

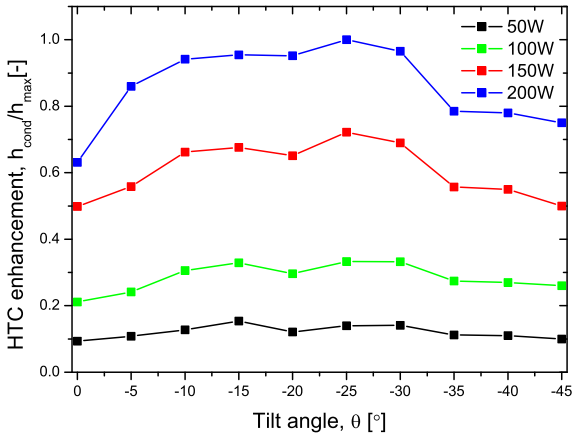

Figure 6.12: Tilt angle effect on HTC in circulation mode, for different heat loads under controlled conditions [Horizontal].

Figure 6.12 depicts the tilt angle effect in terms of HTC ratio, in the steady-state, for the the entire range of heat load tested in the present work. Despite the lower mass fluxes at low heat loads, the effect of inclination is more pronounced at higher heat loads, which would not be entirely expected. Nonetheless, it is necessary take into account that the mass fluxes in this system are very low when compared to the mentioned studies in inclination effect. Besides that, increasing the heat load, the mean vapour quality along the flat tubes of the condenser decreases due to the higher HTC and the saturation temperature in the condenser slightly increases. These factors explain the more pronounced inclination effect at higher heat loads. Therefore, these results show that the optimum tilt angle for the system studied here is around 25° (downward). This was the tilt angle value that was implemented for all the experiments with this condenser in circulation mode. These conclusions are in agreement with most of the studies reported in the literature in this topic, suggesting that the impact of the tilt angle is not much sensitive to differences in the channel geometry.

The alternative condenser tested, under reflux condensation, refers to the condensation process that occurs in a vertical or an inclined tube in which vapour is flowing upward driven by buoyancy forces,

while liquid is flowing downward due to gravity. This gravity-controlled condensation process has been increasingly applied to compact plate heat exchangers, such as the case of the one used in present work. The reviewed literature refers that this configuration has several benefits when compared with the single-pass condenser. First of all, in the context of the present case application, this configuration would result in a more compact geometry, because the liquid line could be suppressed. Also, liquid residence time is also expected to decrease, as the first droplets of condensed liquid could leave the condenser in a shorter period of time and with less sub-cooling. Although larger sub-cooling is not considered an adverse effect, it should be avoided, since the sensitive heat transfer term is much lower, when compared to the vaporization heat transfer. In this context, the system devised in the present work, accounted for the possibility of using a reflux condenser configuration. However, the operability of reflux condensers is limited by the phenomenon of flooding that appears at a critical vapour velocity at which the condensate starts to flow upward rather than downward. Flooding deteriorates the normal operation of the multiphase systems, which inevitably results in an abrupt increase of pressure drop (more information in 2.2). Among the numerous observations, the obtained data by different authors remain significantly scattered and contradictions in the data still persist due to the complicated nature of the flow subject to the effects of liquid viscosity, tube length and slug position. In the present configuration, it was concluded that the condenser inclination has low impact on the HTC enhancement. For this reason, the selected angle, 40°, was chosen taking into account the performed studies in this topic.

In summary, the condenser inclination angles used on the next experimental tests was 25° (downward) for circulation and 40° (upward) for reflux mode.

Circulation vs Reflux

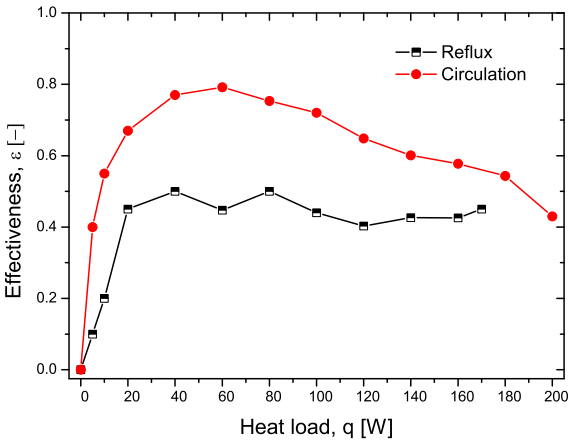

Figure 6.13: Condenser performance at steady-state [Horizontal].

The setup was not exactly arranged in the same way for the two condenser's flow, as described in the

previous chapter 5.1. Consequently the fan rotation speed imposed to control the evaporator pressure was not necessarily the same, which interferes in the heat exchanger efficiency. Therefore, in order to compare and evaluate the performance of the different condenser's flow configurations, without taking into account the air-flow speed, the effectiveness was determined and used to evaluate the condenser's performance. In this context, figure 6.13 depicts the heat exchanger performance along the applied heat load. Here, the condenser's performance is evaluated looking at its effectiveness and at its final impact on the boiling curve and thermal resistance (figure 6.14) for both reflux and single-pass flow configurations. Overall, the results support that the single-pass condenser in circulation mode has better effectiveness values and for this reason better performance results for all the applied heat load's range.

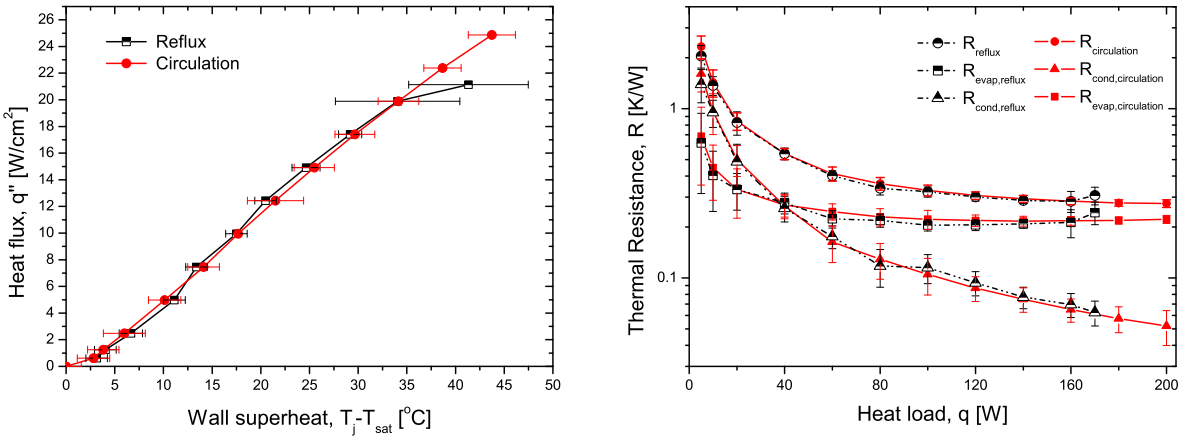

a) Pool boiling curves. **b)** Thermal resistance.

Figure 6.14: System thermal performance for different condensers (Reflux and Circulation) under steady and controlled conditions [Horizontal].

Furthermore, analyzing all the results one must conclude that despite all the potential advantages of using the reflux configuration, for the system devised here the condensation in circulation mode is preferred in steady-state working conditions as it overall shows better effectiveness for similar heat flux and thermal resistance, when compared to the reflux configuration. The overall thermal resistance for the maximum achievable dissipated power is $R_{sys} = 0.275\mathrm{K/W}$ for the circulation and $R_{sys} = 0.303\mathrm{K/W}$ with condenser in reflux mode, for $q = 200\mathrm{W}$ and $q = 170\mathrm{W}$ respectively. This means that under stationary conditions, the closed loop thermosyphon presents 7.5% lower mean absolute thermal resistance than with condensation in reflux mode, resulting in a mean junction-air temperature reduction of $4°\mathrm{C}$ for a heat load of $170\mathrm{W}$.

6.3 Experimental Facility Under Real Working Conditions - Transient-State

The current section covers the outcomes of the transient study performed, which is more representative from the conditions occurring in real CPUs. Hence, this part of the work was performed to evaluate the transient system response to a heat load input. A real scenario, named as I&M transient power load was implemented, as detailed before in 5.2.3. The experimental facility was tested in horizontal and vertical orientations, under this load at real working conditions as described in 6.1.1. In this section all the experimental data was obtained with the smooth and optimized mircro-structured surfaces ($S = 100\mu\mathrm{m}$) and the condenser was positioned in the respective optimized inclination (-25° for circulation condenser and 40° for the reflux condenser).

Validation of the Results at the Transient-State

The time-temperature and time-pressure values of the thermosyphon system were recorded. Specifically, saturation temperature T_{sat}, junction temperature T_j, external ambient air temperature T_∞ and the thermosyphon pressure in the evaporator p_{evap} were the quantities monitored. The transient response of the system, with the condenser in reflux mode is depicted in figure 6.15, which shows the thermal and pressure response to a cycle of sudden power loads, which, as explained in chapter 5, represents a benchmark of a real CPU, based on that reported by Isci and Martonosi [90]. These results are compared with those reported by [33], under similar working conditions (exception made to the setup orientation, as [33] used the setup vertically oriented). The variations detected in the ambient air

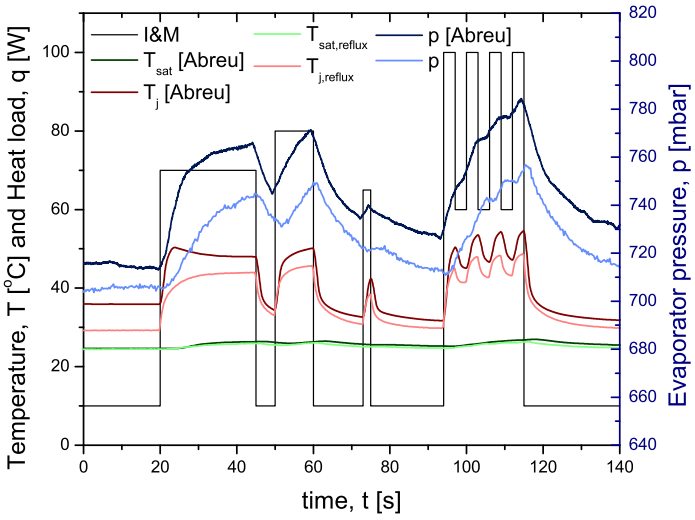

Figure 6.15: Transient experimental results validation with reflux condenser [Horizontal].

temperature are negligible ($< 0.5°\mathrm{C}$), so they are not shown here, for the sake of clarity of the plot. [33] reported that the critical design parameter could be the settled (steady-state) temperature or the onset of nucleate boiling, depending on the surface and power step input. These conclusions are corroborated in the present work, although in the present case, for the optimized surface, $S = 100\mu\mathrm{m}$, the power step of $10\mathrm{W}$ is enough to reach the nucleate boiling region, so that there is no onset of boiling, as illustrated in figure 6.15.

Figure 6.15 evidences that due to smaller saturation pressures a lower boiling temperature is reached, so for the same applied power input, the nucleate boiling onset occurs earlier in time and for lower value of imposed heat load, showing a smother progression from the natural convection regime. In fact, for the $100\mu\mathrm{m}$ surface, the nucleation sites become active right at the initial steady-state at initial $10\mathrm{W}$ imposed heat load. Thus, in the present study, junction temperature is smoothly increased and stabilized instead of sharply reducing after an instantaneous onset of boiling as observed in [33]. Furthermore, a better performance was obtained, with lower pressure values and lower temperatures, resulting in 10% junction temperature enhancement. In the present scenario the system would safely perform throughout all the cycle's time span, since the maximum temperature, achieved at around $115\mathrm{s}$, was $48.7°\mathrm{C}$.

Circulation vs Reflux

In this sub-section the condenser's impact on the transient thermosyphon system is investigated. Figure 6.16 allow taking useful conclusions to be used on the CPU cooling product development. The

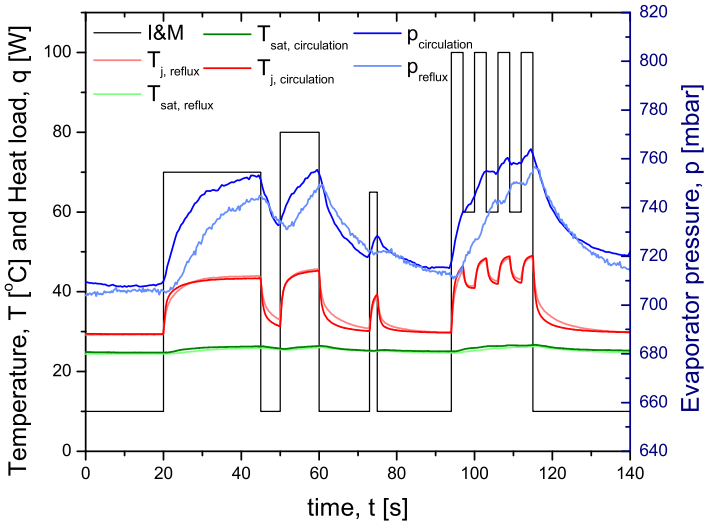

Figure 6.16: Thermal and pressure transient response for different condensers (Reflux and Circulation) [Horizontal].

results, discussed in detail in the following paragraphs allowed concluding that the setup with condenser

in circulation mode depicts quicker response time than that with reflux condensation, as shown on the plot by the steeper junction temperature response as well on pressure curves.

Despite the reflux mode's facility used 2 pipes instead of just one as in the circulation flow, an increase in the condensate mass flow was expected, which could cool down the working fluid temperature, decreasing the evaporator pressure and enhancing the overall cooler performance. However the pressure and temperature reduction are almost negligible as a minimal $10\mathrm{mbar}$ and $0.5^{\circ}\mathrm{C}$ decreasing of pressure and saturation temperature were observed, respectively. By the system response evolution previously discussed, it was possible to predict that the CLTPT system with condenser in circulation mode has better efficiency than CTPT with condenser in reflux mode. To confirm this prediction, an evaluation focused only on the condenser transient analysis was performed, where the instantaneous effectiveness values were calculated, as depicted in figure 6.17.

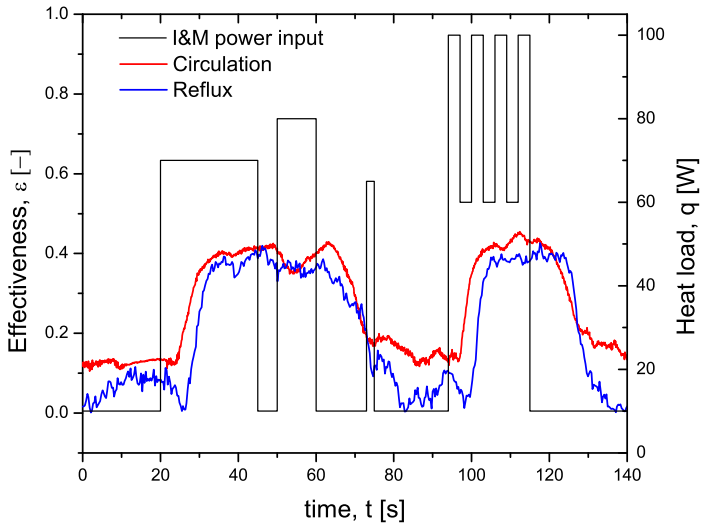

Figure 6.17: Condenser effectiveness at transient-state [Horizontal].

The condenser in reflux mode shows indeed lower effectiveness values than the circulation mode, which is in agreement with the analysis performed at steady-state. It is worth mentioning that the difference in the effectiveness in the circulation or in the reflux mode is much less prominent in the transient-state than in steady-state conditions. As also concluded in the steady-state study, it was also noticeable that in counter-current (reflux) flow condensation, the flow is much more unstable due to the vapour and liquid flow passage in the same tubes, promoting more fluctuations. This fact is well visible in figure 6.17 by the condenser's effectiveness fluctuations, being also observed on the junction temperature, when the frequency is high enough (not in the presented graphics due to representation reasons). These conclusions are in agreement with many of the studies [23, 24].

Another cyclic power input, represented by dot black line in figure 6.18, with approximately 40% higher loads, was applied to evaluate the reliability of the thermosyphon system response to more demanding loads. The condenser was placed in circulation flow mode, since it is the configuration that presents better results as explained before based on experimental results. The system evaluation performed on the maximum demanding point at 115s, resulted on an increase of 19% in junction temperatures and 5% in pressure.

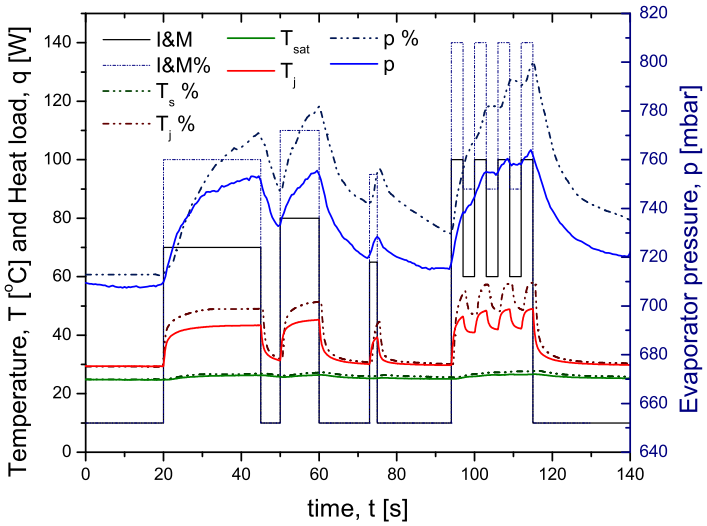

Figure 6.18: Thermal and pressure transient response for an higher cyclic heat load with circulation condenser [Horizontal].

In the present high demand heat loads scenario, the maximum temperature, achieved with the current cooling system configuration, at around 115s, was lower than 60°C as visible in figure 6.18, meaning that the system would perform safely. The design parameter that CPU manufacturers provide for cooling systems design is the Thermal Design Power, TDP, which is the maximum heat load generated by the CPU that the cooling system is designed to dissipate in typical operation conditions. Boiling onset and steady-state temperatures in a power step from 0 W to TDP should then stay below the maximum allowed temperatures.

Vertical Surface Orientation Setup

Temperature and pressure time response obtained on the vertical setup, with the microstructured surface S =100μm are presented in figure 6.19. Here, under real working conditions, as explained before (fan is rotating at constant RPM), both setup orientations are compared with the condenser working in circulation mode. Contrary to what occurred with the setup at horizontal orientation, where the pressure reached in the evaporator under RWC was lower than atmospheric, in this case the vertical setup

tends to work at higher pressure values which prejudice the system performance. This discrepancy can be due to several reasons detailed next.

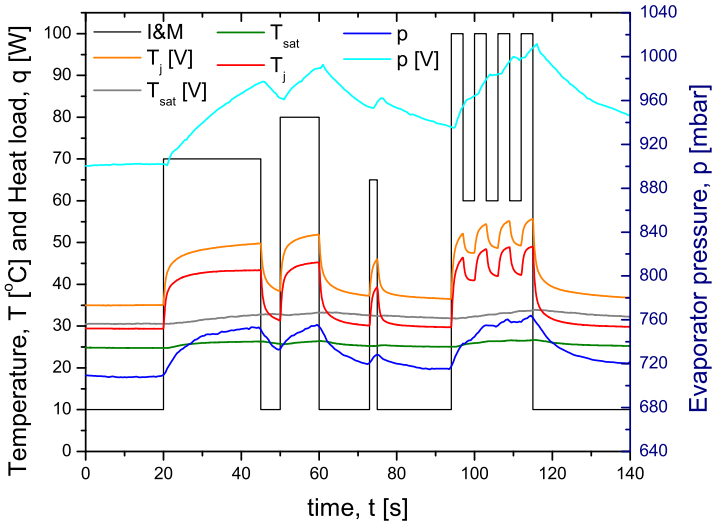

Figure 6.19: Thermal and pressure transient response for circulation condenser [Horizontal vs Vertical].

As visible in the steady-state for the vertical setup, the noticeable reduction of the liquid free height ratio affects much more the boiling heat transfer on the vertical setup. This liquid level ratio decreases with the increasing of heat load, arising to the surface dry-out that increases drastically the inner pressure. This parameter must be taken into account for an adequate design process to avoid the surface dry-out. An alternative to try to avoid this problem can be decrease the evaporator height, reducing the

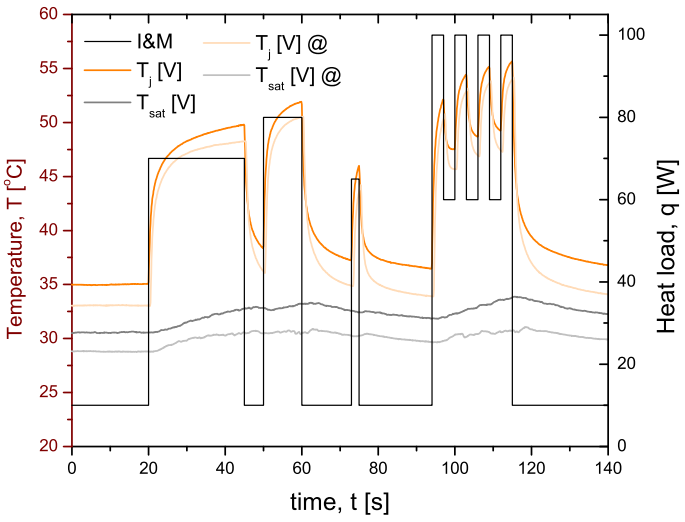

Figure 6.20: Thermal and pressure transient response with shortening evaporator volume [Vertical].

evaporator volume, so that the liquid fills the entire surface to a wider power range. In this context, the evaporator in the vertical orientation was shortened, reduced to 20mm of height, decreasing the dry-out probability and trying to reduce the governing pressure. This change was made for this vertical oriented setup, focusing on the cooler performance improvement. The obtained results are shown in figure 6.20, where the $T@$ are the temperature data obtained with the new cooler configuration. However, it is necessary take into account that for lower working fluid charge, lower is the overall cooling system performance (CHF as well as HTC could be affected).

On the other hand, the configuration differences on the vertical oriented surface setup, such as the smaller differences in heights between condenser inlet and evaporator outlet could affect the thermodynamic closed cycle. In the setup with vertical surface, it was necessary to make some changes in the configuration (detailed in 5.1), so that the steam and condensate flows naturally and fluently. All these modifications appears to affect the vertical oriented surface thermal and hydraulic performance.

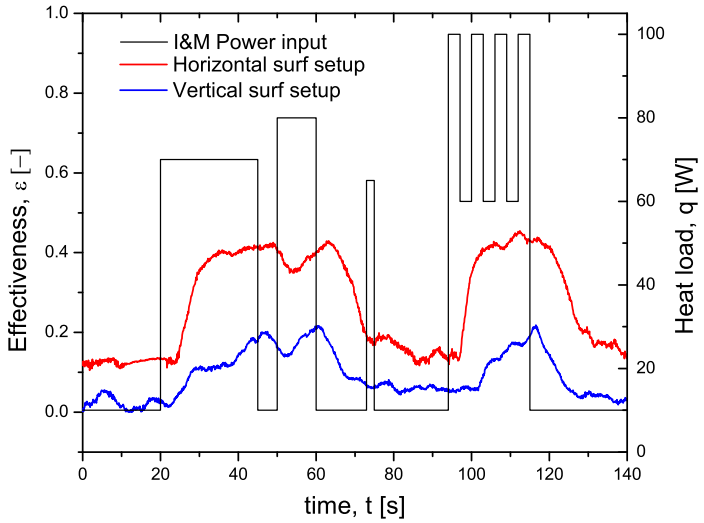

Figure 6.21: Condenser effectiveness in circulation mode at transient-state [Horizontal and Vertical].

Finally, as performed for the horizontal setup, the condenser performance was evaluated and presented in figure 6.21. The condenser effectiveness is naturally affected by the increase of the saturation temperature and consequently higher temperatures are reached at the inlet condenser plenum chamber. Beyond that, the compactness achieved with this setup also increases slightly the inlet air temperature that crosses the louvered fins of the condenser. The results show that the vertical orientation configuration system does not present good results and therefore the reflux condenser has not been tested for this orientation.

7. Conclusions and Future Work

7.1 Conclusions

The present work addresses the design and test of a custom made condenser to be implemented in a closed two-phase thermosyphon, which should be able to dissipate heat loads up to 250W. The work comprises a numerical approach to define the design of the condenser, its main characteristics, dimensions and set of the most relevant geometric and working parameters. The outcome of this approach was a louvered fins and flat tubes plate fin heat exchanger with a core's size of 110x120x22mm, which was possible to build, under the current limitations pointed by the manufacturers. However, the analysis performed on the relevant parameters affecting the heat transfer and fluid dynamic processes in the condenser suggests that the condenser's transversal area could be reduced up to 12$\%$.

An appropriate benchmark experimental facility was used to evaluate the condenser's effectiveness and its real impact on the performance of the cooling system that is being devised. The benchmark simulates the CPU thermal dissipation under steady-state and transient conditions allowing a detailed study of the condenser and of the whole cooling system. The condenser was tested in both circulation and reflux modes. The study performed here allowed setting the following main conclusions, towards the development of a final functional cooling system:

- In steady-state working conditions, the inclination angle of the condenser in circulation mode was found to affect the system performance, namely affecting the heat flux and the heat transfer coefficient. An optimum value of 25° downward was obtained for the inclination angle when the condenser was working in the circulation mode. The effect of the inclination angle was found negligible for the condenser working in the reflux mode.
- In steady-state regime the condenser in circulation mode depicts better effectiveness than in the reflux mode. In steady-state (under controlled pressure conditions), the circulation mode leads to a maximum effectiveness which is 60$\%$ higher than that of the condenser in the reflux mode. In the transient regime, the working mode of the condenser (circulation or reflux) has no impact on the working performance of the cooling system.
- Under controlled pressure conditions (steady-state), the closed loop thermosyphon (circulation mode) achieves a maximum power dissipation of 200W, while the closed reflux two-phase termosyphon reaches 170W maximum power dissipation. The mean absolute thermal resistance with condenser in circulation mode is lower 7.5$\%$ than with condenser in reflux mode, resulting in mean junction-air temperature reduction of 4$^\circ C$ for 170W.

- Overall, the work performs here shows that a closed loop two-phase termosyphon with the condenser in circulation mode is more stable (i.e. the governing pressure and the junction temperature, which represents the temperature of the processor, suffer less fluctuations, which is advantageous in view of the future implementation in a commercial CPU) and leads to a better cooling performance of the entire cooling system.

Based on this analysis, the final closed loop thermosyphon system devised here achieved a $R = 0.275\mathrm{K/W}$ with $q = 200\mathrm{W}$ for horizontal orientation. These values were obtained using a microstructured surface with cavity distance of $100\mu\mathrm{m}$ in the evaporator, following the obtained in previous stages of development of the current system, which were confirmed in the present work.

7.2 Future Work

A few upgrades are recommended to the experimental facility, which will allow a more detailed and precise characterization of the cooling system under relevant working conditions. For instance, it would be advantageous to add more temperature and pressure sensors, together with mass flow meters, to have a more detailed description of the temperature and pressure variations, as well as to have a well defined quantification of the mass flow rates through the system. In addition, heat transfer and pressure drop characteristics along the air-side of the heat exchanger should be studied in a wind tunnel in order to provide measurement of the air mass flow rate through the condenser.

The final results have shown that the condenser has to be further improved. On the air-side of the extended surfaces it is promising to explore the potential use of delta-winglets vortex generators. The use of louvers is a passive technique that causes high heat transfer enhancement with some drop pressure penalty but vortex generators are recognized to provide heat transfer enhancement with relatively small pressure drop penalty, even for high inlet velocities.

On the condensation-side, micro-fins tubes could be applied in the condenser in order to enhance the condensation heat transfer coefficient. This requires a detailed study of the use of micro and nanostructured surfaces in the condensation process, which is an interesting and relevant research topic, with relevant outcomes for the specific application that is being studied here.

Regarding the overall cooler system, the fill ratio should be a parameter to be more closely studied in both loop and single pipe two-phase systems. Furthermore, the next incoming step to be followed comprises the assembly and long test running tests of the dimensioned two-phase loop thermosyphon (including the improved custom made condenser) in a real desktop PC.

Bibliography

[1] G. E. Moore, “Cramming more components onto integrated circuits, reprinted from electronics, volume 38, number 8, april 19, 1965, pp.114 ff.” IEEE Solid-State Circuits Society Newsletter, vol. 11, no. 3, pp. 33–35, 2006.

[2] R. Dennard, F. Gaensslen, W.-N. Yu, L. Rideout, E. Bassous, and A. Le Blanc, “Design of Ion-Implanted Small MOSFET ’ S Dimensions with Very,” IEEE Journal of Solid State Circuits, vol. 9, no. 5, pp. 257–268, 1974.

[3] K. Roy, S. Mukhopadhyay, and H. Mahmoodi-Meimand, “Leakage current mechanisms and leakage reduction techniques in deep-submicrometer CMOS circuits,” Proceedings of the IEEE, vol. 91, no. 2, pp. 305–327, 2003.

[4] B. Sun and H. Liu, “Flow and heat transfer characteristics of nanofluids in a liquid-cooled CPU heat radiator,” Applied Thermal Engineering, vol. 115, pp. 435–443, 2017.

[5] F. Cataldo and J. R. Thome, “Experimental evaluation of the thermal performances of a thermosyphon cooling system rejecting heat by natural and forced convection,” Applied Thermal Engineering, vol. 127, pp. 1404–1415, 2017.

[6] H. Y. Li and S. M. Chao, “Measurement of performance of plate-fin heat sinks with cross flow cooling,” International Journal of Heat and Mass Transfer, vol. 52, no. 13-14, pp. 2949–2955, 2009.

[7] B. Agostini, M. Fabbri, J. E. Park, L. Wojtan, J. R. Thome, and B. Michel, “State of the art of high heat flux cooling technologies,” Heat Transfer Engineering, vol. 28, no. 4, pp. 258–281, 2007.

[8] V. Silvério, S. Cardoso, J. Gaspar, P. P. Freitas, and A. L. Moreira, “Design, fabrication and test of an integrated multi-microchannel heat sink for electronics cooling,” Sensors and Actuators, A: Physical, vol. 235, pp. 14–27, 2015.

[9] M. K. Sung and I. Mudawar, “Effects of jet pattern on two-phase performance of hybrid micro-channel/micro-circular-jet-impingement thermal management scheme,” International Journal of Heat and Mass Transfer, vol. 52, no. 13-14, pp. 3364–3372, 2009.

[10] M. R. Panão, J. P. Guerreiro, and A. L. Moreira, “Microprocessor cooling based on an intermittent multijet spray system,” International Journal of Heat and Mass Transfer, vol. 55, no. 11-12, pp. 2854–2863, 2012.

[11] I. Mudawar, “Assessment of high-heat-flux thermal management schemes,” IEEE Transactions on Components and Packaging Technologies, vol. 24, no. 2, pp. 122–141, 2001.

[12] S. Malla, M. Amaya, H. Moon, and S. M. You, “Liquid cooling of a hot spot using a superhydrophilic nanoporous surface,” Thermomechanical Phenomena in Electronic Systems -Proceedings of the Intersociety Conference, pp. 317–325, 2014.

[13] A. Samba, H. Louahlia-Gualous, S. Le Masson, and D. Nörterhäuser, “Two-phase thermosyphon loop for cooling outdoor telecommunication equipments,” Applied Thermal Engineering, vol. 50, no. 1, pp. 1351–1360, 2013.

[14] X. Chen, H. Ye, X. Fan, T. Ren, and G. Zhang, “A review of small heat pipes for electronics,” Applied Thermal Engineering, vol. 96, pp. 1–17, 2016.

[15] T. E. Tsai, H. H. Wu, C. C. Chang, and S. L. Chen, “Two-phase closed thermosyphon vapor-chamber system for electronic cooling,” International Communications in Heat and Mass Transfer, vol. 37, no. 5, pp. 484–489, 2010.

[16] C. C. Chang, S. C. Kuo, M. T. Ke, and S. L. Chen, “Two-phase closed-loop thermosyphon for electronic cooling,” Experimental Heat Transfer, vol. 23, no. 2, pp. 144–156, 2010.

[17] Y. Kim, D. Hwan Shin, J. Sub Kim, S. M. You, and J. Lee, “Boiling and condensation heat transfer of inclined two-phase closed thermosyphon with various filling ratios,” Applied Thermal Engineering, vol. 145, no. September, pp. 328–342, 2018.

[18] H. Shabgard, B. Xiao, A. Faghri, R. Gupta, and W. Weissman, “Thermal characteristics of a closed thermosyphon under various filling conditions,” International Journal of Heat and Mass Transfer, vol. 70, pp. 91–102, 2014.

[19] R. Khodabandeh and B. Palm, “Influence of system pressure on the boiling heat transfer coefficient in a closed two-phase thermosyphon loop,” International Journal of Thermal Sciences, vol. 41, no. 7, pp. 619–624, 2002.

[20] J. Seo and J. Y. Lee, “Length effect on entrainment limitation of vertical wickless heat pipe,” International Journal of Heat and Mass Transfer, vol. 101, pp. 373–378, 2016.

[21] E. I. Drosos, S. V. Paras, and A. J. Karabelas, “Counter-current gas-liquid flow in a vertical narrow channel-Liquid film characteristics and flooding phenomena,” International Journal of Multiphase Flow, vol. 32, no. 1, pp. 51–81, 2006.

[22] A. A. Mouza, S. V. Paras, and A. J. Karabelas, “the Influence of Small Tube Diameter and Inclination Angle on Flooding Phenomena,” International Journal of Multiphase Flow, vol. 28, pp. 1311–1331, 2002.

[23] M. Zhang, Z. Liu, and G. Ma, “The experimental investigation on thermal performance of a flat two-phase thermosyphon,” International Journal of Thermal Sciences, vol. 47, no. 9, pp. 1195–1203, 2008.

[24] G. Xia, W. Wang, L. Cheng, and D. Ma, “Visualization study on the instabilities of phase-change heat transfer in a flat two-phase closed thermosyphon,” Applied Thermal Engineering, vol. 116, pp. 392–405, 2017.

[25] S. J. D. van Stralen, R. Cole, W. M. Sluyter, and M. S. Sohalt, “Bubble growth rates in nucleate boiling of water at subatmospheric pressures,” International Journal of Heat and Mass Transfer, vol. 18, pp. 655–669, 1975.

[26] D. E. Kim, D. I. Yu, D. W. Jerng, M. H. Kim, and H. S. Ahn, “Review of boiling heat transfer enhancement on micro/nanostructured surfaces,” Experimental Thermal and Fluid Science, vol. 66, pp. 173–196, 2015.

[27] M. I., E. Teodori, A. Moita, A. Moreira, and M. Marengo, “Wettability effect on pool boiling: a review.” Encyclopaedia of Two-Phase Heat Transfer and Flow III: Macro And Micro Flow Boiling And Numerical Modeling Fundamentals, vol. 4, pp. 437–448, 2018.

[28] M. Moura, “Design and development of a two-phase closed loop thermosyphon for CPU cooling,” Master’s thesis, IST, Lisboa, Portugal, 2015.

[29] A. Moita, E. Teodori, and A. Moreira, “Influence of surface topography in the boiling mechanisms,” International Journal of Heat and Fluid Flow, vol. 52, pp. 50 – 63, 2015.

[30] M. Moura, E. Teodori, A. S. Moita, and A. L. Moreira, “2 phase microprocessor cooling system with controlled pool boiling of dielectrics over micro-and-nano structured Integrated Heat Spreaders,” Proceedings of the 15th InterSociety Conference on Thermal and Thermomechanical Phenomena in Electronic Systems, ITherm 2016, pp. 378–387, 2016.

[31] A. S. Moita, E. Teodori, and A. L. N. Moreira, “Enhancement of pool boiling heat transfer by surface micro-structuring,” Journal of Physics: Conference Series, vol. 395, p. 012175, 2012.

[32] E. Teodori, A. S. Moita, and A. L. Moreira, “Characterization of pool boiling mechanisms over micro-patterned surfaces using PIV,” International Journal of Heat and Mass Transfer, vol. 66, pp. 261–270, 2013.

[33] V. Abreu, “Test and optimization of a two-phase thermosyphon cooling system for microprocessors under real working conditions,” Master’s thesis, IST, Lisboa, Portugal, 2017.

[34] K. Nishikawa, Y. Fujita, S. Uchida, and H. Ohta, “Effect of surface configuration on nucleate boiling heat transfer,” International Journal of Heat and Mass Transfer, vol. 27, no. 9, pp. 1559–1571, 1984.

[35] M. S. El-Genk and H. Bostanci, “Saturation boiling of HFE-7100 from a copper surface, simulating a microelectronic chip,” International Journal of Heat and Mass Transfer, vol. 46, no. 10, pp. 1841–1854, 2003.

[36] A. Priarone, “Effect of surface orientation on nucleate boiling and critical heat flux of dielectric fluids,” International Journal of Thermal Sciences, vol. 44, no. 9, pp. 822–831, 2005.

[37] M. S. El-Genk and J. L. Parker, “Nucleate boiling of FC-72 and HFE-7100 on porous graphite at different orientations and liquid subcooling,” Energy Conversion and Management, vol. 49, no. 4, pp. 733–750, 2008.

[38] D. P. Rini, R. H. Chen, and L. C. Chow, “Bubble behavior and heat transfer mechanism in FC-72 pool boiling,” Experimental Heat Transfer, vol. 14, no. 1, pp. 27–44, 2001.

[39] W. Kays and A. London, Compact heat exchangers. Krieger Pub. Co., 1984.

[40] K. Aroonrat and S. Wongwises, “Experimental study on two-phase condensation heat transfer and pressure drop of R-134a flowing in a dimpled tube,” International Journal of Heat and Mass Transfer, vol. 106, pp. 437–448, 2017.

[41] D. Jung, Y. Cho, and K. Park, “Flow condensation heat transfer coefficients of R22, R134a, R407C, and R410A inside plain and microfin tubes,” International Journal of Refrigeration, vol. 27, no. 1, pp. 25–32, 2004.

[42] G. Li, L. Huang, and L. Tao, “Experimental investigation of refrigerant condensation heat transfer characteristics in the horizontal microfin tubes,” Applied Thermal Engineering, vol. 123, pp. 1484–1493, 2017.

[43] S. P. Guo, Z. Wu, W. Li, D. Kukulka, B. Sundén, X. P. Zhou, J. J. Wei, and T. Simon, “Condensation and evaporation heat transfer characteristics in horizontal smooth, herringbone and enhanced surface EHT tubes,” International Journal of Heat and Mass Transfer, vol. 85, pp. 281–291, 2015.

[44] S. Lips and J. P. Meyer, “Two-phase flow in inclined tubes with specific reference to condensation: A review,” International Journal of Multiphase Flow, vol. 37, no. 8, pp. 845 – 859, 2011.

[45] S. Lips and J. P. Meyer, “Stratified flow model for convective condensation in an inclined tube,” International Journal of Heat and Fluid Flow, vol. 36, pp. 83–91, 2012.

[46] S. Lips and J. P. Meyer, “Experimental study of convective condensation in an inclined smooth tube. Part I: Inclination effect on flow pattern and heat transfer coefficient,” International Journal of Heat and Mass Transfer, vol. 55, no. 1-3, pp. 395–404, 2012.

[47] J. Meyer and D. Ewim, “Heat transfer coefficients during the condensation of low mass fluxes in smooth horizontal tubes,” International Journal of Multiphase Flow, vol. 99, pp. 485 – 499, 2018.

[48] S. N. R. Abadi, J. Meyer, and J. Dirker, “Numerical simulation of condensation inside an inclined smooth tube,” Chemical Engineering Science, vol. 182, pp. 132–145, 2018.

[49] D. Del Col, M. Bortolato, M. Azzolin, and S. Bortolin, “Effect of inclination during condensation inside a square cross section minichannel,” International Journal of Heat and Mass Transfer, vol. 78, pp. 760–777, 2014.

[50] S. Fiedler and H. Auracher, “Experimental and theoretical investigation of reflux condensation in an inclined small diameter tube,” International Journal of Heat and Mass Transfer, vol. 47, no. 19-20, pp. 4031–4043, 2004.

[51] T. Klahm, H. Auracher, and F. Ziegler, “Heat transfer during reflux condensation of an R134a/R123 mixture in vertical and inclined narrow tubular and rectangular channels,” International Journal of Refrigeration, vol. 33, no. 7, pp. 1319–1326, 2010.

[52] S. Nukiyama, “The maximum and minimum values of the heat q transmitted from metal to boiling water under atmospheric pressure,” International Journal of Heat and Mass Transfer, vol. 9, no. 12, pp. 1419 – 1433, 1966 (originally Journal of the Japan Society of Mechanical Engineers, Vol. 37, 1934, pp. 367-374).

[53] V. Carey, Liquid–Vapor Phase-change Phenomena. New York: Hemisphere, 1992.

[54] S. Kandlikar and W.J.Grande, “Evolution of microchannel flow passages–thermohydraulic performance and fabrication technology,” Heat Transfer Engineering, vol. 24, no. 1, pp. 3–17, 2003.

[55] S. Mehendail, A. Jacobi, and R. Shah, “Fluid flow and heat transfer at micro- and meso-scales with application in heat exchanger design,” Appl. Mech. Rev, vol. 53, no. 7, p. 105–116, 2000.

[56] S. M. Kim and I. Mudawar, “Universal approach to predicting heat transfer coefficient for condensing mini/micro-channel flow,” International Journal of Heat and Mass Transfer, vol. 56, no. 1-2, pp. 238–250, 2013.

[57] P. Cheng and H. Wu, “Mesoscale and microscale phase-change heat transfer,” Advances in Heat Transfer, vol. 39, pp. 461 – 563, 2006.

[58] J. Chato, “Laminar condensation inside horizontal and inclined tubes,” ASHRAEL J., vol. 4, no. 2, pp. 52–60, 1962.

[59] J. R. Thome and J. E. Hajal, “Two-Phase Flow Pattern Map for Evaporation in Horizontal Tubes: Latest Version,” Heat Transfer Engineering, vol. 24, no. 6, pp. 1–2, 2003.

[60] J. El Hajal, J. R. Thome, and A. Cavallini, “Condensation in horizontal tubes, part 1: Two-phase flow pattern map,” International Journal of Heat and Mass Transfer, vol. 46, no. 18, pp. 3349–3363, 2003.

[61] R. Suliman, L. Liebenberg, and J. P. Meyer, “Improved flow pattern map for accurate prediction of the heat transfer coefficients during condensation of R-134a in smooth horizontal tubes and within the low-mass flux range,” International Journal of Heat and Mass Transfer, vol. 52, no. 25-26, pp. 5701–5711, 2009.

[62] N. Kattan, J. R. Thome, and D. Favrat, “Flow Boiling in Horizontal Tubes: Part 1—Development of a Diabatic Two-Phase Flow Pattern Map,” Journal of Heat Transfer, vol. 120, no. 1, p. 140, 1998.

[63] A. Cavallini, G. Censi, D. Del Col, L. Doretti, G. A. Longo, and L. Rossetto, “Condensation of halogenated refrigerants inside smooth tubes,” HVAC and R Research, vol. 8, no. 4, pp. 429–451, 2002.

[64] J. W. Coleman and S. Garimella, “Characterization of two-phase flow patterns in small diameter round and rectangular tubes,” International Journal of Heat and Mass Transfer, vol. 42, no. 15, pp. 2869–2881, 1999.

[65] S. Bortolin, E. Da Riva, and D. Del Col, “Condensation in a square minichannel: Application of the VOF method,” Heat Transfer Engineering, vol. 35, no. 2, pp. 193–203, 2014.

[66] P. Toninelli, S. Bortolin, M. Azzolin, and D. Del Col, “Effects of geometry and fluid properties during condensation in minichannels: experiments and simulations,” Heat and Mass Transfer, pp. 1–17, 2017.

[67] D. Del Col, S. Bortolin, A. Cavallini, and M. Matkovic, “Effect of cross sectional shape during condensation in a single square minichannel,” International Journal of Heat and Mass Transfer, vol. 54, no. 17-18, pp. 3909–3920, 2011.

[68] J. Chato, “Laminar condensation inside horizontal tubes,” Ph.D. dissertation, Massachusetts Institute of Technology, 1960.

[69] S. Dalkilic, A.S., Yildiz, S., Wongwises, “Experimental investigation of convective heat transfer coefficient during downward laminar flow condensation of R134a in a vertical smooth tube.” Int. J. Heat Mass Transfer, vol. 52, pp. 142–150, 2009.

[70] S. M. Zivi, “Estimation of steady-state steam void-fraction by means of the principle of minimum entropy production.” Journal of Heat Transfer, vol. 86, 1964.

[71] A. Singh, M. Ohadi, and S. Dessiatoun, “Empirical modeling of stratified-wavy flow condensation heat transfer in smooth horizontal tubes,” in annual meeting of the American Society of Heating. San Antonio, TX (United States): Refrigerating and Air-Conditioning Engineers (ASHRAE), 1996.

[72] M. K. Dobson and J. C. Chato, “Condensation in Smooth Horizontal Tubes,” Journal of Heat Transfer, vol. 120, no. 1, pp. 193–213, 1998.

[73] V. Gnielinski, “New equations for heat and mass transfer in the turbulent flow in pipes and channels,” Int Chem Eng, vol. 16, pp. 359–368, 1976.

[74] W. W. William Wang, T. D. Radcliff, and R. N. Christensen, “A condensation heat transfer correlation for millimeter-scale tubing with flow regime transition,” Experimental Thermal and Fluid Science, vol. 26, no. 5, pp. 473–485, 2002.

[75] J. R. Thome, J. El Hajal, and A. Cavallini, “Condensation in horizontal tubes, part 2: New heat transfer model based on flow regimes,” International Journal of Heat and Mass Transfer, vol. 46, no. 18, pp. 3365–3387, 2003.

[76] A. Cavallini, D. Del Col, L. Doretti, M. Matkovic, L. Rossetto, C. Zilio, and G. Censi, “Condensation in horizontal smooth tubes: A new heat transfer model for heat exchanger design,” Heat Transfer Engineering, vol. 27, no. 8, pp. 31–38, 2006.

[77] J. H. Kim, J. H. Yun, and C. S. Lee, “Heat-Transfer and Friction Characteristics for the Louver-Fin Heat Exchanger,” Journal of Thermophysics and Heat Transfer, vol. 18, no. 1, pp. 58–64, 2004.

[78] F. White, Fluid Mechanics, ser. McGraw-Hill series in mechanical engineering. McGraw Hill, 2011.

[79] H. Aoki, T. Shinagawa, and K. Suga, “An Experimental Study of the Local Heat Transfer Characteristics in Automotive Louvered Fins,” Experimental Thermal and Fluid Science, vol. 2, pp. 293–300, 1989.

[80] Y. J. Chang and C. C. Wang, “A generalized heat transfer correlation for louver fin geometry,” Int J Heat Mass Transfer, vol. 40, no. 3, p. 533–544, 1997.

[81] M. H. Kim and C. W. Bullard, “Air-side thermal hydraulic performance of multi-louvered fin aluminum heat exchangers,” Int J Refrigeration, vol. 25, no. 3, p. 390–400, 2002.

[82] Y. J., K. C. Hsu, Y. T. Lin, and C. C. Wanga, “Generalized friction correlation for louver fin geometry,” Int J Heat Mass Transfer, vol. 43, no. 12, p. 2237–2243, 2000.

[83] T. A. Cowell, M. R. Heikal, and A. Achaichia, “Fluid flow and heat transfer in compact louvered fin surfaces,” Exp Thermal Fluid Sci, vol. 10, no. 2, p. 192–199, 1995.

[84] A. A. Antoniou and T. A. C. M. R. Heikal, “Measurements of local velocity and turbulence levels in array of louvered plate fins,” Proceedings of the 9th International Heat Transfer Conference on Numerical Methods in Laminar and Turbulent Flow, p. 482–495, 1987.

[85] D. Tafti, G. Wang, and W. Lin, “Flow transition in a multilouvered fin array,” Int J Heat Mass Transfer, vol. 43, no. 6, p. 901–919, 2000.

[86] D. Tafti and X. Zhang, “Geometry effects on flow transition in multilouvered fins - onset, propagation, and characteristic frequencies,” Int J Heat Mass Transfer, vol. 44, no. 22, p. 4195–4210, 2001.

[87] P. Shinde and C. Lin, “A heat transfer and friction factor correlation for low air-side Reynolds number applications of compact heat exchangers,” Science and Technology for the Built Environment, vol. 23, no. 1, pp. 192–210, 2016.

[88] R. K. Shah and D. P. Sekulic, Fundamentals of Heat Exchanger Design. New Jersey: John Wiley Sons, 2003.

[89] N. H. Kim and J. P. Cho, “Air-side performance of louver-finned flat aluminum heat exchangers at a low velocity region,” Heat Mass Transfer, vol. 44, no. 9, p. 1127–1139, 2008.

[90] C. Isci and M. Martonosi, “Runtime power monitoring in high-end processors: Methodology and empirical data,” in Proceedings of the 36th Annual IEEE/ACM International Symposium on Microarchitecture, ser. MICRO 36. Washington, DC, USA: IEEE Computer Society, 2003, pp. 93–.

[91] R. B. Abernethy, R. P. Benedict, and R. B. Dowdell, “ASME Measurement Uncertainty,” Journal of Fluids Engineering, vol. 107, no. 2, p. 161, 1985.

[92] S. Chang, D. Lo, K. Chiang, and C. Lin, “Sub-atmospheric boiling heat transfer and thermal performance of two-phase loop thermosyphon,” Experimental Thermal and Fluid Science, vol. 39, pp. 134 – 147, 2012.

[93] P. Zhang, B. Wang, W. Shi, L. Han, and X. Li, “Simulation on energy performance of air-conditioning system assisted with thermosyphon used in telecommunication base station,” Proceedings of BS 2013: 13th Conference of the International Building Performance Simulation Association, pp. 1548–1553, 2013.

[94] T. Valente, E. Teodori, A. Moita, and A. Moreira, “Effect of Wettability on Nucleate Boiling,” in Procedings of 11th International Conference on Heat Transfer, Fluid Mechanics and Thermodynamics EFFECT, 2015, pp. 168–177.

Annexes

A.1. Transistor power control unit

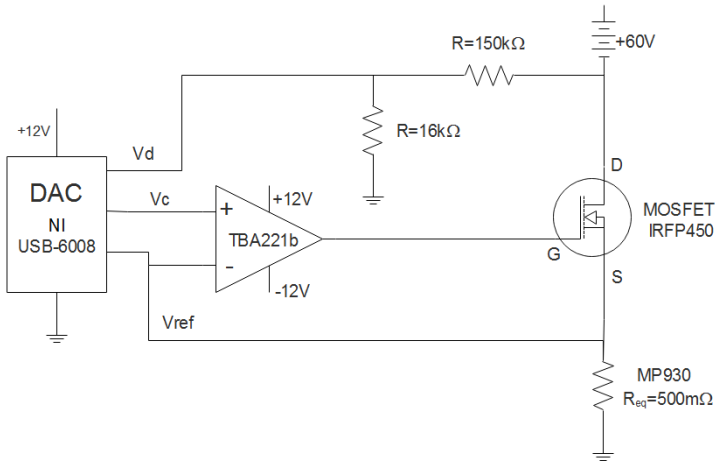

Figure 7.1: Heat load control circuit scheme.

A.2. Fan control unit

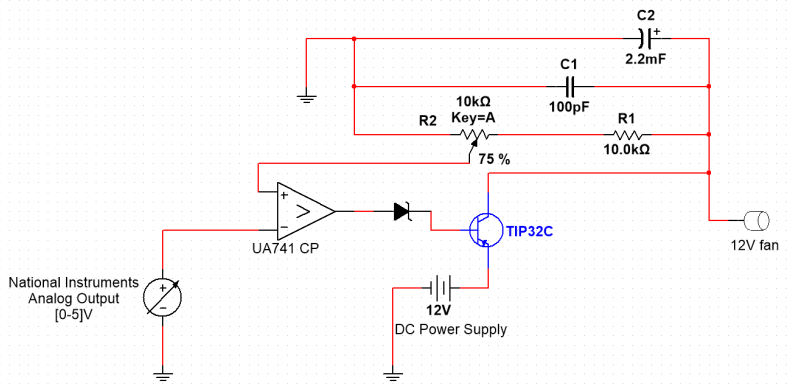

Figure 7.2: RPM's fan linear controller.

A.3. Infrared Thermography

A non-intrusive method to directly measure the two-phase temperature on the different condensers was performed, under the transient and steady-state regimes, with spatial and temporal resolved infrared thermography. Although the analysis performed at this stage is mainly qualitative, an adequate calibration process was considered.

Heres, in figure 7.3, is shown the Infrared (IR) camera recording images of the temperature gradients across the condenser for the transient-state. It is shown the condenser's temperature for different flow modes (circulation and reflux) at the same instant, when the thermal dissipation is maximum, corresponding to 115th second of the cyclic I&M load heat load input. This gives a quick snap shot of the temperature range over the entire surface area for the two studied condensers.

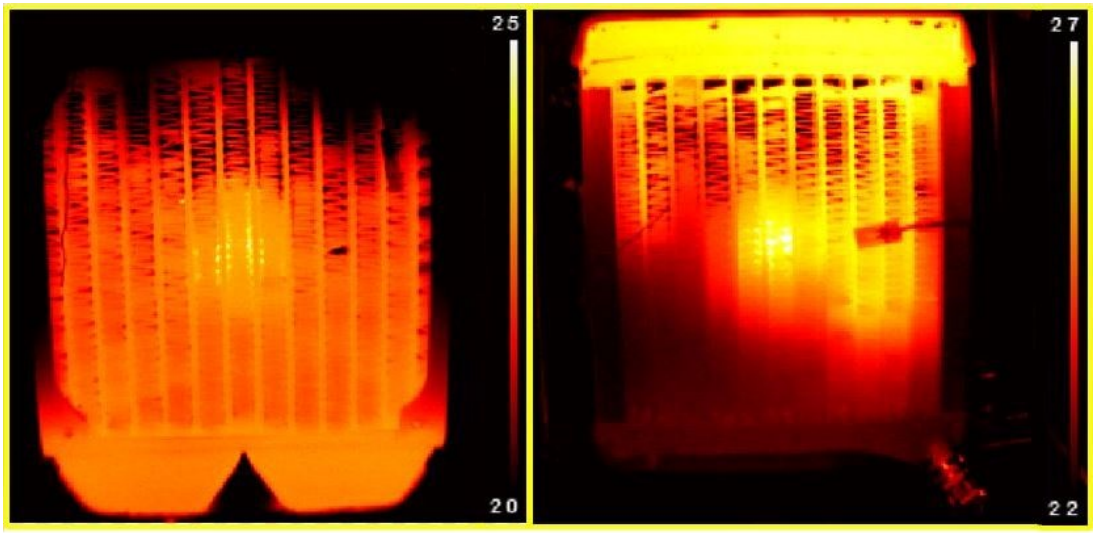

Figure 7.3: Condenser IR thermography results under transient heat load at the same instant - 115s [Horizontal oriented surface]. Reflux - left; Circulation - right.

With the IR analysis it was possible to check that the reflux condenser works under lower saturation temperatures in the condenser. This is not necessarily an advantage from the heat transfer point of view since, as aforementioned, lower working pressure results in lower boiling and condensation HTC values.